

A STUDY OF SOLAR MAGNETIC AND VELOCITY FIELDS

Shibu K. Mathew

Ph.D. Thesis
September 1998

Physical Research Laboratory
Ahmedabad 380 009, India

**A STUDY OF SOLAR MAGNETIC AND
VELOCITY FIELDS**

Shibu K. Mathew

**Physical Research Laboratory
Ahmedabad 380 009, India**

**A thesis submitted to the Gujarat University for the
Degree of Doctor of Philosophy**

September 1998

In memory of my dear mother

Smt. Thankamma Kunchandy

CERTIFICATE

I hereby declare that the work presented in this thesis is original and has not formed the basis for the award of any degree or diploma by any University or Institution.

Shibu K. Mathew

(Author)

Physical Research Laboratory
Ahmedabad - 380 009 (India)

CERTIFIED BY

Dr. Ashok N. M.

(Thesis Supervisor)

Reader

Astronomy and Astrophysics Division

Physical Research Laboratory

Ahmedabad - 380 009 (India)

Acknowledgments

I want to express my heartfelt gratitude to Prof. A. Bhatnagar, my guide, who posed the thesis subject and guided me all along the way in my research with his long experience in solar physics and especially in the field of instrumentation.

Dr. Ambastha helped me through out my research and specially during the later stages with his acumen in the field and it would be no hyperbole to say that he brought the thesis in final shape. No words can express my gratitude to him.

I want to express my gratitude to Dr. N. M. Ashok for helping me in fulfilling the statutory requirements and his moral, academic and guidance in my research.

Thanks are also due to Dr. Debi Prasad who was always available in the time of difficulty with his practical suggestions. Nandita's help, both in the hostel and the observatory require special mention. I want to express my deep gratitude to her.

I am thankful to Dr. R. M. Jain and Dr. S. C. Tripathy for their help in my research in various ways.

Neerav, Brajesh and Lokesh provided me nice company in hostel and in the observatory.

I want to express my thanks to Prof. Jack Harvey and Prof. Bill Livingston for their useful suggestions and comments on my research. Thanks are also due to Dr. Venkatakrishnan for his valuable help. Also, I want to express my thanks to Prof. Peter Foukal for his kind words and encouragement.

Thanks are due to the Director, PRL and all the Academic committee members for their frequent assessment of my work. Especially I am thankful to Prof. M. R. Deshpande, Prof. J. N. Goswami, Prof. V. B. Sheory, Dr. T. Chandrashekar and Prof. B. G. Anandarao for their continued interest in my work.

Sh. B. L. Paneri with his precision in fabrication of mechanical instrument was of immense help in building the magnetograph. All the mechanical components required for the magnetograph were designed and fabricated by him. I want to express my special thanks to him.

SOHO/MDI magnetogram used for the comparison is kindly provided by SOI-MDI group.

*Especially, I am thankful to Prof. Philip Scherrer for the SOHO magnetograms. Calibrated GONG magnetograms were kindly provided by Dr. Frank Hill, I express my thanks to him. The help of Dr. Mitzi L. Adams, for obtaining the MSFC magnetogram is acknowledged. The high voltage power supply for KD*P modulator was designed and fabricated at Space Application Center (SAC), for which I acknowledge the contributions of Dr. S. S. Rana, Sh. Arora and his group members. Dr. Balasubramaniam and Dr. Vyas from SAC are acknowledged for their help in optical coating.*

Mr. Raju Koshy and his family provided me moral help and a home away home, and also a touch of my native land Kerala with his frequent invitations for lunch and dinners. I express my heart felt gratitude to Sh. Porwal and family for their love, homely affection, help and support extended to me. I also remember Late Smt. Sardalia for her moral support.

Thanks are also due to Sh. Gupta and Sh. Naresh for their technical help.

I express my gratitude to Sh. Sanjay Bhatnagar for helping me in administrative matters. Sh. Rakesh Jaroli, Sh. Ram Chandra Carpenter and Sh. Laxmilal Suthar provided me all possible assistance.

I want to record my thanks to Sh. Shankar Lal Paliwal, Sh. Jagdish and Sh. Dal Chand for their support.

Thanks to you, Poulouse, Watson, Biju, Clement and Shibu for all your love, advises, help and support and also for your frequent moral boosting visits.

I remember with gratitude my batch mates Sandeep, Debabrat, Anshu, Prashant, Chakraborty and friends Lucky and Azim. I remember with pleasure the company of Ranjana, Bala and Prathista during their short stay in the observatory.

I am thankful to all the PRL library and computer center staffs, especially Mrs. Barucha, Mrs. Giya and Mrs. Rohini for their support and help.

I remember with gratitude the support extended by Mrs. Bhatnagar, Mrs. Ambastha and Mrs. Debi Prasad.

Thanks to Sh. Pandey, Sh. Duve, Sh. George and their families for their advice, affection

and help.

Thanks are also due to Sh. Pukhraj Joshi for providing ration. Rukmeni Ben cooked patiently for all through these years.

I would especially like to mention Sh. Heera Lalji, ex-gardner, for his help during observations. I learnt a lot of values from his unassuming character.

Thanks are also due to all the security guards, especially Dinesh, Daval, Ramchandr and Barot for their timely cup of tea while working in the night.

None of it would have been possible with out the patient support and quite inspiration of my father. I do not think it is possible to express my feelings for them in words and I will not even try. My brothers John Mathew, K. Raju and sister-in-laws Ponnamma and Leelamma supported me with love, patience and affection especially during my hard time. I also want to express my thanks to my sisters, Leelamma, Kunjumole and Kunjukunjamma and my brother-in-laws Philip, Joykutty and David for their love, affection and support. I also remember with pleasure the real love and affection of my nephews and nieces Binu, Teena, Beena, Darshan, Jinu, Jeena, Jestine, Jinson and Jessy.

At last, thanks to “Chogum” for her patience to stay with me through out the thesis period, she is my cute cat.

Research Publications

1. Solar photospheric and chromospheric observations using a Lithium Niobate Fabry-Perot etalon, 1997, Debi Prasad C., **Shibu K. Mathew**, Arvind Bhatnagar and Ashok Ambastha, *Exp. Astronomy*, **8**, 125.
2. Fabry-Perot filter based solar video magnetograph, 1998, **Shibu K. Mathew**, Arvind Bhatnagar, Debi Prasad C., and Ashok Ambastha, *A&AS* (in Press).
3. A digital imaging multi-slit spectrograph for measurement of line-of-sight velocities on the Sun, 1998, Nandita Srivastava and **Shibu K. Mathew**, submitted to *Solar Physics*.

Contents

1	Introduction	1
1.1	Sunspots as seats of strong magnetic fields	2
1.2	Solar active regions, the center of solar activity	4
1.3	Solar flares	5
1.3.1	Flare in association with the magnetic field	9
1.3.2	Solar flare models	12
1.4	Solar magnetic field measurement	15
1.5	Solar magnetographs	17
2	USO Video Magnetograph	19
2.1	Principle of Solar Magnetograph	19
2.1.1	Zeeman effect	20
2.1.2	Stokes parameters	21
2.1.3	Circular polarization measurement technique	24
2.2	The optical layout of USO magnetograph	26
2.3	Narrow band filter	28
2.3.1	Theory of Fabry-Perot etalons	30
2.3.2	Electro-optic effect in Lithium Niobate substrate	35
2.3.3	Voltage tunable $LiNbO_3$ FP etalon	36
2.3.4	Narrow band filters at CaI 6122 Å and H α 6563 Å	41
2.4	Polarisation analyser	43

2.4.1	KD*P Pockels cell modulator	44
2.4.2	Calculation of quarter wave voltage for KD*P crystal	45
2.4.3	Circular polarisation analyser	46
2.4.4	Quarter-wave retardation, high voltage driver for KD*P electro-optic modulator	47
2.4.5	Bench test of the KD*P modulator	48
2.5	Detector - Cohu 4710 series CCD camera	51
2.6	Image acquisition and processing system	52
2.7	Operational modes of the magnetograph	56
2.7.1	Magnetogram and CaI filtergrams	56
2.7.2	Chromospheric H α filtergrams	58
3	Calibration and Comparison	59
3.1	Calibration of USO video magnetograms	60
3.1.1	Profile line slope method in weak field approximation	61
3.1.2	Calibration of the USO video magnetogram data	61
3.2	Comparison of USO, SOHO/MDI and GONG magnetograms	64
3.2.1	Correlation plot of calibrated USO and SOHO magnetograms	67
3.3	Data acquisition and reduction methodology	68
3.3.1	Format of the raw VMG data and initial processing	68
3.3.2	Magnetic flux, gradient and potential field calculation	69
4	Study of Magnetic Field Evolution	71
4.1	Active region NOAA 7843 observed during February 18-20, 1995	72
4.1.1	Observations	72
4.1.2	Discussions and Results	73
4.1.3	Conclusion	80
4.2	A rapidly evolving active region NOAA 8032 observed on April 15, 1997	81
4.2.1	Observations	81

4.2.2	Discussion and results	84
4.2.3	Conclusion	89
4.3	Active region NOAA 8038 observed during May 10 - 13, 1997	91
4.3.1	Observation	91
4.3.2	Discussion and Results	91
4.3.3	Conclusion	101
4.4	Summary of results	102
5	Summary and Future Plans	104
5.1	Summary	104
5.1.1	Instrumentation	104
5.1.2	Comparison and calibration of VMG	105
5.1.3	Study of evolution of active regions	105
5.2	Future Plans	106
5.2.1	Study of more active regions during the ascending phase of solar cycle 23	106
5.2.2	Calibration of magnetograph using different methods	107
5.2.3	Vector magnetic field measurement	107
A	KD*P High Voltage Power Supply	111
B	VMG Software - C Program	113

List of Figures

1.1	Magnetogram and CaI images of a single sunspot active region NOAA 8038	3
1.2	A two ribbon flare in NOAA 6555	8
1.3	Gold and Hoyle solar flare model	13
1.4	Sturrock and Heyvaerts flare models	14
2.1	Zeeman effect	22
2.2	Stokes parameter	24
2.3	Longitudinal magnetic field measurement technique	25
2.4	Computed Stoke's V parameter for different filter positions	26
2.5	Optical layout of USO Videomagnetograph	27
2.6	The block diagram of the optics, image acquisition system and control electronics	29
2.7	Multiple reflection model for analysing Fabry-Perot etalon	30
2.8	Transmission characteristics of a Fabry-Perot etalon	31
2.9	Basic interferometric arrangement of Fabry-Perot etalon	33
2.10	Constructional details of the solid state $LiNbO_3$ etalon	37
2.11	Experimental arrangement for determining the parameters of FP etalon	38
2.12	The observed and corrected Faby-Perot channel spectrum	39
2.13	Voltage tunability of $LiNbO_3$ Fabry-Perot etalon filter	40
2.14	Passband shift and profile broadening due to FP tilt angle	40
2.15	The measured frequency response of the $LiNbO_3$ Fabry-Perot etalon filter	41

2.16	The transmission peaks of CaI (6122 Å) and H α (6563 Å) pre-filters	42
2.17	Temperature tunability of CaI 6122Å pre-filter	43
2.18	Circular polarisation analyser	48
2.19	Time sequencing diagram showing the synchronisation of image acquisition and KD*P switching	49
2.20	The optical arrangement for the KD*P bench test	49
2.21	Applied voltage versus retardance for KD*P modulator	50
2.22	KD*P modulation at 7Hz	51
2.23	Image acquisition system architecture	53
2.24	Flow chart showing the operation involved in a single cycle of image acquisition	55
3.1	Intensity for different filter position plotted against the wavelength offset . .	62
3.2	The slope of the line profile	63
3.3	The full disk magnetograms used for comparison	65
3.4	Resolution effect	66
3.5	The SOHO and rotation corrected USO magnetograms	67
3.6	Scatter plot made between the USO and SOHO longitudinal magnetic fields	68
4.1	Magnetogram , CaI and H α images of NOAA 7843	72
4.2	Magnetogram , CaI and H α images of NOAA 7843 on 19 Feb 95	74
4.3	Computed potential field overlaid on H α and CaI images, 19 Feb 1995, 05:03 UT	77
4.4	Computed potential field overlaid on H α and CaI images, 19 Feb 1995, 06:54 UT	78
4.5	Computed potential field overlaid on H α and CaI images, 20 Feb 1995, 05:03 UT	79
4.6	NOAA 8032, GOES X-ray flare data on 15 April 1997	81
4.7	The 6122 Å continuum image of the active region NOAA 8032 taken on 15 April 1997	82

4.8	The evolution of longitudinal magnetic field for NOAA 8032	83
4.9	Magnetic field gradient in active region NOAA 8032 taken on 15 April 1997	86
4.10	The calculated potential field for NOAA 8032	88
4.11	The SOHO/EIT image for the active region NOAA 8032	89
4.12	Magnetograms and CaI images of NOAA 8038	92
4.13	12 May 1997, 1N/C1.3 flare	93
4.14	Network flux motion	95
4.15	Proper motion of the network fluxes	96
4.16	Velocity distribution of network magnetic flux elements	97
4.17	Network flux motion	99
4.18	Magnetic flux cancellation	100
5.1	The scheme for vector magnetic field measurement	108
A.1	KD*P power supply	112

List of Tables

1.1	<i>Classification scheme for flares</i>	7
2.1	<i>Narrow band filter parameters</i>	44
2.2	<i>Specifications of the Meadowlark Pockels cell modulator</i>	45
2.3	<i>Specifications of the Cohu 4710 series CCD camera</i>	52
4.1	<i>Flux changes at the location of EFRs</i>	85
4.2	<i>Flux cancellation at the flaring site on May 12, 1997</i>	101
5.1	<i>Full vector magnetic field measurement</i>	109

Chapter 1

Introduction

The sun is a unique object in astrophysics, since it is the only star on which the physical processes can be resolved in some details. The sun can also be seen as a unique plasma laboratory, in which physics at a scale not accessible to experiments in earth laboratories can be explored. Observations show that the atmosphere of the sun is highly structured, governed by an intricate interplay between magnetic forces, turbulent motions, and heating processes. These interactions manifest themselves in various signatures of solar activity such as solar flares, surges, sunspots, and coronal mass ejection, while the key parameter behind these various forms of activity is solar magnetic field.

Solar magnetic field is believed to be generated by dynamo processes operating in its interior, through the amplification of the “seed” magnetic field, as they interact with a turbulent, rotating and electrically conducting medium (Parker 1955; Zeldovich *et al.* 1983; Stenflo 1989; Philips 1995; Stix 1991). The seed magnetic field present in solar interior might be dragged along with the gas when sun was first formed by contraction of a gas cloud. This represents the initial poloidal field. The interaction between rotation and convection leads to a differential rotation, while rotational shear may generate a toroidal field from an initially poloidal field. Active region and sunspots are formed when the strong poloidal field break through the solar surface. Cyclonic turbulence acting on this toroidal field results in the generation of small section of the poloidal field. The turbulent transport spreads this new poloidal field , which has a polarity opposite to the previous

poloidal field. The time scale of this sequence is 11 year. Thus the solar dynamo can be considered as an oscillation between poloidal field and toroidal field with a 22 year period, which produces large as well as small scale magnetic field structures.

Magnetism on the sun occurs on all temporal and spatial scales and most of the observed dynamic phenomenon is directly linked to the magnetic fields. The diameter of the smallest tubes of magnetic flux are at or below the spatial resolution limit of the present day instruments. The field is very weak over major fraction of the solar surface, but has much larger values around a few kilogauss in local spots and flux tubes. Weaker field may result due to the concentration of flux by converging motions whereas the convective collapse transforms the weak concentration in to strong and narrow flux tubes (Stix 1991). The smallest magnetic phenomena which are distinguished in white light images are *pores*. These features are almost as dark as sunspots but have no penumbra and are much smaller, with a size of one or several granules. Normally the magnetic field strength in pore exceeds 1500 Gauss. The concentration of magnetic field due to the supergranular flow is visualised as *network fields*, which also have field strength similar to pores. High resolution magnetograms taken in the quiet sun show intermittent irregular field structures with field strength as low as 100 Gauss, above a nearly field-free background (*cf.* Stenflo 1994; Stix 1991). Another examples of small scale magnetic structures are *filigree* and *facular* points, which are sub-arc second features ($\simeq 0.25$ arc-sec), visible in H α line wings (Dunn & Zirker 1973). Even though the present day magnetograms are unable to resolve the fine structures such as facular points, the count show that the number density of facular points are roughly proportional to the mean magnetic field density (Mehlretter 1974). Thus the average field strength of the facular point deduced from the measurement is found to be around 1000 Gauss, with a diameter of $\simeq 200$ km.

1.1 Sunspots as seats of strong magnetic fields

Sunspots are the largest manifestation of concentrated magnetic field on the solar surface, which normally appear as bipolar structures and are also locations of large scale solar

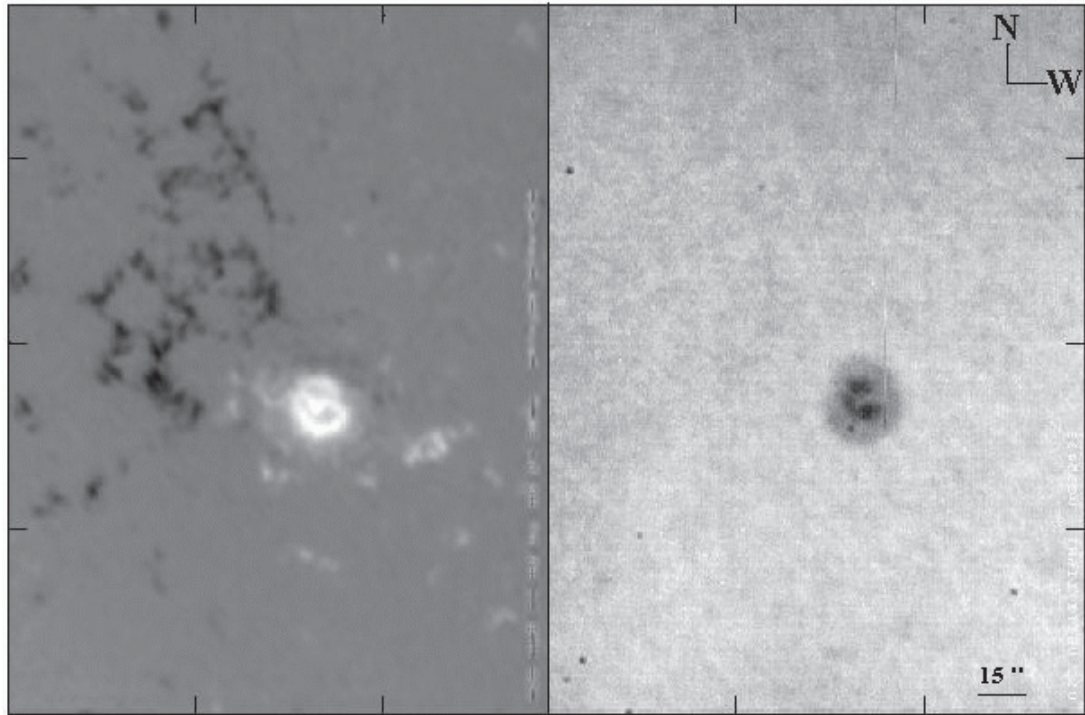


Figure 1.1: *Magnetogram (left) and CaI (right) images of the active region NOAA 8038, observed on May 11, 1997, using USO video magnetograph. This is an example of a single sunspot active region. In magnetogram the white areas denotes areas of positive polarity and black negative polarity.*

activities. It may also be possible that flux of one polarity is more concentrated than that of the other, which leads to the formation of only a single visible spot (*cf* Fig. 1.1). The sunspots are classified according to their unipolar or bipolar configuration, the size and magnetic complexity of the group and the presence or absence of penumbrae (Zirin 1989; Stix 1991). According to the Mount Wilson classification introduced by Hale (1919), α represents a single dominant spot connected to plage of opposite polarity, β a pair of dominant spots of opposite polarity, γ a complex group with irregular distribution of polarities and δ , umbrae of opposite polarity in a single penumbra. The Zürich classification (Waldmeier 1947; Kiepenheuer 1953) depends on the size and complexity, ranging from A for the smallest single spot to F for the largest and most complex group. The classification

in terms of the sunspot complexity is most important in association with the various solar activities.

Most of the sunspots start their life as small pore like bipolar structures (EFR - Emerging Flux Regions), and the orientation of the configuration is roughly east-west on the sun, but the preceding (*p*) spot is usually slightly closer to the equator than the following (*f*) spot. The emergence and subsequent growth of sunspot groups gives strong evidence that a magnetic flux tube is emerging from below. Pores appear, clumped in bipolar form and X-ray or H α emission is seen. The bipolar character of the EFR becomes clear from the H α and X-ray observations, even without magnetic field measurements. The arch-filaments systems clearly mark the loops of the emerging field, and they generally occur in the EFRs (Bruzek 1967; Liggett & Zirin 1985). The evolution of the EFR continues and the pores may become large complex sunspot group or decay after a day or few days. The tendency of new dipoles to pop up in the middle of existing region produce complex γ and δ sunspot groups which are the major sources of solar flares (Zirin & Liggett 1987).

1.2 Solar active regions, the center of solar activity

Sunspot and sunspot groups are only the most conspicuous part of an active region, which comprises of field concentrations out side sunspots and may live much longer than the sunspot it contains. Active regions extend several tens of thousands of kilometers in to the solar atmosphere, above sunspots and have distinct appearance in chromosphere, transition regions and corona. Compared with quiet sun, active regions show enhanced emission over a broad spectral range from soft X-rays to decimetric radio waves. The chromospheric part of the active region is visible in wavelengths of strong Fraunhofer lines notably in H α 656.3 nm and Ca H and K lines in visible spectrum, He 1083 nm in near-IR and Hydrogen Lyman α 121.5 nm in UV. The extension of the active regions into corona can be observed in a number of coronal UV emission lines, soft X-ray and radio wavelengths.

In H α filtergrams the active region consists of bright patches called “plages” around

dark sunspots. In high resolution images fibrils or dark elongated structures can be observed which are normally arranged in a radial or spiral pattern centered on sunspot. There is a close relationship of all chromospheric structures with the photospheric magnetic field. The fibril structures seen in $H\alpha$ connects the area with opposite magnetic polarities and are aligned with local magnetic fields. The dark filament separates areas of opposite magnetic polarities which normally runs parallel to the magnetic inversion line. In corona, active regions are characterised by bright points and loop like structures, when viewed in soft X-ray.

Active region evolves with time through changes in the chromospheric structures and associated magnetic field. An active region first appears as brightening in chromospheric $H\alpha$ and as pores or tiny sunspots in the photospheric white light images. In maps of magnetic fields the active region shows up as compact bipolar magnetic areas, which are commonly called as “emerging flux regions” (EFR). Later these regions develop into full fledged active regions. The newly emerging flux regions in high resolution $H\alpha$ are characterised by low lying filaments known as arch filament systems, which connect the location of opposite polarities directly across the magnetic inversion line. The development of large active regions is associated with increase in the brightness of $H\alpha$ emission, frequent flaring, the change in number and size of sunspots and the complexity of the magnetic field. Magnetic flux distribution and its complexity within an active region is best illustrated by the help of the solar longitudinal magnetograms, usually obtained at the photospheric level. Flux motions, their growth/decay, locations of abnormal polarity distribution, all can be crucial for the flare occurrence in the active regions. These situations are also monitored by video magnetograms (VMGs).

1.3 Solar flares

Solar flares are intense and abrupt release of energy occurring in localised areas of solar atmosphere during the evolution of an active region. The first recorded flare observation was of a white light flare which was made independently by two observers, R. C. Carrington

and R. Hodgson in 1859. Barring the most energetic ones, flares are usually not visible in white light but reserve their strongest enhancement in the spectral lines such as $H\alpha$ and also in EUV and X-ray wave bands. Flares mostly occur when the active region is in a rapidly developing stage; however they also occur when the region is decaying and has lost all its sunspots. As for the sunspots, the frequency of the flare also follows the eleven year activity cycle, but there is often a burst of activity late in the cycle.

The various phenomena accompanying flares may last for as little as a few minutes, but for large flares it may be several hours or even a day or so before everything returns to the pre-flare state. The total energy output in a solar flare varies from 10^{28} ergs in a sub-flare to 10^{32} ergs in a large flare, with about a quarter of the energy appearing in visible wavelengths. Almost the similar amount of energy may appear as energetic particles and mass motions. In literature generally two schemes of flare classification are used: a classification based on the observed area in $H\alpha$ and the soft X-ray flux measured by the onboard SMS-GOES instrument (Table 1.1). In addition to the area, an index is employed in $H\alpha$ classification which signifies the $H\alpha$ brightness of the flare: these are, faint (f), normal (n) and bright (b). The X-ray importance is indicated by a number following one of the letters (B, C, M and X), with the number being a multiplier of $10^{-x} W/m^2$ e.g. C3.2 stands for $3.2 \times 10^{-6} W/m^2$ flare energy in X-rays.

The $H\alpha$ emission during a flare is the strongest and most easy to observe in the visible spectral region. Thus the $H\alpha$ observation provides us with extensive information on low temperature flares. High temporal and spatial resolution $H\alpha$ observations give us most of our information on location, morphology and evolution of flares relative to the underlying magnetic field configuration (Priest 1981; Canfield 1986; Hiei 1987; Zirin 1988; Gaizauskas 1989). The flare appears as brightening of existing plages or formation of new bright areas. $H\alpha$ brightening usually occurs along and in both sides of the magnetic neutral line (Severny 1958). Since the shape of the neutral line depends on the complexity and evolutionary stages of active region, various morphological shape of $H\alpha$ flares are observed (Kurokawa 1988). Zirin (1974) gave a morphological list of flare classification showing six types $H\alpha$ flares,

Table 1.1: *Classification scheme for flares*

<i>Hα flares</i>		<i>X-ray flares</i>	
Importance	Flare area (square degrees)	Importance	Peak flux (watts per m²)
S (Subflare)	Less than 2	B	10^{-7}
1	2.1 - 5.1	C	10^{-6}
2	5.2 - 12.4	M	10^{-5}
3	12.5 - 24.7	X	10^{-4}
4	More than 24.7		

i.e., large two-ribbon flares, explosive flares, surge flares, compact flares, unstable loops, and prominence eruption. An example of a two ribbon flare observed in H α is shown in Fig. 1.2.

In general two kind of magnetic neutral lines are observed in active region, and both are marked by the H α dark fine structures. In one case the transverse component of magnetic field cross nearly perpendicular to the neutral line and are usually marked by arch filament system, threads and arches (Bruzek 1967; Foukal 1971; Prata 1972). In the other the field runs nearly parallel to the neutral line and are marked by dark filaments. This later case indicates slightly sheared neutral line, in which most of the major flares are found to occur (Kurokawa 1988). The flare energy is generally considered to be stored in twisted or sheared magnetic fields. Therefore the observation of the evolutionary changes associated with magnetic field is important to understand the flare process. These evolutionary changes in an active region can be qualitatively examined in the chromosphere from the morphological changes of fine H α fibrils and filaments (Zirin 1971). The fibril structures which connects the opposite polarity magnetic regions provide us with the equivalent of vector magnetic field information in the chromosphere (Foukal 1971). As in the case of

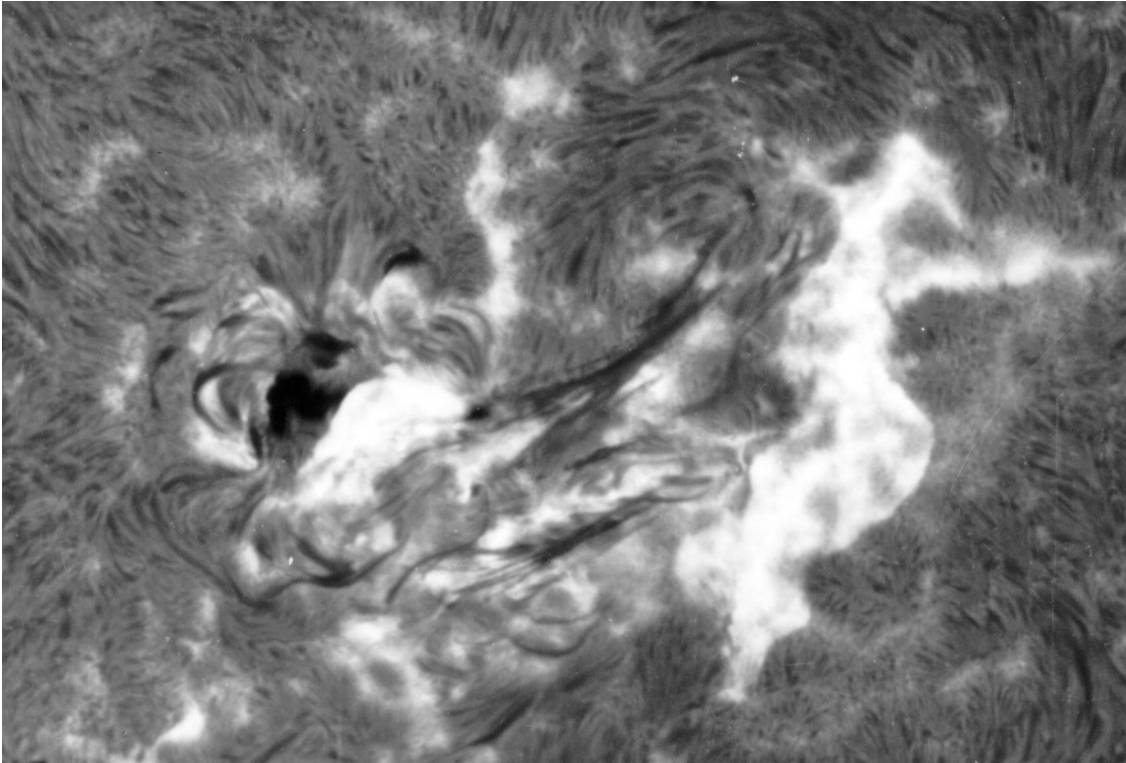


Figure 1.2: *A two-ribbon flare observed in NOAA 6555 on March 23, 1991. Photograph obtained using USO high resolution Spar telescope equipped with an $H\alpha$ 0.5 Å passband Hale-filter.*

vector magnetograms a qualitative measure of the magnetic shear can be estimated by the angle between the $H\alpha$ filamentary structures and polarity boundary line; smaller the angle the stronger the shear. A large number of cases of shear development and associated flaring activity, studied from the evolutionary changes in $H\alpha$ features of active regions and white light images have been reviewed by Kurokawa (1988). Tanaka and Nakagawa (1973) derived a formulation for approximating the force-free energy in terms of fibril geometry and found that sufficient energy was associated with the relaxation observed in a 3B flare to account for the energy released. Tanaka (1976) studied the evolutionary characteristics of three flaring active regions and showed that the $H\alpha$ chromospheric structures tend to be strongly sheared before flares due to foot-point motions associated with the sunspots.

Kurokawa (1987) also found strong shear along the neutral line before a flare, resulted due to the shearing motion of sunspots. He concluded that two types of processes may be responsible for the shear development; a) collision of two sunspots of opposite polarities, and b) the successive emergence of twisted magnetic flux ropes from below the photosphere as first suggested by Tanaka *et al.* (1980). The later type is essential for the build up process leading to major flare activities (Kurokawa 1987; Zirin & Liggett 1987). Reorganisation of fibril structures in the aftermath of flares, in some cases has been also reported which indicate relaxation of force-free magnetic field (Neidig 1979). Another method for magnetic shear calculation from the H α fibril morphology is given by Sivaraman *et al.* (1992) (*see also* Venkatakrishnan 1993).

1.3.1 Flare in association with the magnetic field

The first direct comparison of magnetograms with flare positions were made by Bumba (1958) and Severny (1960). Later similar measurements were carried out by Howard and Babcock (1960) and many others. Some of the early conclusions obtained from their studies were summarized by Svestka (1975). The flare usually starts with two or more bright points or areas. When there are two bright points they appear on opposite sides of the longitudinal magnetic field neutral line (Martres *et al.* 1966; Tang 1986). Usually flares avoid the exact position of the neutral line, whereas one of the initial knots tends to lie immediately adjacent to the neutral line in a region of the greatest longitudinal magnetic field gradient. This happens normally in the case of δ spots where large magnetic field gradients exist. At such abnormal locations opposite polarity umbrae within a penumbra are observed (Mayfield & Lawrence 1985; Patty & Hagyard 1986; Zirin & Liggett 1987; Wang *et al.* 1991; Hagyard 1988). The flare related magnetic field changes were reported by Martres *et al.* (1968). Their study found an active region in which all the flares occurred at the locations where magnetic flux was increasing on one side of the polarity inversion line while it was decreasing on the other side.

In addition to the above mentioned longitudinal magnetic fields, the measurements

of transverse magnetic field in vector magnetograph has shown in many cases that the first $H\alpha$ brightening of flares coincide with the places where the transverse field is nearly parallel to the neutral line. Zirin & Tanaka (1973) reported $H\alpha$ observations of penumbral fibrils which trace the transverse magnetic field running almost parallel to neutral line in a complex flare productive active region, indicating large magnetic stress or shear. Hagyard *et al.*(1984, *see also* Ambastha *et al.*1993) defined shear angle, as the angular difference in the photosphere between the potential field calculated using the line-of-sight magnetic field as the boundary condition, and the observed transverse field (Teuber *et al.* 1977). From the study of an active regions they concluded that the flare sites occur near the locations of higher shear. A threshold value of maximum attainable shear exists, which is found to be $\geq 80^\circ$, above which the flare is triggered. More over, it was noticed that the sheared field exists throughout the flaring period, which suggests that the flare may cause a relaxation of the shear value to some what smaller than the threshold, however further, evolution increases the shear above the threshold. Such a process might cause repeated flaring as seen in many complex active regions. Similar suggestions were made by Moore and LaBonte (1980) based on indirect qualitative observations of large shear at the sites of flare onset. The existence of a critical shear has been also proposed by theoretical studies of Low (1977) and Brian *et al.* (1978). More recently Schmeider *et al.* (1994) have found in a study of NOAA 6659 that the locations of the X-class flares were the sites of strong magnetic shear and also large magnetic field values. Large scale fragmentation, restructuring of the magnetic field topology and fast new flux emergence were observed at the this region. On the basis of above observations they suggested that, the fragmentation and continuos restructuring of the magnetic field topology might have led to the shearing of the field lines. Thus the energy storage took place over the field lines, while the emerging fluxes might have triggered for the release of the energy. In apparent contradiction to the above requirement of maximum shear and magnetic field and its association with the flare sites, Fontenla *et al.* (1995) found that large flares in NOAA 6555 occurred near regions of enhanced magnetic shear, but not necessarily at the

location of maximum shear or maximum magnetic field.

There are a number of observations suggesting new flux emergence as the cause for the flare trigger. Association of frequent occurrence of flares with emerging magnetic flux regions (EFR) were reported by Rust (1972, 1974) in number of cases. Vorpal (1973) examined a moderately active sunspot group, and found that almost all the flares occurred in the neighbourhood of EFRs. Examples of EFR triggered flares have been also reported by Wang *et al.* (1991), where they observed X-class flares near the sites of EFR. A recent paper by Debi Prasad *et al.* (1998) discussed an unambiguous case of a EFR triggered X-class flare in the active region NOAA 6555.

Apart from the EFR associated flares, there are also cases of flares without them. Martin *et al.* (1984) reported flares which occurred in the absence of EFRs. They analysed a decaying active region and found that all its observed flares began at locations where magnetic flux was cancelling (Martin *et al.* 1985). Cancellation of the flux is mutual decrease of magnetic flux at the boundary between closely spaced opposite polarity magnetic fields. By analysis of several active regions, they suggested that flux cancellation is more important in its association with flares, while other associations could be considered to be special cases (Livi *et al.*, 1989). Wang & Shi (1993) suggested that emergence of new flux and flux cancellation with existing flux driven due to the flux emergence are wholly inseparable, elementary process in the active regions for the occurrence of flares.

From these observations it is clear that, the production of flares is related to some particular properties of the photospheric magnetic field configurations and its evolution. Some of these suggested properties are; strong magnetic fields, large gradients, emergence of new flux regions, sunspot motion and the flux cancellation. All the above mentioned properties derive from statistics over many active regions, and a particular flaring active region may not show all of these properties. It may also happen that some active regions having all the above properties produce no large flares. The identification of the relevant properties is important for developing and testing theoretical models and forecasting flare activity. Some of the flare models, having a basis on the observed magnetic field

configuration, are discussed in the following section.

1.3.2 Solar flare models

There are four fundamental questions to which the reply should be found in any flare theory. These pertain to: the source of flare energy, the storage of flare energy, the sudden release of energy, and the heating and acceleration mechanisms. The fact that flare mostly occur in active regions indicates that the pre-flare conditions include increased value of magnetic field and temperature relative to the quiet solar atmosphere. It can be readily shown from the energetic conditions that the only source of solar flare energy can be in the stressed magnetic field, ruling out other sources such as thermal, gravitational potential and nuclear energy which are all found to be inadequate (Tandberg & Emslie 1988). A force-free field configuration which is current carrying and non-potential can store excess of magnetic energy. To make this energy available for the flare production, the field configuration should be such that, the fieldlines must reconnect. A part of the field disappears and its energy is transformed into other energy forms. More over the configuration must be metastable and the annihilation must proceed at such a rate that all the flare energy is released within 10^2 to 10^3 seconds of observed flare time-scales.

A variety of reconnection models have been proposed over the years. According to Gold and Hoyle (1960), the magnetic flux tubes are twisted at its feet with the twist distributed evenly along the whole tube. The twist may be caused by the rotation at the feet of the flux tube due to the convective motions. The degree to which the flux tube is twisted is the measure of excess energy stored in the tube compared to the energy content in an untwisted potential field configuration, where in static case the field must be force-free. This means that the electric current \mathbf{j} in the tube are very nearly parallel to the magnetic field \mathbf{H} , in order to make $\mathbf{j} \times \mathbf{H} = 0$. Two tubes close to each other with the twist and field in opposite sense and direction must attract each other, forming a neutral point (Fig.1.3). At this neutral point the magnetic field lines get reconnected and a part of the magnetic field is annihilated. Even though this model could explain the occurrence of frequent small

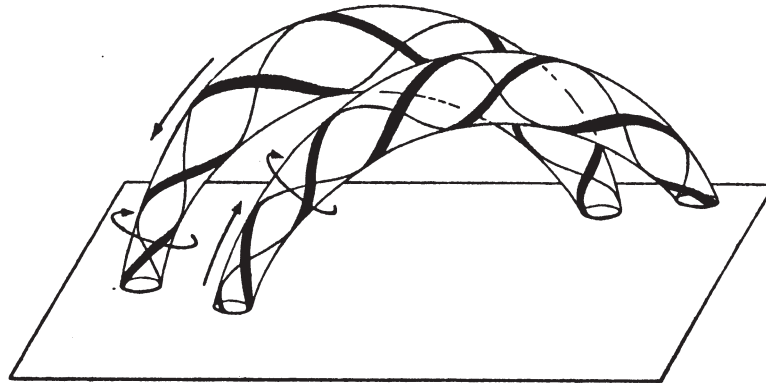


Figure 1.3: *Gold and Hoyle solar flare model. Two bundles of lines of force, both twisted up, here the longitudinal field is in opposite directions (indicated by arrows) and the twisting has occurred in opposite sense.*

flares but it needed additional assumptions in order to stabilise the configuration to have any major flares.

In Alfvén and Carlqvist (1967) model, the effect of electric current is considered for the instability in a single twisted flux tube. Since the storage of magnetic energy can be accomplished only through departures from a potential field, any deviation from the potential field is associated with the existence of currents. Both measurements and theoretical considerations indicate that the flare energy must be stored as magnetic energy in the current system. Another model proposed by Tanaka and Nakagawa (1973) make use of the shear in the magnetic field to store the excess energy required for the flare. The stored energy is calculated from the deviation (shear) of visible $H\alpha$ fibrils from the calculated potential field lines (Zirin & Tanaka 1973). This model is supported by the observation of shear relaxation in some rare instances (Neidig 1979). Low (1982) suggested that the storage of energy in the magnetic field can be thought of as a slow process where the field evolves through a sequence of force-free configuration, each time ending up in high energy state. This slow process is driven by the motions in the low atmosphere where the energy of plasma motion dominates the magnetic energy and the field lines are swept passively

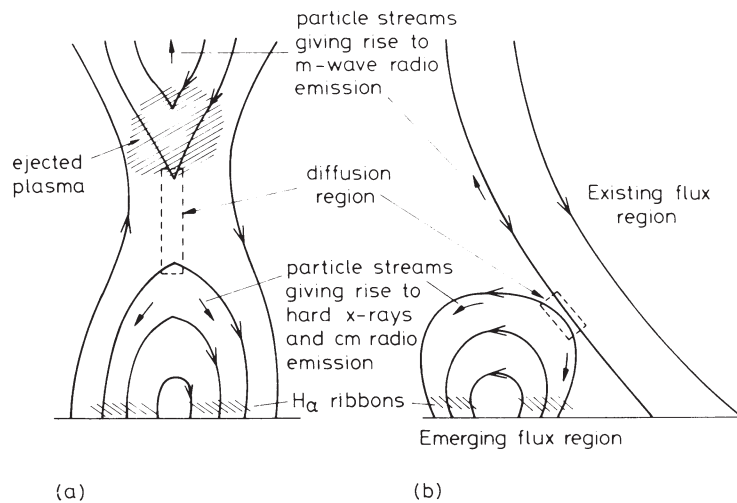


Figure 1.4: (a) *Sturrock* and (b) *Heyvaerts* solar flare models.

along with plasma. Even though this process itself does not produce flares, it sets the stage for the onset of flares. In the flare model by Sturrock (1972) a current sheet can be built from a force-free field configuration (Fig. 1.4(a)). The initial potential field configuration is distorted by the photospheric motions leading to the production of force-free configuration. If the photospheric motions are sufficiently large the energy stored in the field may ultimately exceed the energy of an open field configuration which becomes unstable or metastable. In such cases the configuration can change into open field and can bring the oppositely directed field lines close together to make neutral point or current sheet. The oppositely directed field lines merge and annihilate one another and the released magnetic energy is transformed to heat and kinetic energy of the plasma. The pre-flare activation and disruption of the filaments support this model.

Heyvaerts *et al.* (1977, see also Priest & Heyvaerts 1974) put forward another model, which could explain the *pre-flare*, *impulsive*, *flash*, and the *main phases* of flare, in connection with the emergence of magnetic flux loops from below the photosphere, to an already existing magnetic region. According to their model, during the pre-flare heating

phase continuous reconnection occurs in the current sheet that forms between the new and old flux (Fig. 1.4(b)). When emerging flux loops reach a critical height, typically in the upper chromosphere, the current density exceeds the value for occurrence of plasma microinstabilities and result in impulsive and flash phase. The onset of a turbulent electrical resistivity in sheet causes it to expand rapidly, and the particles are accelerated to high energies and escape along the field lines, down to the lower chromosphere and producing $H\alpha$ emission knots. Here the attainment of the critical current density is regarded as the trigger for the flare, while in main phase a new steady state of magnetic field reconnection is reached with much larger current sheet. This model could explain different types of flares; strong flux emergence near a simple sunspot field should lead to a *simple loop flare* and sometimes surges, whereas the magnetic loops may press against the twisted field which surrounds an active region filament, and produce *two ribbon flare*. Number of observations supporting the emergence of new flux region for the triggering of solar flare have been reported in literature (Rust & Bridges 1975; Kurokawa 1987; Debiprasad *et al.* 1998).

1.4 Solar magnetic field measurement

Form the above mentioned flare models, it is clear that, it is important to have good temporal and spatial resolution magnetic field measurements for the understanding of solar flares and related activities. The history of magnetic field measurement go back to 1908, when Hale discovered magnetic field in sunspot through Zeeman splitting of spectral lines. Since then, solar magnetic field have been explored with increasingly sophisticated techniques. A major contribution in this direction was due to Harold Babcock who built a photoelectric magnetograph in 1953 which could measure weak magnetic fields. Prior to that only strong magnetic fields present in the sunspots could be detected. In his instrument, Babcock used an electro-optic crystal in front of the spectrograph which converted the circular polarisation of the incoming beam into two mutually perpendicular linear polarisations, so that the polarisation property of the Zeeman splitted component could

be measured. The Babcock instrument measured the magnetic field at a single point on the sun, where as Leighton (1959) introduced a modified instrument which was capable of making two dimensional magnetograms, using a spectroheliograph and photographic subtraction method. The photographic detector was replaced by a double array of diodes by Livingston *et al.* (1971), providing a way of simultaneously measure the magnetic field over upto 512 points along the slit. Since then, good quality full-disk magnetograms have been obtained by this instrument, which is still operational at National Solar Observatory /Kitt Peak (NSO/KPNO), with a modified design (Jones *et al.* 1992).

Another major improvement in the magnetic field measurement was achieved by Leighton and Smithson (Smithson 1973), when they used a narrow band Lyot filter and a Vidicon camera instead of the spectrograph and diode array. This equipment was first installed at Big Bear Solar Observatory (BBSO) which was capable of obtaining a two dimensional magnetic field map, avoiding the tedious and time consuming task of adding up the linear scan results as in the case of spectrograph based instruments. This instrument opened up a new era of filter based, high temporal and spatial resolution magnetographs.

The above mentioned magnetographs measure only the longitudinal component of the magnetic field. Bruckner developed a filter based vector magnetograph at Marshall Space Flight Center (MSFC/NASA), which could measure longitudinal as well as the difficult to measure transverse component of the solar magnetic field (Hagyard *et al.* 1982). Besides the above mentioned instruments mostly operating in USA, a few more magnetographs are now operational. Those are; a filter-based vector magnetograph at Huairou Observing Station, Beijing Astronomical Observatory (Ai & Hu 1986); National Astronomical Observatory of Japan, Mitaka (Sakurai *et al.* 1992), and a spectrograph based Stokes polarimeter at Mees solar observatory, Hawaii (Mickey 1985).

Although only large magnetic fields could be detected during the early stages, the measurement gave enormous amount of information on magnetic polarities of the sunspot, flux distribution, and polarity reversals. The development of magnetographs which use the polarisation property of the Zeeman splitted components increased the sensitivity of

the magnetic field measurements. This enabled the researchers to study the magnetic field evolution associated with a specific active region and related activities. The limitation in temporal and spatial resolution of the spectrograph based magnetographs were overcome by the introduction of filter based-magnetographs. The increased temporal resolution made possible the study of rapid evolution of active regions. The real time image acquisition systems and CCD cameras have improved the S/N ratio and provided high quality images with good spatial and temporal resolution.

1.5 Solar magnetographs

As discussed before, for the study of flare related magnetic field changes, one needs to know magnetic configuration of active regions, the polarity distribution of the emerging flux regions, location of flux emergence field gradients and shear development. The longitudinal magnetic field, white light and $H\alpha$ observations are very useful for studying the evolution of active regions. Evolution of flare producing active region is usually very rapid, therefore in order to have proper correlation of the flare activity and magnetic field evolution it is required to have simultaneous chromospheric $H\alpha$, magnetograms and white light observations. The high resolution $H\alpha$ observations obtained at USO in the initial period were interpreted using magnetograms from other observatories such as MSFC, BBSO and Beijing Astronomical Observatory, since no magnetograph facility were available in the longitudinal belt between Japan and Europe. The large time gap between USO flare observations and the magnetograms from the above observatories rendered the analysis of our data very difficult and at times erroneous. Therefore it was considered essential to build a solar magnetograph at USO for reliable interpretation of solar photospheric and chromospheric phenomenon in relation with solar magnetic field.

A digital, filter-based video magnetograph (VMG) has been designed, fabricated and successfully installed as a part of this Ph.D. thesis. This is the first such system in the country. Polarisation property of the Zeeman splitted component of a suitable photospheric absorption line (CaI 6122 Å, Landé factor 1.75) is used for the measurements. This in-

strument is capable of providing near simultaneous observations of longitudinal magnetic field, chromospheric $H\alpha$ (6563 Å) and photospheric CaI (6122 Å) observations using the same telescope and back-end equipment. The use of a voltage tunable Fabry-Perot narrow band filter, instead of conventional birefringent Lyot filter makes the near simultaneous multi-wavelength observations possible. A fast switchable KD*P electro-optic modulator is used to analyse the polarisation property of the solar light, which allows data acquisition at the video rate. This minimizes the atmospheric seeing and telescope tracking effects. A real time data acquisition system is employed to acquire and process the data, which makes possible the averaging of a large number of frames in a short interval of time, thus providing a good signal-to-noise (S/N) ratio and sensitivity.

Comparison of our magnetograms with corresponding data obtained by space based Solar Orbiting Heliospheric Observatory/Michelson Doppler Instrument (SOHO/MDI) shows very good agreement over the magnetic features. For converting the measured Stokes V intensity values into magnetic field strength in Gauss, we have derived a calibration parameter using the profile line slope method. A scatter plot has been made between calibrated SOHO/MDI and USO magnetograms, which show very little scatter, indicating the reliability of our measurements. We have discussed the principle of the Solar magnetograph and the technical details of USO magnetograph in chapter 2. Calibration method and comparison of USO magnetograms with those obtained by other existing equipments are reported in chapter 3.

During the ascending phase of cycle 23, February 1995 and April-May 1997, we have taken simultaneous photospheric, chromospheric and magnetic field data for three active regions NOAA 7843, NOAA 8032 and NOAA 8038. These active regions had shown EFR related flaring activities. A good amount of flux motion and cancellation was also observed from detailed studies. Analysis of the data has been done to understand the magnetic field evolution and related flare activity of these regions. The details of the analysis and results are also presented in the thesis. Further plans for upgradation and increase of instrumental accuracy is described in chapter 5.

Chapter 2

Udaipur Solar Observatory Video Magnetograph

2.1 Principle of Solar Magnetograph

In the presence of magnetic field the absorption lines originated at the solar surface is split and polarised due to Zeeman effect. For weak magnetic fields of the order of a few Gauss, the direct measurement of Zeeman splitting requires very high resolution spectrograph. Therefore, modern solar magnetograph mostly use the polarisation property of the Zeeman split components for the measurement of magnetic field. Basically there are two types of magnetographs; spectrograph based and filter based. First method employs a spectrograph for isolating the absorption line and a scanning system for building up the image. In the second method a narrow band filter is used to isolate the line and the area of interest is imaged on a detector. In both methods polarisation measurement is done for the determination of magnetic field. Both the instruments have their own merits and demerits. The spectrograph based magnetograms are superior for their high spectral purity compared to the filter based magnetographs. However in order to obtain a magnetogram over a large active region the spectrographic method is considerably time consuming. In other words filterbased magnetographs are fast instruments and can be employed for the study of rapidly evolving magnetic field structures in the active regions. The spectrographic method requires a precise matching of the measurements made at various positions of the

slit thereby degrading the spatial resolution of the magnetogram (Zirin 1995). This limits the capability of the spectrographic method from resolving the rapid temporal and spatial changes which are important for the solar flare studies. Another important aspect is the high signal-to-noise ratio, which can be attained by the filter based magnetograms by acquiring a large number of frames in a short interval of time. Considering all the above facts, the filterbased magnetographs are more suitable instruments for observing rapidly evolving active region where the absolute field strength is not of interest but the spatial resolution and temporal evolution are important. Therefore we preferred to build a video magnetograph employing imaging filtergraph mode over the spectrographic method.

Before discussing the USO VMG instrument, we describe the Zeeman effect, polarisation properties (Stokes parameters) of the light coming from the Sun and the measurement technique in detail.

2.1.1 Zeeman effect

In the case of weak magnetic field L , S , J and M_j are the quantum numbers which denote the state of an atom, where L is the total orbital angular momentum of the electrons, S the spin and J the total angular momentum. M_j is the magnetic quantum number which determines the component of the total angular momentum in any one direction. M_j can adopt the values $-J$ to $+J$, i.e., $(2J + 1)$ values excluding zero, while J itself can have the values from $|L - S|$, $|L - S| + 1, \dots, L + S$. All the M_j states have the same energy in the absence of magnetic field, i.e. $B = 0$ while degeneracy is removed if field strength $B \neq 0$. For the energy shifts and the resulting Zeeman displacement the Landé factor g of each state is important which is given by

$$g = 1 + \frac{J(J + 1) + S(S + 1) - L(L + 1)}{2J(J + 1)}. \quad (2.1)$$

If g and g' , M and M' be the Landé factor of the lower and upper states of transition considered, then the displacement of the line from its unmagnetic position λ_0 can be derived as,

$$\lambda - \lambda_0 = \frac{e}{4\pi m_e C} g^* \lambda^2 B \quad (2.2)$$

where $g^* = g M - g' M'$, is the effective g factor of transition. When λ is measured in Å and B in gauss then,

$$\lambda - \lambda_0 = \Delta\lambda = 4.67 \times 10^{-13} g^* \lambda^2 B \quad (2.3)$$

If we do not consider the spin, i.e. $S = 0$ then g will have the value 1. If both states have $S = 0$ then the selection rule for M_j , i.e., $\Delta M_j = -1, 0, +1$ yields $g^* = -1, 0, +1$. The result is the normal Zeeman splitting or “Lorentz” triplet. In general there is Zeeman multiplet or “anomalous” splitting. Since most solar lines are broad, the multiplets normally are not resolved and thus for weak fields we can consider the multiplet as if it was a triplet. The effective g factor is then calculated from the g^* values of the contributing components, where each component is given weightage according to their intensity

Zeeman triplet consists of two shifted σ and one unshifted π component. When the line-of-sight is in the direction of the magnetic field only the σ components are visible. This is the longitudinal Zeeman effect. These σ components are circularly polarised in opposite sense. When the observation is made perpendicular to the magnetic field all the three components are visible. The π component is linearly polarised perpendicular to B and the σ components are linearly polarised parallel to B as shown in Fig. 2.1. Solar spectral lines are doppler and collision broadened, therefore the field strength must be more than 0.15T for Zeeman splitting to be recognised. However the Zeeman components are polarised regardless how small the splitting is. Around 1950, H. W. Babcock and K. O. Kiepenheuer first investigated the possibility of separating Zeeman components by means of polarimetric methods.

2.1.2 Stokes parameters

The polarization of the light can be described in terms of four parameters called Stoke’s parameters (*cf.* Stix 1991). The light propagating in z -direction have the electric field vectors in the x - y plane:

$$E_x = \xi_x \cos \phi \quad (2.4)$$

$$E_y = \xi_y \cos(\phi + \epsilon) \quad (2.5)$$

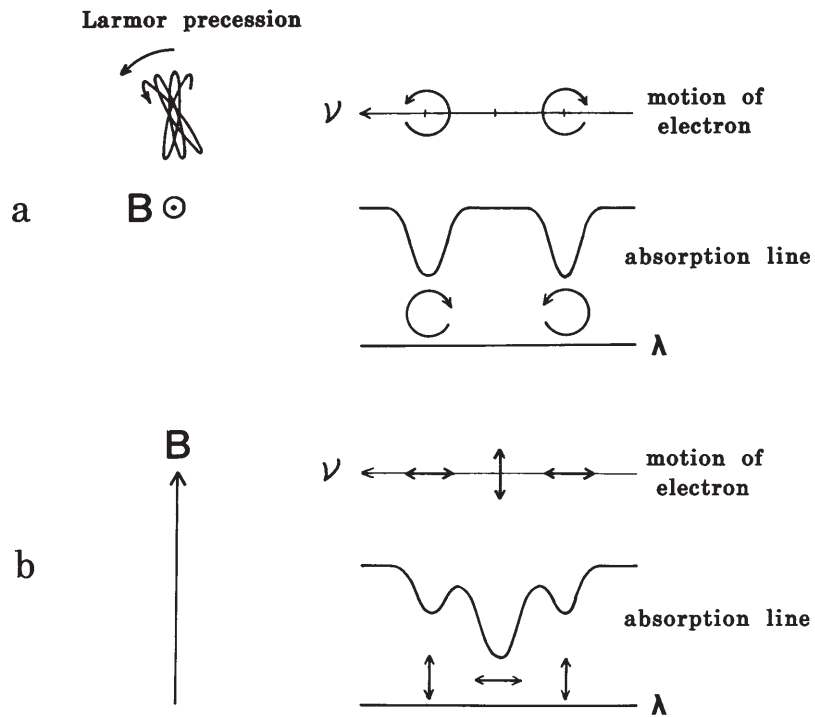


Figure 2.1: Longitudinal (a) and transverse (b) Zeeman effects. In longitudinal case the absorption line is split into two σ components which are circularly polarised in opposite sense. In transverse case the central π component and the two σ components are linearly polarised orthogonal to each other (Sakurai 1989)

where $\phi = \omega t - kz$ and ϵ is the phase difference between E_x and E_y . ξ_x and ξ_y are constant amplitudes which together with ϵ describes the state of polarisation of the wave which is elliptical in general. For the complete representation of the polarised light, four parameters connecting ξ_x , ξ_y and ϵ were introduced by G. G. Stoke which are,

$$I = \langle \xi_x^2 + \xi_y^2 \rangle \quad (2.6)$$

$$Q = \langle \xi_x^2 - \xi_y^2 \rangle \quad (2.7)$$

$$U = 2 \langle \xi_x \xi_y \cos \epsilon \rangle \quad (2.8)$$

$$V = 2 \langle \xi_x \xi_y \sin \epsilon \rangle \quad (2.9)$$

where $\langle \rangle$ represents time averages taken over a period of observation. For unpolarised light all the transverse directions are equal and all phases ϵ between 0 to 2π occur with same probability so that $Q = U = V = 0$. In other words completely polarised light is characterised by ϵ and the ratio of ξ_x and ξ_y . Some of the representative cases are shown in Fig. 2.2. The Stokes Q and U represents the states of linear polarization where as V corresponds to circular polarization. V is positive for right- circular polarization and negative for left-circular polarization as viewed from the observer. The Stokes I represents the total intensity.

By solving the equations of radiative transfer of the Stokes profiles and considering the weak field approximation ($\delta\lambda_B \ll \delta\lambda_D$, where $\delta\lambda_B$ is the separation between the Zeeman components and $\delta\lambda_D$ is the doppler width of the spectral line) the parameters Q, U and V can be related to the magnetic field by the following formulae (Sakurai 1989; Stix 1991),

$$V \sim B_l \quad (2.10)$$

$$Q \sim B_l^2 \cos 2\chi \quad (2.11)$$

$$U \sim B_l^2 \sin 2\chi \quad (2.12)$$

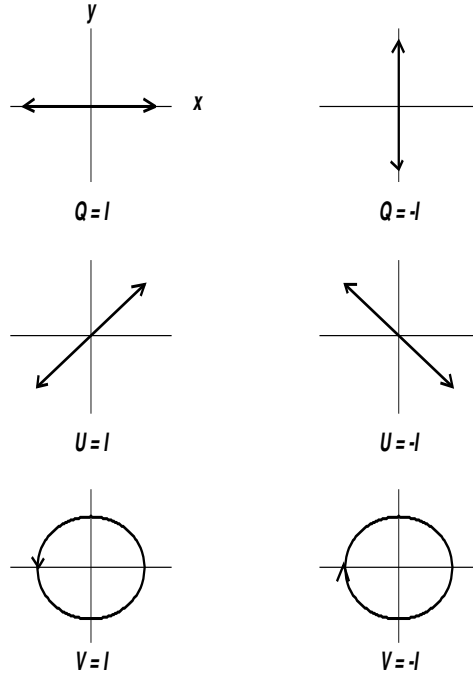


Figure 2.2: *Stokes parameter Q , U and V for perfectly polarised light. The arrows represents the trajectory of the electric field as viewed from the observer (Sakurai 1989).*

where B_l and B_t are the line-of-sight and the transverse components of the magnetic field respectively, and χ is the angle between the transverse field and the direction of measurement of positive Q .

2.1.3 Circular polarization measurement technique

Filter-based magnetographs use the polarisation property of the Zeeman components for the measurement of magnetic field. As discussed in the previous section, for the line-of-sight magnetic field the σ_1 and σ_2 components are oppositely circular polarised. Since the σ_1 and σ_2 components are shifted in wavelength, choosing the polarisation (left or right) entering the system essentially corresponds to shifting of the lines. This principle is used in our video magnetograph (VMG). We have selected CaI 6122 Å solar photospheric absorption line for the magnetic field measurements. This line has a g factor of 1.75 and line width of 200 mÅ. The low temperature sensitivity, higher line depth and no blend are the preferred characteristics of this line. For restricting the measurement at this particular

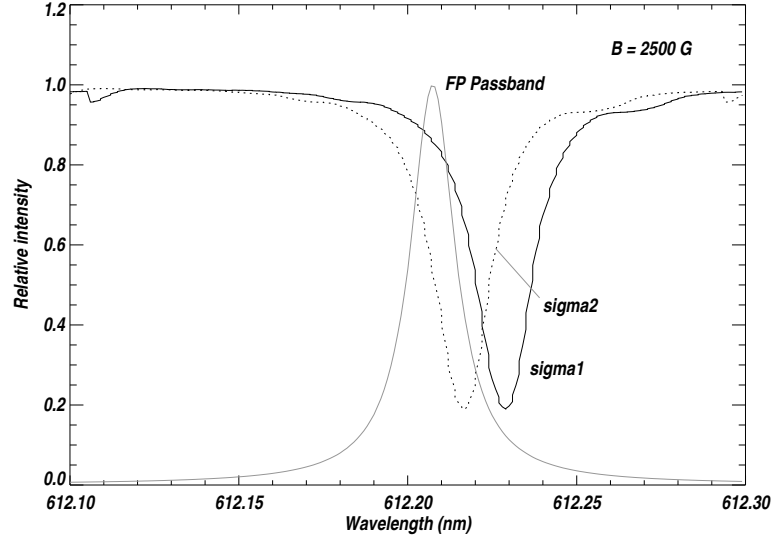


Figure 2.3: *Longitudinal magnetic field measurement technique. The dark solid and dotted curves shows the Zeeman components, where as the light solid curve shows the Fabry-Perot passband tuned at $140 \text{ m}\text{\AA}$ away from the line centre (6122.231\AA).*

wavelength, a narrow band filter of $160 \text{ m}\text{\AA}$ is tuned at the blue wing of this line, $140 \text{ m}\text{\AA}$ away from the line centre as shown in Fig. 2.3. This allows the measurement of the Stokes parameters integrated over a narrow band of wavelength. Tuning the filter to the blue wing of the line reduces the background variations since the increase in brightness due to the rising granules is cancelled by the shift of the absorption line. In order to fix the wavelength offset the V parameter is computed for a range of magnetic field strengths and filter positions. Fig. 2.4 shows the degree of polarisation V/I plotted against magnetic field strengths for different filter positions. From the plot it is evident that tuning the filter $140 \text{ m}\text{\AA}$ away from the line centre gives maximum signal with an acceptable linear response in V parameter over a field strength up to around of 1500 Gauss . We are measuring only the V component of the Stokes parameters in the VMG mode. The measurement is done by making two images of the active region; one in the left and other in the right circular polarisations, which are $I + V$ and $I - V$ images. A polarisation analyser (*cf.* Section 2.3)

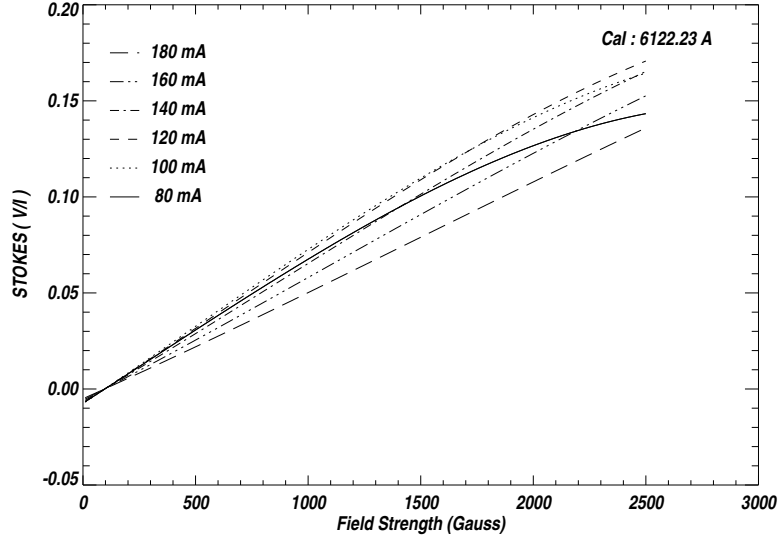


Figure 2.4: *Computed Stoke's V parameter for different filter positions along the line profile. The maximum signal and acceptable linearity of V parameter is obtained when the filter is tuned at 140 mÅ away from the line centre.*

is used for switching between left and right-circular polarisation images. To increase the signal-to-noise ratio (SNR) a suitably large number of $I + V$ and $I - V$ images are made alternately which are added separately. These images are then subtracted and normalised to get the Stokes V parameter i.e.,

$$\frac{V}{I} = \frac{\Sigma(I + V) - \Sigma(I - V)}{\Sigma(I + V) + \Sigma(I - V)} \quad (2.13)$$

The detailed description of the instrument for the magnetic measurement is given in following sections.

2.2 The optical layout of USO magnetograph

Fig. 2.5 shows the optical layout of the USOs Video Magnetograph. The solar light is fed to VMG through a Zeiss made coude telescope. The telescope has a 15 cm doublet primary lens with a focal ratio $f/15$. Two mirrors placed at the arms of the telescope reflect the beam to a fixed coude focus. The back end equipments are installed on a separate

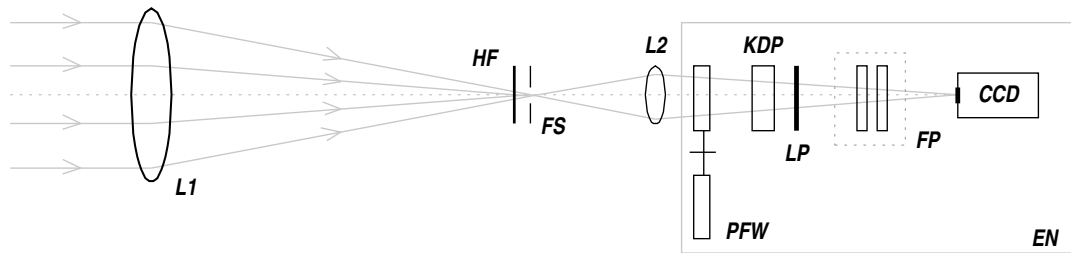


Figure 2.5: *Optical layout of USO Videomagnetograph. L1- 6 inch objective doublet, HF - heat filter, FS - field stop, L2 - relay lens, PFW - pre-filter wheel, KDP - variable quarter-wave plate, LP - linear polariser, FP - Fabry-Perot etalon, CCD - Cohu CCD camera, EN - enclosure.*

platform behind the telescope. The image rotation caused due to the Coudé movement of the telescope is corrected off-line by software. The anti-symmetrical reflections made by the two mirrors present in the optical path make the polarisation on reflection negligible. The telescope is equipped with a guider which provides correction signal to the RA (Right Ascension) and DEC (Declination) differential drive motors. The telescope makes a solar image of 22mm diameter at the focal plane. The image is enlarged by another lens $L2$ which slows down the beam to $f/43$, and a solar image of 60 mm is formed at the detector plane. The lens $L2$ is mounted on a motorised x-y stage which is capable of moving the lens to one of the two predetermined positions for magnetogram or chromospheric observations. A field stop (FS) selects the area-of-interest on the solar disk which just fits on the CCD chip. This reduces the scattered light by blocking unwanted part of the image from reaching the optics behind. A heat filter HF is placed just in front of the field stop to avoid the heat load on the optics. Moreover the heat filter reflects back the IR part of the spectrum which could otherwise saturate the CCD chip. The filter wheel fixed behind the lens $L2$ holds two pre-filters enclosed in separate temperature controlled ovens. These pre-filters are tuned to CaI 6122 Å and H α 6563 Å by adjusting the oven

temperature. A computer interface controls the relay-motor mechanism attached to the filter wheel and the relay lens movements. This mechanism allows the selection of the pre-filters and thus the wavelength by software during observations. The selected pre-filter can be introduced into the beam with in a few seconds (~ 10 -15 seconds) making it possible to have the near simultaneous magnetogram and chromospheric observations. The KD*P electro-optic modulator installed behind the pre-filter acts as a variable quarter wave plate. The high voltage terminals from the KD*P are connected to the switchable power supply. A linear polarizer LP , mounted on a wheel at the back of KD*P crystal acts as an analyser of the incoming circular polarisation. The linear polariser is rotated away from the beam during $H\alpha$ observations for better image contrast. The position of the polariser wheel is detected by the opto-isolators and is controlled by software. The voltage tunable narrow band Fabry-Perot etalon filter FP is placed in front of the CCD camera. The field-of-view at the CCD is equivalent to $\sim 4 \times 3$ minutes-of-arc on the sun. Fig. 2.6 shows the schematic of the optics, image acquisition and controlling system. All the components mounted on the optical bench are enclosed in a sealed enclosure to avoid the consequences due the change in the out side temperature.

2.3 Narrow band filter

A voltage tunable solid-state Fabry-Perot (FP) etalon instead of a conventional birefringent Lyot filter is used in our video magnetograph. The FP etalon has the advantage of fast tunability over birefringent filters which is very useful when the instrument is used in multiwavelength observations. More over this property is essential for making the velocity maps (Dopplergrams) which needs fast switching of the wavelength between the blue and red wings of the spectral line (Rust 1985; Rust *et al.* 1986). Lower temperature-sensitivity of the etalon (which is 0.024 \AA per $^{\circ}\text{C}$ in our etalon) compared with birefringent Lyot filter (0.4 \AA per $^{\circ}\text{C}$) is also an added advantage. One disadvantage of the etalon is that its transmission profile falls slower than the Lyot profile which results in lower image contrast. However this difficulty can be reduced by using two etalons in tandem giving

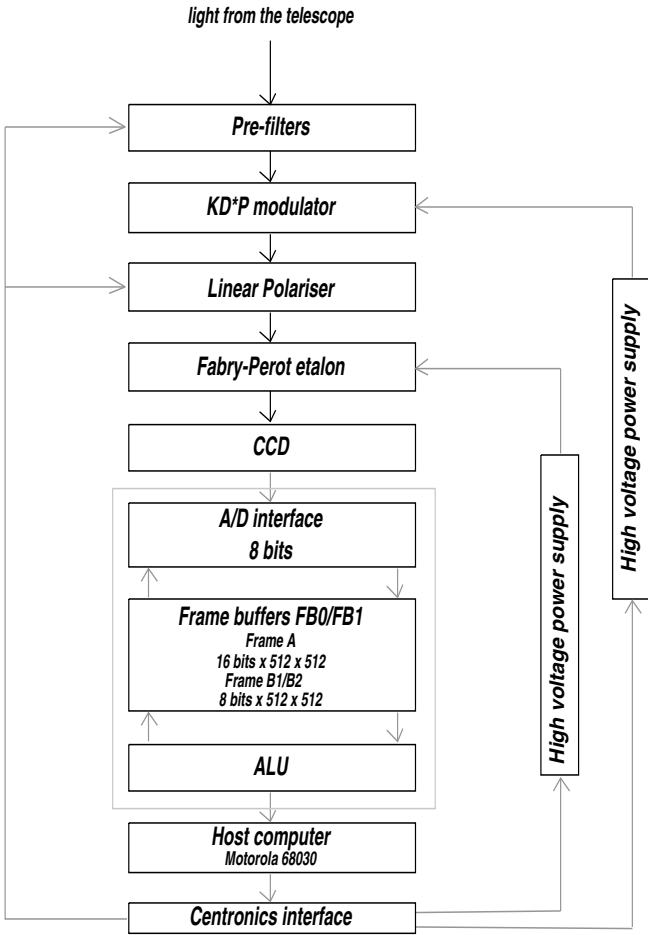


Figure 2.6: The block diagram of the optics, image acquisition system and control electronics.

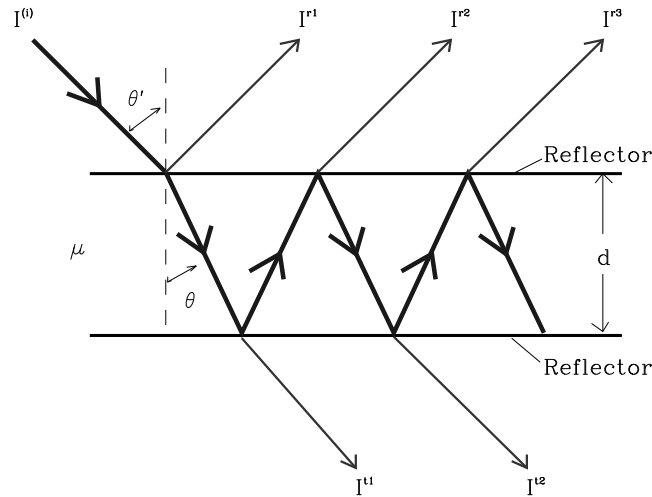


Figure 2.7: Multiple reflection model for analysing Fabry-Perot etalon. $I^{(i)}$, I^r , I^t are the incident, reflected and transmitted waves respectively.

contrast comparable to that attainable with Lyot filter. Although the Lyot filter gives better contrast, its use of a large number of calcite or quartz elements (~ 9 to 20 in the Lyot filter) introduces larger image distortion than the single 0.175 mm wafer used in the solid-state FP etalon. Further Lyot filters are more expensive than etalon filters - a Lyot filter having similar band pass can be 8 to 9 times expensive than FP etalon filter.

2.3.1 Theory of Fabry-Perot etalons

Fabry-Perot (FP) Etalon is a device based on the theory of multiple beam interference. A standard FP etalon consists of two partially reflecting surfaces separated by a narrow cavity as shown in Fig. 2.7. The light transmitted by the first surface may be reflected or transmitted by the second surface and so on. The reflected and transmitted rays combine constructively when the number of waves in the cavity is an integer. If $I^{(i)}$ is the incident intensity, the intensity of the light transmitted by the device $I^{(t)}$ is given by the Airy

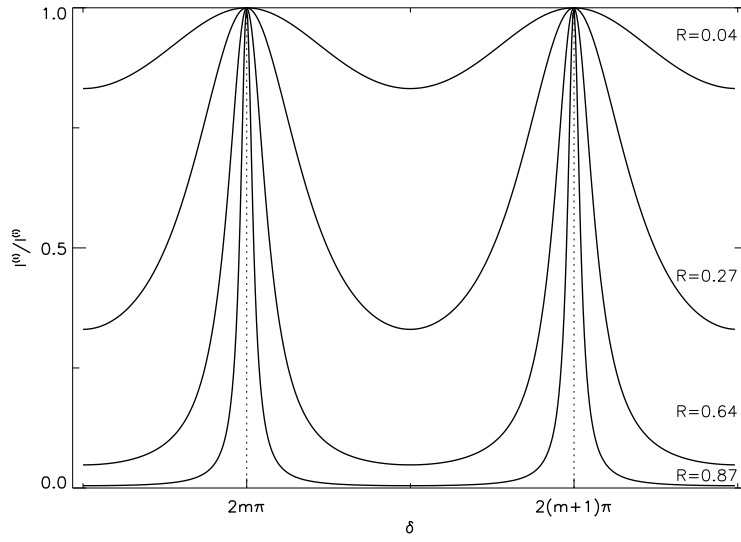


Figure 2.8: *Transmission characteristics of a Fabry-Perot etalon for a uniform change of phase difference δ at different reflectivity (R) values.*

formula as,

$$I^{(t)} = \frac{I^{(i)}}{1 + F \sin^2(\delta/2)} \quad (2.14)$$

where

$$\delta = \frac{2\pi}{\lambda} 2\mu d \cos \theta + \epsilon \quad (2.15)$$

and

$$F = 4R/(1 - R)^2 \quad (2.16)$$

Here, R is the reflectivity of the surfaces, d the width of the cavity, μ the refractive index within the cavity, θ the angle between the rays and the normal to the reflective surfaces, λ the wavelength, ϵ is the phase changes on reflection and δ the phase difference between two consecutive rays. Fig. 2.8 shows the relative transmitted intensity versus the phase difference δ for different reflectivities. The maximum transmission is obtained

when $\delta = 2\pi m$ where m is the order of interference given by,

$$m = \frac{2\mu d \cos \theta}{\lambda} \quad (2.17)$$

which is an *integer* and represents the number of wavelengths within the cavity. When R approaches to unity the pattern of the transmitted light consists of narrow bright fringes on an almost completely dark background. As evident from above, the narrow bright fringes are obtained only for chosen wavelengths, therefore the FP etalon can be used as a narrow band filter. The “full width at half maximum” (FWHM), $\delta\lambda$ of the fringes can be derived from (2.14) as

$$\delta\lambda = \frac{4}{\sqrt{F}} \quad (2.18)$$

The sharpness of the fringes increases with the increase in reflectivity which can be conveniently expressed as the ratio of the separation between successive fringes(i.e., free spectral range or FSR, equal to 2π) to the FWHM; which is called reflective finesse N_R ,

$$N_R = \frac{FSR}{\delta\lambda} \quad (2.19)$$

By putting the value of FSR and FWHM, N_R can be obtained as,

$$N_R = \frac{\pi\sqrt{R}}{(1-R)} \quad (2.20)$$

for ideally flat etalon plates. However in practice, the instrumental profile and the line-width will be modified by the plate imperfections. For a λ/q plate flatness the “flatness finesse” is given by,

$$N_F = q/2 \quad (2.21)$$

and the net finesse as,

$$N_I = \left(\frac{1}{N_R^2} + \frac{1}{N_F^2} \right)^{-1/2} \quad (2.22)$$

Fig. 2.9 shows the basic interferometric arrangement of an FP etalon. From the cylindrical symmetry of the arrangement about the optic axis, bright circular rings of angular radius θ are observed at the focal plane of the lens $L2$ where the angular radius of n^{th} ring, θ_n is given by,

$$\theta_n = \cos^{-1}(\lambda/2\mu d)n \quad (2.23)$$

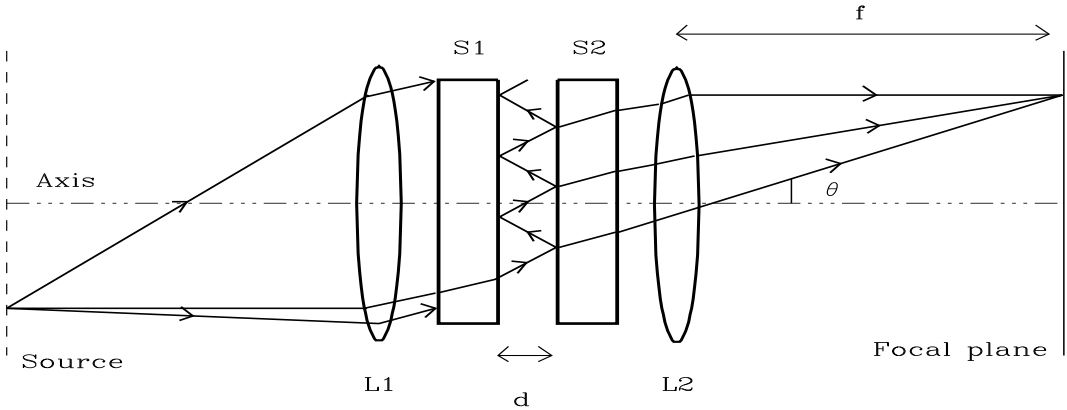


Figure 2.9: An illustration of the basic interferometric arrangement with plane parallel optical surfaces $S1$ and $S2$. Light from the source is collected by the lens $L1$. Successively reflected waves are superposed by lens $L2$ and fringes are formed in the focal plane (Vaughan 1989).

Here we are neglecting the phase change ϵ on reflection which merely serves to displace the fringe pattern and it is equivalent to a small change in the effective value of the etalon spacing d . The radius of the circular fringes are obtained as $f\theta_n$ where f is the focal length of the lens $L2$. For a perfect non-absorbing and non-scattering reflecting film, we have $T + R = 1$. If there is an absorption or scatter loss A in the reflecting surfaces then $T + R + A = 1$ and the peak maximum and minimum intensities are given by,

$$I_{max} = I_0 T^2 / (1 - R)^2, \quad (2.24a)$$

and

$$I_{min} = I_0 T^2 / (1 + R)^2 \quad (2.24b)$$

The ratio of the peak maximum to minimum intensities is called the extinction or contrast ratio given by,

$$\frac{I_{max}}{I_{min}} = \frac{(1 + R)^2}{(1 - R)^2} \quad (2.25)$$

For $R = 0.94$ it corresponds to an extinction factor of 10^3 which is not high enough to study a weak spectral feature in the presence of bright one. The contrast ratio can be increased by using two or more etalons in tandem or multipassing a single etalon. FP etalon can be used as a narrow band filter if its FSR is larger compared with the FWHM. There are different kinds of etalons depending on the spacer used between the reflective faces. In astronomy usually the air spaced etalons are used, which have the advantage of a fast wavelength tunability. The wavelength tunability in this kind of filters is achieved by changing the effective spacing between the reflective faces. The disadvantage with these etalons on the other hand is that it requires sophisticated mechanisms to maintain parallelism of the plates and to compensate for the air pressure and temperature changes. In solid etalons the spacer used is a transparent substrate, whose faces are highly polished and coated with high reflectivity films. Here, after the fabrication the task of maintaining parallelism is not a problem and tuning of the filter can be achieved by changing the temperature of the substrate or by tilting. These are too slow processes compared with the fast wavelength tunability of air spaced etalons.

In USO video magnetograph we used a solid-state etalon, substrate of which is made up of electro-optic Lithium Niobate ($LiNbO_3$) crystal. The refractive index of this crystal can be varied by applying a high voltage across the crystal. The electro-optic property of the crystal is used to make the etalon voltage tunable. The tunability is fast and is comparable with piezo-electric, air spaced etalons. In the next section the electro-optic property of the Lithium Niobate crystal is discussed.

2.3.2 Electro-optic effect in Lithium Niobate substrate

$LiNbO_3$ is a birefringent crystal with linear electro-optic properties. The linear electro-optic effect is the change in the indices of the ordinary and extraordinary rays that is caused and is proportional to the applied electric field. The birefringence of a crystal can be conveniently expressed in terms of index ellipsoid (Yariv 1991). In the principal axes system for a uniaxial crystal with its c-axis (optic axis) parallel to the z-direction (i.e., $n_x = n_y = n_o$ the ordinary refractive index, $n_z = n_e$ the extraordinary refractive index) the index ellipsoid can be written as,

$$\frac{x^2 + y^2}{n_o^2} + \frac{z^2}{n_e^2} = 1 \quad (2.26)$$

Also the changes in refractive index due to an electric field is given by,

$$\Delta \left(\frac{1}{n^2} \right)_i = \sum_{k=1,2,3} r_{ik} E_k \quad (2.27)$$

where E_k ($k = 1, 2, 3$) represents the components of the applied electric field and r_{ik} ($i = 1, 2, \dots, 6$, $k = 1, 2, 3$) are the elements of the electro-optic tensor. The linear electro-optic tensor for $LiNbO_3$ is of the form

$$[r] = \begin{bmatrix} 0 & -r_{22} & r_{33} \\ 0 & r_{22} & r_{13} \\ 0 & 0 & r_{33} \\ 0 & r_{51} & 0 \\ r_{51} & 0 & 0 \\ -r_{22} & 0 & 0 \end{bmatrix} \quad (2.28)$$

In the presence of an applied electric field along the z-direction the index ellipsoid will be modified as described below,

$$\frac{x^2 + y^2}{n_0^2} + \frac{z^2}{n_e^2} + r_{13}E_z x^2 + r_{13}E_z y^2 + r_{33}E_z z^2 = 1 \quad (2.29)$$

or

$$x^2 \left(\frac{1}{n_0^2} + r_{13}E_z \right) + y^2 \left(\frac{1}{n_0^2} + r_{13}E_z \right) + z^2 \left(\frac{1}{n_e^2} + r_{33}E_z \right) = 1 \quad (2.30)$$

and the refractive index for x, y and z polarized wave can be obtained as,

$$n_x = n_0 - \frac{1}{2}n_0^3 r_{13}E_z \quad (2.31)$$

$$n_y = n_0 - \frac{1}{2}n_0^3 r_{13}E_z \quad (2.32)$$

$$n_z = n_e - \frac{1}{2}n_e^3 r_{33}E_z \quad (2.33)$$

So, for the wave propagation along the z-axis the change in the refractive index Δn_0 for an applied voltage V is given by,

$$\Delta n_0 = -\frac{n_0^3 r_{13} V}{2d} \quad (2.34)$$

where d is the thickness of the crystal, and r_{13} for $LiNbO_3$ is 8.6×10^{-12} meter/volt.

2.3.3 Voltage tunable $LiNbO_3$ FP etalon

A 0.175 mm thick $LiNbO_3$ crystal wafer is used as the substrate in the USO's FP etalon supplied by CSIRO, Australia. The free aperture of this etalon is around 60mm. Both the sides of the wafer are polished to an accuracy of $\lambda/200$ or better. Highly reflective dielectric coatings of SiO_2 and Ta_2O_5 are deposited on both sides of the crystal. The dielectric coatings are 93% reflecting over a wavelength range of 5000 - 6700 Å, which limits the operating range of the filter. A conductive coating of ITO (Indium Tin Oxide) is also deposited for the application of electric field across the crystal. High Voltage terminals made of gold wires are bonded to the ITO coating with the help of silver epoxy. Two wedge shaped glass windows protect the wafer. Fig. 2.10 shows the constructional details of the etalon.

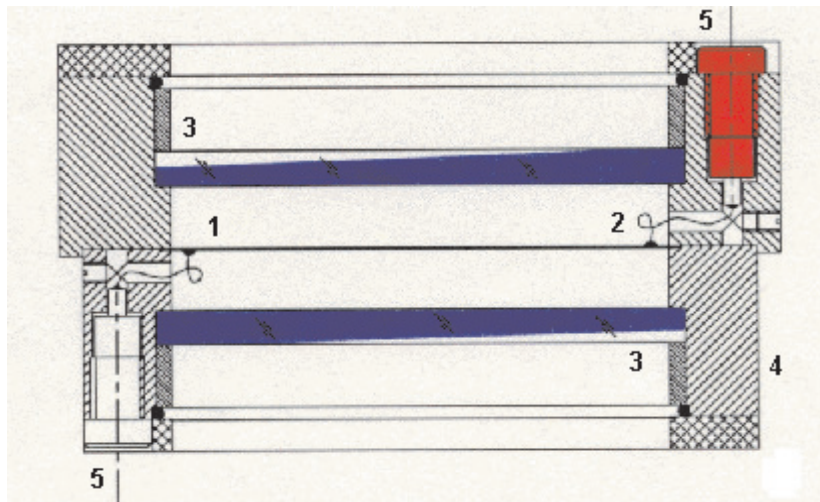


Figure 2.10: *Constructional details of the solid state LiNbO_3 etalon. 1. Thin LiNbO_3 wafer coated with SiO_2 , Ta_2O_5 and Indium Tin Oxide (ITO), 2. Electrodes fixed on the surface of the wafer for high voltage application, 3. High quality AR coated protective windows, 4. Perplex enclosure, 5. High voltage connector.*

A bench test was performed for determining different parameters of the FP etalon. For this purpose the etalon was placed in front of the USO Littrow spectrograph. This spectrograph has a dispersion of around 0.047 \AA per pixel at the CCD plane. Fig. 2.11 shows the experimental set-up used for the bench test. The channel spectra were digitised and stored by an on-line image acquisition system. Later the images were analysed using IDL software to determine important parameters of the etalon. Fig. 2.12 (a) and (b) show the channel spectra recorded near CaI 6122 \AA and $\text{H}\alpha$ 6563 \AA lines. The obtained channel spectrum is corrected for the instrumental profile. An Airy fit is carried out to the corrected channel spectrum. Fig. 2.12 (c) and (d) show the respective corrected profiles. The FSR, FWHM and the finesse are calculated from the corrected profiles; the FSR was found to be 4.22 \AA and 5.05 \AA at CaI and $\text{H}\alpha$ wavelength, respectively. The calculated values of FWHM are 160 m\AA for CaI and 220 m\AA for $\text{H}\alpha$. These values of FSR and FWHM give finesse as ~ 26 and ~ 23 at CaI and $\text{H}\alpha$ lines. To determine the voltage tunability of the etalon, channel spectra were recorded for a range of voltages starting

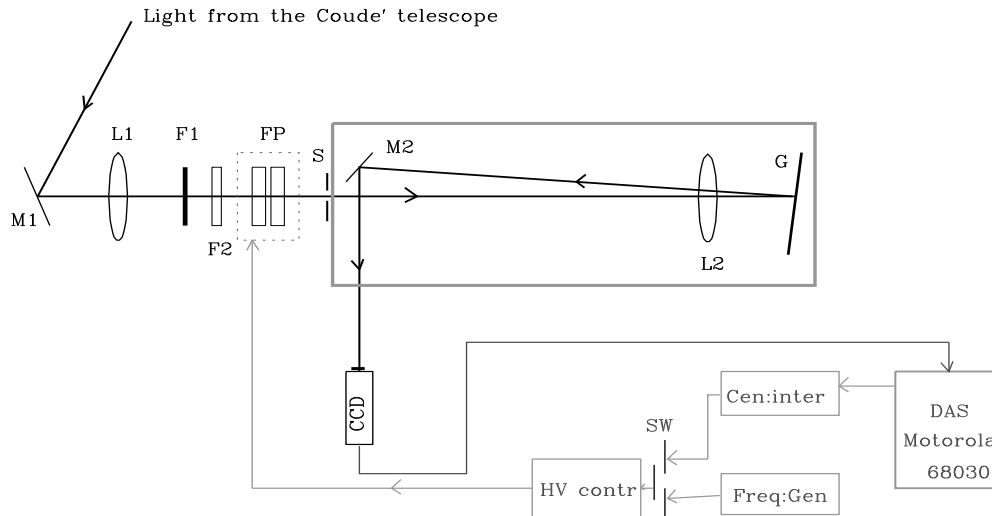


Figure 2.11: *Experimental arrangement for determining the parameters of FP etalon: M = Mirror, G = Grating, L = Lens, F1 = Heat filter, F2 = Pre-filter, FP = Fabry-Perot etalon, S = Entrance slit, SW = Change over switch, cen:inter = computer interface, DAS = Data acquisition system, HV contr = High voltage controller, Freq:Gen = Frequency generator, CCD = CCD camera.*

from -3000 to 3000 Volts in steps of 100 Volts. The wavelength shift is measured in all the channels for the average shift. The shift in the wavelength for the applied voltage is plotted in Fig. 2.13. From the figure it is evident that the wavelength shift is a linear function of the applied voltage. The average tuning constant is found to be $\sim 0.45 \text{ \AA}$ per 1000 volts. Moreover the voltages required for the positioning of the channels at CaI 6122 \AA and H α 6563 \AA line are also measured for a particular temperature and tilt. FP etalon is sensitive to both temperature and tilt. The channel peak shifts to redward of the spectrum as the temperature is increased. A value of 0.024 \AA per $^{\circ}\text{C}$ at CaI 6122 \AA is derived for the temperature sensitivity of the etalon from our measurements. A constant temperature oven is constructed in-house to enclose the etalon to avoid wavelength shift due to the change in the ambient temperature. The temperature stability of the oven is better than $\pm 0.05 \text{ }^{\circ}\text{C}$, which yields a wavelength stability of $\sim 5 \text{ m\AA}$. The etalon is very sensitive to tilt which produces broadening of the passband and shift towards the blue side of the spectral line profile. Fig. 2.14 (a) and (b) show the pass band shift and broadening respectively

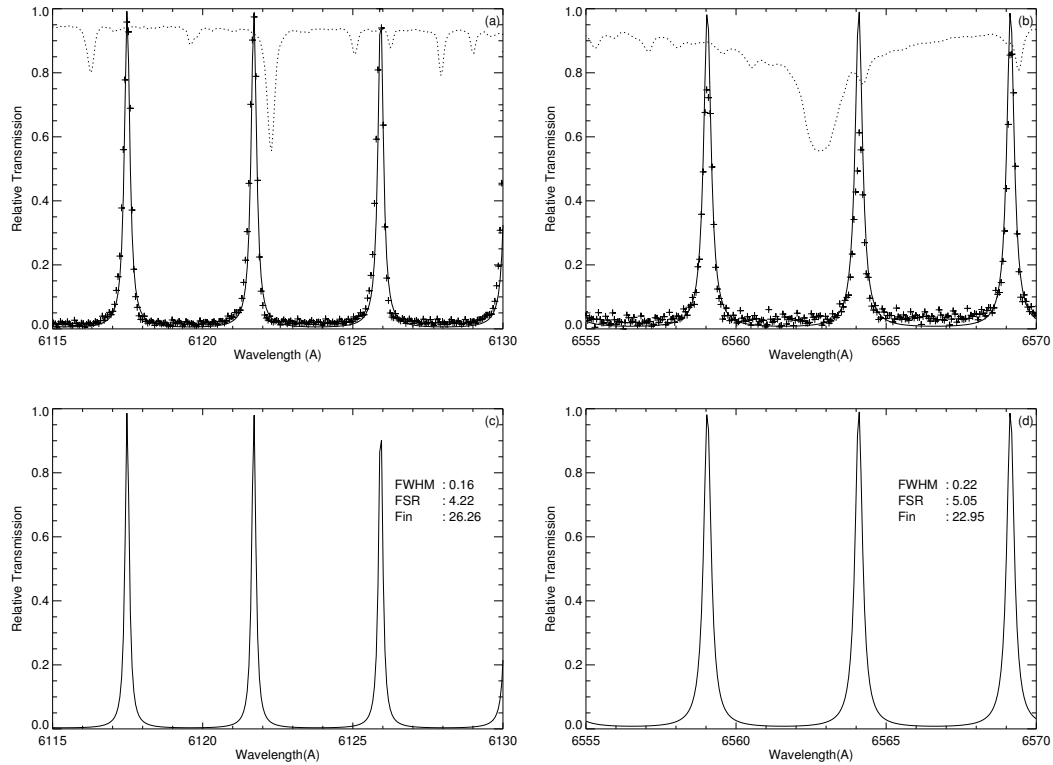


Figure 2.12: *The observed and corrected Fabry-Perot channel spectrum. (a) and (b) shows the observed channel spectrum near 6122 Å and 6563 Å respectively. The dotted line shows the solar spectrum, the prominent absorption lines in (a) and (b) are CaI at 6122 Å and H α at 6563 Å. (c) and (d) show the channel spectrum corrected for the spectrograph instrumental profile.*

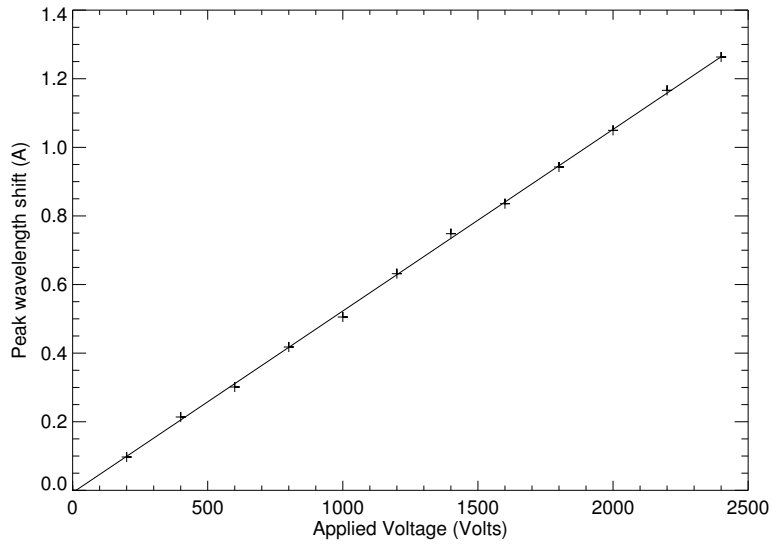


Figure 2.13: Voltage tunability of $LiNbO_3$ Fabry-Perot etalon filter

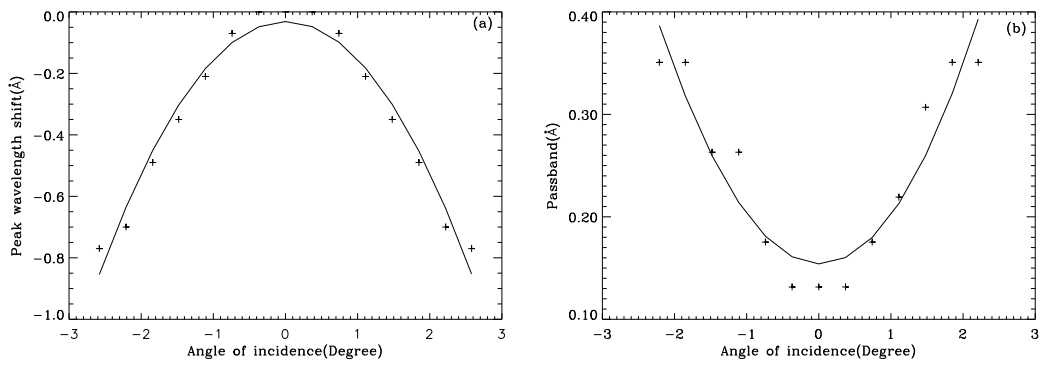


Figure 2.14: Passband shift and profile broadening due to tilt angle.

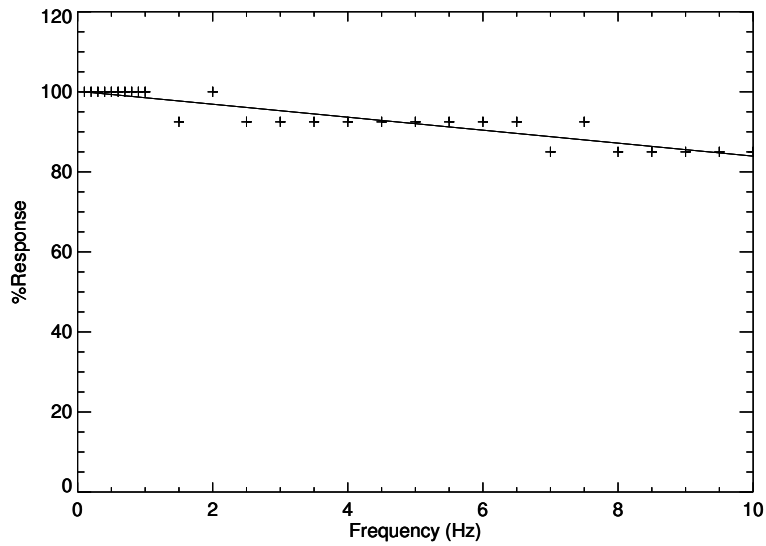


Figure 2.15: *The measured frequency response of the LiNbO_3 Fabry-Perot etalon filter.*

due to the tilt. Tilts greater than 2° generally produce unacceptable broadening.

The frequency response of the etalon is also determined by applying a square voltage of 1200 volts at different frequencies. The frequency response is measured by averaging 255 frames in video rate to get the two peaks corresponding to the minimum and maximum of the applied voltages. The shift between these two peaks is reduced when the frequency is increased, and the above measured shift is taken as the percentage response. Fig. 2.15 shows the percentage frequency response for different frequencies. By knowing the percentage response at different frequencies the correction voltage can be calculated when FP is operated at high frequencies.

2.3.4 Narrow band filters at $\text{CaI } 6122 \text{ \AA}$ and $\text{H}\alpha 6563 \text{ \AA}$

The combination of two interference pre-filters with the tunable FP etalon yields two narrow band filters at selected wavelengths - we have used one at the photospheric $\text{CaI } 6122 \text{ \AA}$ line and the other at the chromospheric $\text{H}\alpha 6563 \text{ \AA}$ line.

The pre-filters help to block the unwanted channels in the transmission peaks of the

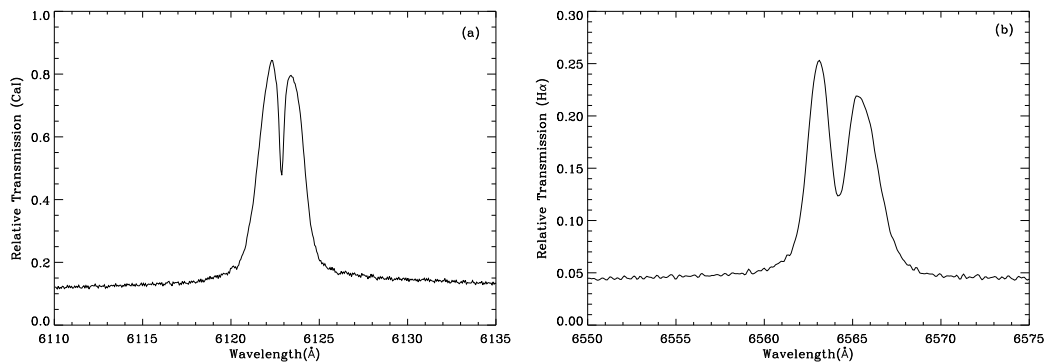


Figure 2.16: *The transmission peaks of CaI (6122 Å) and H α (6563 Å) pre-filters.*

etalon. Fig. 2.16 (a) and (b) show the transmission peaks of the CaI and H α pre-filters. The centre of the transmission peaks are tuned to the CaI and H α lines. The band width of the CaI and H α pre-filters are 2.68 and 3.58 Å respectively. However the combination of the pre-filter and etalon gives a much narrower passband of around 160 mÅ at CaI line and 220 mÅ at H α line. We use the narrow band filter at CaI 6122 Å for the photospheric magnetogram observations where as that at H α 6563 Å is used for solar chromospheric observations. The pre-filters are sensitive to temperature and tilt angle, however we can profitably use these parameters to tune the pre-filters over a range of wavelengths. As in the case of FP etalon, an increase in the temperature shifts the transmission peak to redward side of the spectrum, while a tilt increase shifts it to the violet side. Fig. 2.17 shows the temperature dependability of the CaI 6122 Å pre-filter. Both the pre-filters are also enclosed in separate constant temperature ovens to avoid any wavelength shift due to the variation in the ambient temperature. Table 2.1 summarises the properties of the etalon and pre-filters. The process of tuning the narrow band filter to different wavelengths consists of choosing the appropriate pre-filter and applying the required voltage to the etalon. Tuning of the filter is done with great accuracy using the Littrow spectrograph. The etalon is placed in front of the spectrograph and appropriate voltage is applied to get

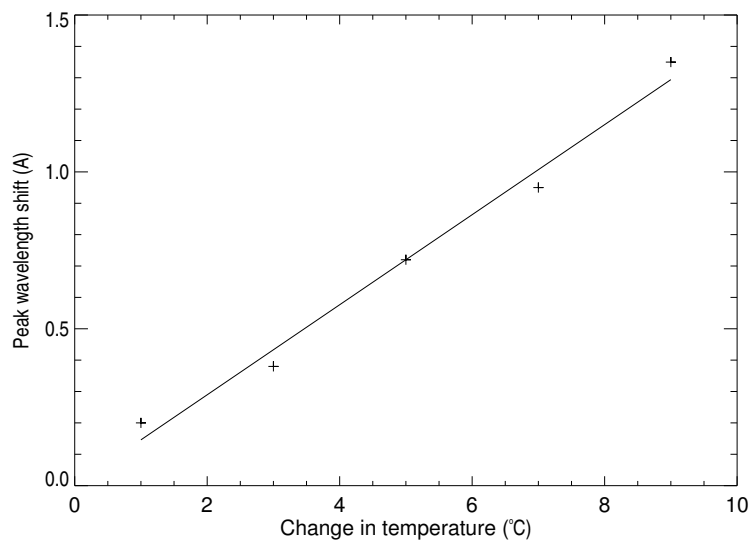


Figure 2.17: *Temperature tunability of CaI 6122Å pre-filter.*

the required solar spectral line in one of the channels.

The operations such as changing the pre-filters and application of the high voltage to the FP are controlled by a Motorola 68030-based workstation computer in a programmed manner. Switching from one wavelength to another thus takes only a few seconds, making it possible to obtain the near-simultaneous observations in magnetograph and H α filter-graph modes. If the wavelengths are within the range of the pre-filter used, then the switching process takes only a few milliseconds.

2.4 Polarisation analyser

A KD*P variable quarter wave plate and a linear polariser constitute the circular polarisation analyser for the longitudinal magnetic field measurements. The KD*P electro-optic modulator is capable of switching between $\pm\lambda/4$ wave retardation on the application of ± 2100 Volts. The fast switching property of the KD*P modulator allows the data acquisition in video rate, which minimises the seeing and the telescope tracking effects. More over it eliminates mechanical movements required for switching between polarisation as in

Table 2.1: *Narrow band filter parameters*

Etalon Properties		
Substrate material	:	Z-cut LiNbO ₃
Substrate diameter	:	73.6 mm
Usable aperture	:	60mm
Etalon thickness	:	0.175 mm
Coating	:	Multilayer broad band, hard ion assisted deposition of SiO ₂ , Ta ₂ O ₅ , ITO
Reflectivity	:	0.95 at $\lambda = 6120 \text{ \AA}$
Voltage sensitivity	:	0.45 \AA per 1000 Vol
FP filter parameters		
	CaI 6122 \AA	H α 6563 \AA
Free Spectral Range(\AA)	:	4.22
Passband (\AA)	:	0.16
Finesse (FSR/FWHM)	:	26
		5.05
		0.22
		23
Pre-filter parameters		
Central wavelength (\AA)	:	6122.23
Bandwidth (\AA)	:	2.68
Peak transmission (%)	:	33.50
Ambient temperature ($^{\circ}\text{C}$)	:	43.0
		6563.98
		3.58
		23.03
		43.0

the case of rotating fixed $\lambda/4$ plates.

2.4.1 KD*P Pockels cell modulator

The variable quarter wave plate is a longitudinal Pockels cell , made of z-cut potassium di deuterium phosphate (KD*P) crystal, procured from Meadowlark optics. The Pockels cell has transparent indium tin oxide electrodes applied to the faces of the protective windows adjacent to the optical faces of the z-cut crystal. This electrode produces a uniform electric field normal to the faces of the KD*P crystal. The use of a thin crystal (less than 3mm) makes these cells suitable for the application in noncollimated imaging beams slower than $f/20$ (West 1989). The clear aperture of the KD*P is 2.5 cm and the transmission is 92%

or better at 622 nm. Table 2.2 gives the specification of the Pockels cell. The next section describes the theory of operation of the KD*P crystal as a quarter wave plate.

Table 2.2: *Specifications of the Meadowlark Pockels cell modulator*

Material	:	KD*P crystal between fused silica substrates, mounted in housing
Retardance range	:	0 - 320 nm (approximate)
Transmitted wave front distortion	:	1/4 wave peak to valley at 633 nm
Clear aperture	:	2.5 cm
Transmission	:	92% or better at 633 nm
Angular acceptance	:	2° half cone angle
Reflection	:	1.6% per surface
Quarter-wave voltage	:	2200 volts or less at 633 nm (linear with wave length), varies with temperature
Maximum voltage	:	4500 volts (must be AC with no DC bias)
Response time	:	100 nanoseconds
Nominal capacitance	:	40 pf
Resistance	:	greater than 1000 megohms
Cell dimensions	:	1.25" <i>O.D</i> × 0.54" deep
Temperature range	:	5° to 35° C

2.4.2 Calculation of quarter wave voltage for KD*P crystal

KD*P crystal is a negative uniaxial crystal. The crystal has a four-fold axis of symmetry (optic or z -axis) and two mutually orthogonal two-fold axes of symmetry. The two-fold axes of symmetry designated as x and y axis lie in the plane normal to c-axis. The electro-optic tensor for the KD*P crystal is of the form,

$$[r] = \begin{bmatrix} 0 & 0 & 0 \\ 0 & 0 & 0 \\ 0 & 0 & 0 \\ r_{41} & 0 & 0 \\ 0 & r_{41} & 0 \\ 0 & 0 & r_{63} \end{bmatrix} \quad (2.35)$$

The index ellipsoid for KD*P with the applied electric field E_z parallel to c-axis can be obtained as,

$$\left(\frac{1}{n_0^2} - r_{63}E_z\right)x^2 + \left(\frac{1}{n_0^2} + r_{63}E_z\right)y^2 + \frac{z^2}{n_e^2} = 1 \quad (2.36)$$

where x and y are the principal axes, 45° rotated from the original position due to the application of the electric field. The refractive index for the rays which have field components along the principal axes can be written as,

$$n_x = n_0 + \frac{n_0^3}{2}r_{63}E_z \quad (2.37a)$$

$$n_y = n_0 - \frac{n_0^3}{2}r_{63}E_z \quad (2.37b)$$

$$n_z = n_e \quad (2.37c)$$

Thus the phase difference between the two rays having the electric field vector along the principal axes is given by,

$$\delta_{xy} = \frac{2\pi}{\lambda} d(n_x - n_y) \quad (2.38)$$

where d is the thickness, and λ the wavelength of the incident light. The voltage required for a phase shift of $\pi/2$ which is equivalent to $\lambda/4$ retardation can be obtained as,

$$V_{\lambda/4} = \frac{\lambda}{4n_0^3r_{63}} \quad (2.39)$$

From the above equation it is evident that the retardation is independent of the thickness of the crystal and is dependent on the wavelength of the incident light. Using the above equation the theoretical value of the voltage required for a $\lambda/4$ retardation at 633 nm, is computed and is equal to 1937 volts. Here r_{63} and n_0 for the KD*P crystal at 633 nm wavelength are taken as $24.1 \times 10^{-12} m/V$ and 1.502 respectively (Yariv 1991).

2.4.3 Circular polarisation analyser

For the longitudinal magnetic field measurement the circular polarisation of the incoming solar light is analysed. The analysis of the circular polarisation is done by employing proper combination of a variable quarter wave plate - KD*P Pockels cell, and a linear

polariser. Here the transmission axis of the linear polariser is aligned 45° to the fast axis of the KD*P crystal. By using Jones calculus, the overall transfer matrix for the above system can be obtained (Yariv 1991). The Jones matrix for a quarter wave plate with 45° azimuth angle is given by,

$$W_{1/4} = \frac{1}{\sqrt{2}} \begin{bmatrix} 1 & -i \\ -i & 1 \end{bmatrix} \quad (2.40)$$

and the right circular polarisation is represented as,

$$V_{rc} = \frac{1}{\sqrt{2}} \begin{bmatrix} 1 \\ i \end{bmatrix} \quad (2.41)$$

Assume that the transmission axis of the linear polariser is aligned parallel to the laboratory x-axis, Then the Jones matrix for the linear polariser is given by,

$$L = \begin{bmatrix} 1 \\ 0 \end{bmatrix} \quad (2.42)$$

Multiplying the above three equations gives,

$$V = \begin{bmatrix} 1 \\ 0 \end{bmatrix} \quad (2.43)$$

which represents a horizontally polarised emerging beam.

In the case of left hand circular polarisation the beam emerging from the circular polariser will be vertically polarised and the resultant intensity after the linear polariser will be zero. If the azimuth of the circular polarizer is switched to -45° , the emerging linear polarisation corresponds to left circular polarisation and for the right circular polarisation the emerging intensity will be zero. Thus by switching the KD*P modulator between $\pm\lambda/4$ voltage the azimuth of the resultant circular polariser can be switched between $\pm 45^\circ$. This allows the selection of the image corresponding to left or right polarisation in the emerging beam. This process is schematically represented in Fig. 2.18.

2.4.4 Quarter-wave retardation, high voltage driver for KD*P electro-optic modulator

In order to operate the KD*P modulator a high voltage power supply was designed and fabricated. This power supply is capable of providing ± 2100 volts (continuously adjustable

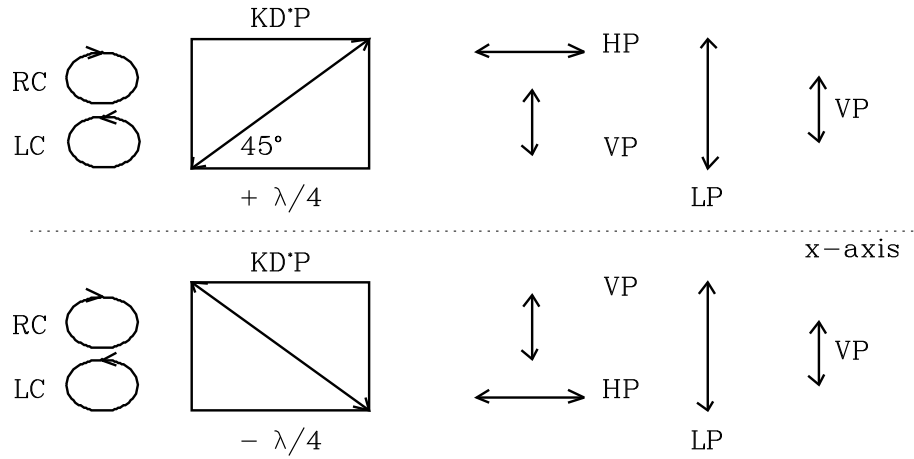


Figure 2.18: *Circular polarisation analyser. The left- or right-circular polarisation (LC or RC) passing through the KD*P crystal is converted into vertical or horizontal polarisation (VP or HP) by applying $\pm\lambda/4$ voltages. The beam emerging after the linear polariser (LP) corresponds to left- or right-circular polarisation for $+\lambda/4$ or $-\lambda/4$ voltages respectively.*

in the range of 0 - ± 2500 volts) output on the application of low voltage signals (TTL pulses) at the inputs. The ripple factor and the rise time of the power supply is measured. The peak to peak ripple and rise time were found to be $\pm 0.25\%$ with 20KHz frequency and 3 msec respectively. To avoid the image acquisition during the rise time, one video field is allowed to pass without capturing, soon after the KD*P switching. The TTL input pulses for the high voltage power supply are derived from the centronics port of the image acquisition computer. These pulses are produced in synchronisation with the image acquisition, such that the alternate captured video frames contains the left or right circular polarisation images. The timing diagram of the KD*P switching and image collection is shown in Fig. 2.19. The vertical blanking pulse contained at the end of the video frame is detected through software and is used to time the centronics TTL pulses. The circuit diagram of the high voltage power supply is included in the appendix A.

2.4.5 Bench test of the KD*P modulator

A bench test of the KD*P modulator was carried out for obtaining the required voltage corresponding to the exact $\lambda/4$ effect. The optical arrangement for the bench test is shown

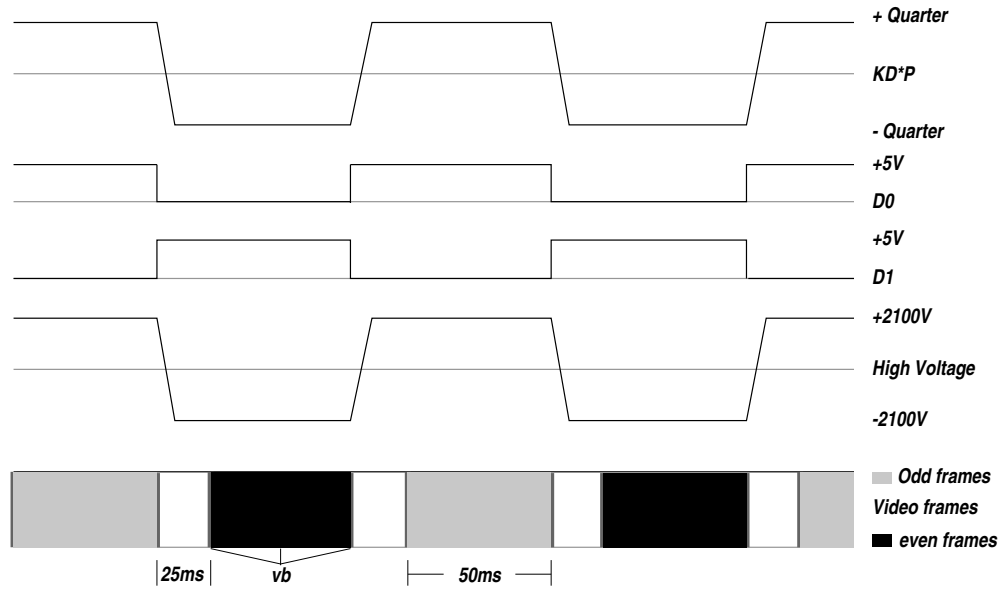


Figure 2.19: Time sequencing diagram showing the synchronisation of image acquisition and KD^*P switching. 'vb' is the vertical blanking pulse after each video field. One video field is skipped after each video frame for the settling of the KD^*P voltage.

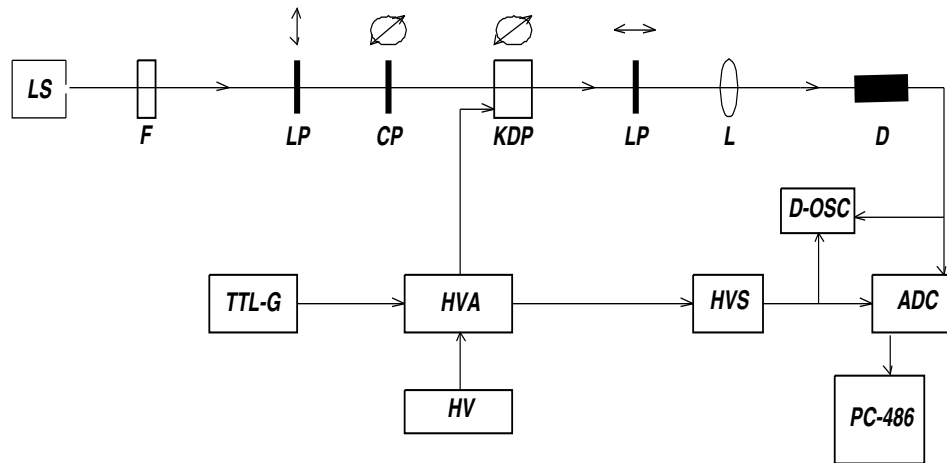


Figure 2.20: The optical arrangement for the KD^*P bench test. LS = light source, F = broad band filter centred around 6122 \AA , LP = linear polariser, CP = circular polariser, KDP = quarter wave plate, L = lens, D = detector, TTL-G = pulse generator, HVA = high voltage amplifier, HV = high voltage power supply, HVS = high voltage sampler, D-OSC = dual oscilloscope, ADC = A/D converter, PC-486 = computer.

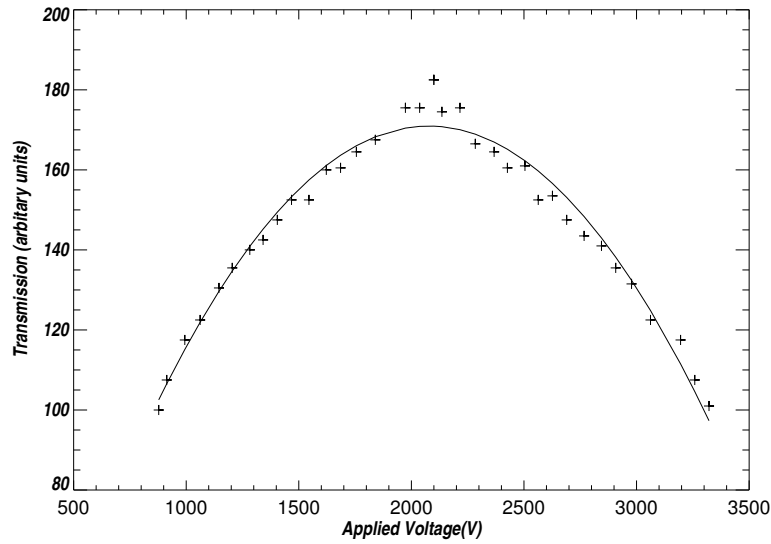


Figure 2.21: *Applied voltage versus retardance, the peak transmission corresponds to the quarter wave voltage.*

in Fig. 2.20. Here F is a broad band filter (10 \AA) with a peak transmission near 6122 \AA and is used to block the remaining parts of the spectrum. An additional fixed $\lambda/4$ plate is added to the KD*P modulator to have a resultant $\lambda/2$ plate so that the crossed linear polarisers transmit maximum intensity if quarter wave voltage is applied to the modulator. The input TTL pulses for the high voltage amplifier is applied from frequency generator. The experiment is conducted for a range of high voltage pulses starting from 0 to $\pm 3000 \text{ V}$, in the intervals of 25 V . The A/D converter digitises the modulated signal obtained from the photodiode detector along with the high voltage sample. This data is used to determine the KD*P voltage required for the $\lambda/4$ effect. The result is plotted as the transmission versus applied voltage and is shown in the Fig. 2.21. From above experiment the quarter wave voltage for the KD*P is found to be 2100 volts at 6122 \AA . Fig. 2.22 shows high voltage sample wave form and the resultant modulated signal, at 7Hz . The exact orientation of the fast axis is also determined by rotating the KD*P between the crossed polarisers. Similar experiment is repeated for more accurate determination of

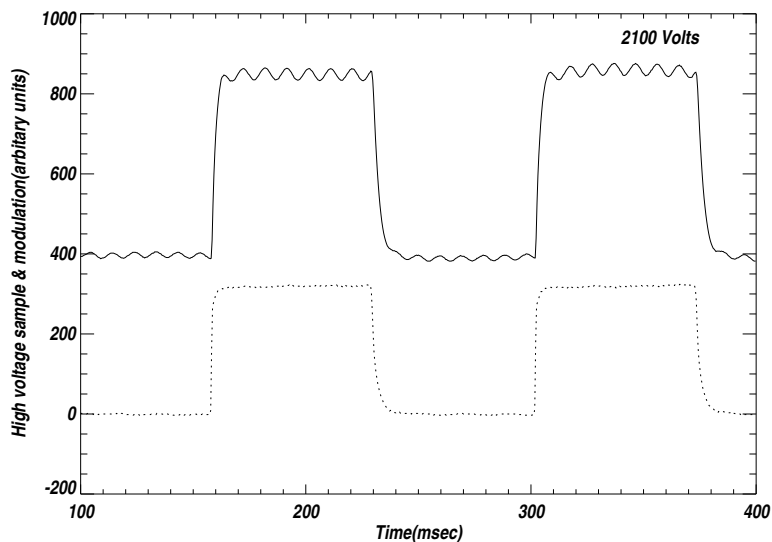


Figure 2.22: KD^*P modulation at 7Hz. The dotted and solid line corresponds to the high voltage sample wave form and modulated signal respectively. The wave pattern on the modulated signal is due to the frequency of the power source used for the collimated light.

the $\lambda/4$ voltage, by placing the modulator in between two crossed polarisers, in front of a spectrograph tuned to 6122 Å wavelength. Fine tuning of the KD^*P modulator is again carried out during the magnetogram observations to have the optimum signal.

2.5 Detector - Cohu 4710 series CCD camera

The detector used in our VMG is a Cohu made monochrome camera which incorporates a Charge Coupled Device (CCD) image sensor chip TC277 from Texas Instruments. This camera provides high resolution pictures with sensitivity as low as 0.25 lux, zero geometric distortion and no lag or retention of images. The CCD used is frame transfer device with $9.2 \times 16.8 \mu m$ pixels arranged in 699×576 array. Here half of the pixel rows are masked for image storage where as the other half are exposed to light. This makes a resultant image area of 6.4×4.8 mm (1/2" vidicon format) on the CCD chip. CCIR scanning system is employed for the image read out, where a single video field (one video frame

Table 2.3: *Specifications of the Cohu 4710 series CCD camera*

Pickup	: single CCD using frame transfer method
Pickup area	: 6.4×4.8 mm
Number of picture cells	: $732(H) \times 576(V)$
Active picture elements	: $699(H) \times 288(V)$
Scanning systems	: CCIR, 2:1 interlaced
Video output	: 1 V p-p, 75Ω unbalanced
Signal-to-Noise ratio	: 56 dB
Power consumption	: 4.2 Watts

contains two video fields -odd and even) takes $1/50$ seconds for scanning. During every video field the charge accumulated in the storage section is read out while image section is exposed. The vertical blanking pulses after each video field (two vertical blanking pulses for each video frame) in the CCIR video out put is detected through software and used for the synchronisation of the KD*P switching and the entire data acquisition and reduction process. The specification of the Cohu CCD is summarised in the table 2.3. In our present optical set-up an area of 3.8×2.9 arc-minute of the solar disk can be imaged by the camera, which gives a resolution of 0.3×0.6 arc-seconds/pixel.

2.6 Image acquisition and processing system

A workstation based on Heurikon HK68 (from Innovision Inc) single board VMEbus computer, integrated with Imaging Technology Series 150 image processing modules makes the complete data acquisition system. The HK68 single board host computer features a Motorola, MC68030, enhanced 32 -bit microprocessor and 68882 floating point co-processor.

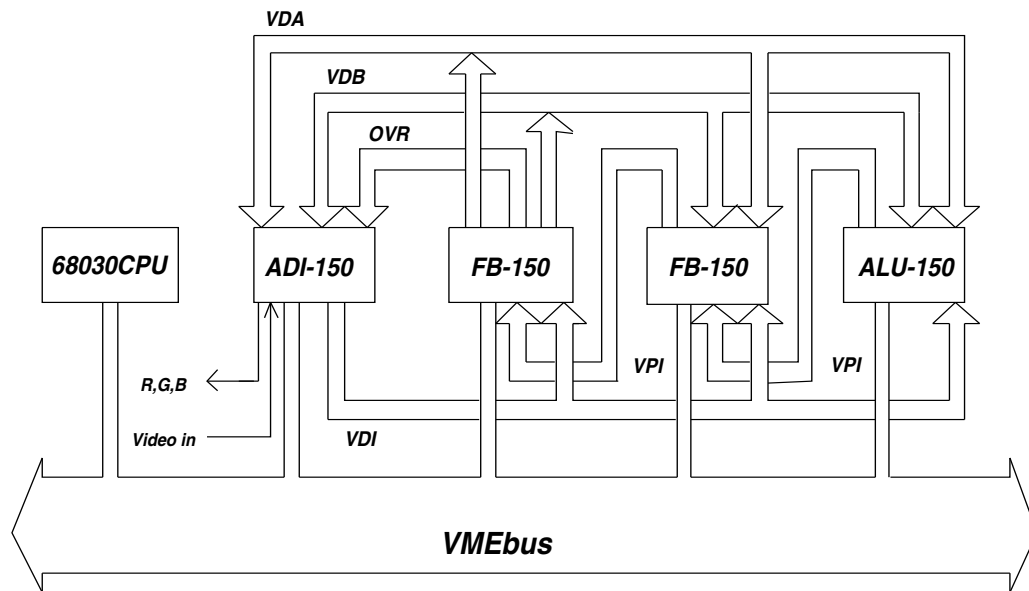


Figure 2.23: *Image acquisition system architecture*

The board contains all the peripheral controllers needed to drive four serial I/O ports, SCSI port and one centronics port. The image processing modules consists of one analogue-to-digital interface (ADI) unit, two frame buffers (FB) and one arithmetic and logic unit (ALU); all connected to the VMEbus of the host computer. All the modules are designed around a video bus which allows fast transfer of image data between the processing modules. The on-board software programmable registers makes image acquisition and processing easier. Fig. 2.23 illustrates the bus architecture of the host computer and the image processing modules. The combination of the host computer, series 150 modules and suitable software can perform complex real time digital image processing tasks such as averaging of images, subtraction etc. The ADI-150 is a high performance analogue-to-digital interface to video source and monitor. The ADI generate timing signal and interrupts for all the other modules and incorporates an 8-bit flash A/D converter with 10MHz sampling rate, which digitises the video input signal to 256 grey levels. Before the

digitisation the video signal is conditioned to remove DC bias and passed through a gain and offset circuitry. The video bus transmit the digitised data to all the other modules (VDI, 8-bit video bus in the figure).The frame buffers FB0 and FB1 contain the image storage required for the real time processing of the data. Each FB-150 consists of a single 512 by 512 by 16-bit frame store (FRAME A) and two 512 by 512 by 8-bit frame stores (B1 and B2). The frame A is used as an accumulator to hold the processed data where the intermediate results exceed eight bits. The video data from the above frame buffers are available on VDA (16-bit, originated from FRAME A) and VDB (8-bit, originated from FRAME B) video buses. ALU-150 is pipelined image processor which provides real time image processing capabilities when used with ADI-150 and FB-150. Within 1/25 of a second the ALU can perform 16-bit multiplication and addition, subtraction or logical operations on an entire frame of pixels. The two 16-bit operands for the arithmetic or logical operations can be selected from the video buses . After the required operation the output results are routed back to the frame store A.

The software used for the operation of video magnetograph is compiled from a C-source code incorporating the ITEX 150/151 library functions and runs under OS/9 operating system. ITEX150/151 functions are subroutines which can be linked to the application programs written in C - language. The ITEX150/151 library functions are used to modify the appropriate on-board registers to prepare the Series 150 modules for different image acquisition tasks. The role of the software may be divided into two parts; setting up the Series150 modules for the image processing and synchronisation/controlling the optical instruments with the image acquisition. Fig. 2.24 shows the flow chart of operations required for a complete acquisition cycle. For making magnetograms the Series150 modules are set up for continuous acquisition and adding up of the images. Here the ALU is programmed for adding the incoming video data on to the pervious image present in the FRAME A ($A \text{ operand} + B \text{ operand} = \text{VDI} + \text{FRAME A} \Rightarrow \text{FRAME A}$). After the ALU operation the result corresponding to the acquired alternate video frame (refer the timing diagram in Fig. 2.19) is routed to FRAME A of FB0 and FB1 separately. This

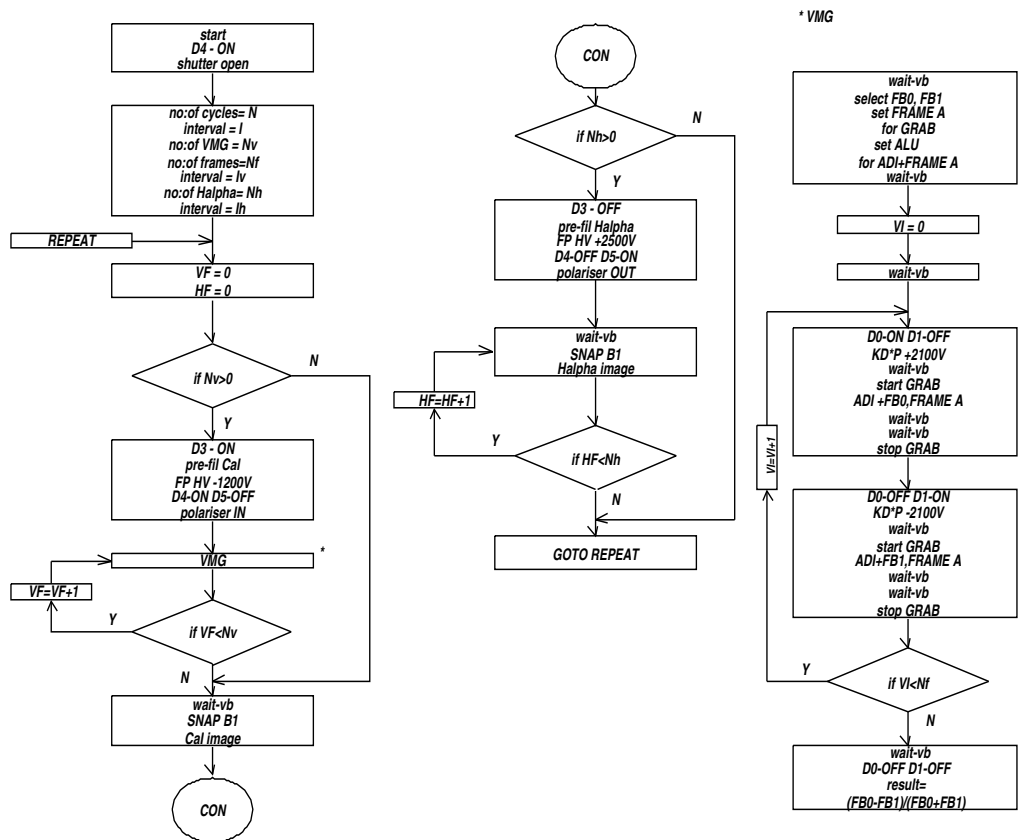


Figure 2.24: Flow chart showing the operation involved in a single cycle of image acquisition.

process is repeated for a maximum up to 256 frames in each frame buffers. The FRAME A contents are then transferred to the host computer memory for further processing. The vertical reset signal (vertical blanking pulse - vb) from the video camera pixel clock is used to synchronise the image acquisition and the polarity switching of the KD*P. This is done in such a way that the alternate incoming video frame contains the image corresponding to left- or right-circular polarisation. The data bits (D0 and D1) of the centronics port is flipped to high/low on the detection of vertical blanking pulse and these signals control the high voltage power supply polarity. For tuning the optics to H α line, D2 , D4 and D5 bits on the centronics port are enabled. D4 and D5 bit is used for changing the high voltage applied to the FP, bringing the appropriate pre-filter and adjusting the relay lens focus whereas D2 is used for removing the polariser from the optical path for improving the image contrast.

2.7 Operational modes of the magnetograph

The operational procedure can be divided into three steps; making of magnetograms, CaI off-band images and H α filtergrams. In normal mode of operation a CaI off band image and an H α image is made soon after each magnetogram. The procedure can be programmed in such a way that any number of magnetograms or H α images can be taken in a single operational cycle. If the interval between any of the above operations is more than 3 min the telescope shutter gets automatically closed to reduce the heat load so that the internal seeing is not affected. The operations such as changing the pre-filter, applying/changing high voltage to the FP etalon, adjusting the focus and applying switching voltage to the KD*P are software controlled through the computer. (*cf.* Fig. 2.24 for the procedure involved in a single cycle of operation).

2.7.1 Magnetogram and CaI filtergrams

For making magnetograms the narrow band filter is tuned at CaI 6122 Å line, 140 mÅ away from the line centre in the violet wing. Tuning the filter to CaI 6122 Å line wing is

accomplished by introducing 6122 Å pre-filter into the beam and applying -1200 V DC to the FP etalon. The linear polariser is introduced into the beam, where the transmission axis of the polariser is kept at 45° to the fast axis of the KD*P crystal. The quarter wave plate (KD*P crystal) converts the circular polarisation into two orthogonal linear polarisation on the application of the quarter-wave voltage. The linear polariser just behind the KD*P lets only one of the beam through at a time. By switching the KD*P between ± 2100 volts, the resultant polarisation can be flipped into opposite sense. The switching of the KD*P is synchronised with the image acquisition. This is done by obtaining a switching signal at the centronics port of the computer on the detection of the vertical-blank pulse in the video signal which is available after each video frame. The switching signal drives a high voltage power supply, the output of which is connected to the KD*P crystal. An image is made for each circular polarisation ie $(I + V)$ and $(I - V)$ and stored in two separate 16-bit frame buffers. To increase the signal to noise ratio a sufficiently large number of images (sa mximum of 256) are added for each circular polarisation in to the respective frame buffers alternately. The resultant magnetogram is obtained by subtracting and normalising the added images, ie,

$$\frac{V}{I} = \frac{\Sigma \frac{1}{2}(I + V) - \Sigma \frac{1}{2}(I - V)}{\Sigma \frac{1}{2}(I + V) + \Sigma \frac{1}{2}(I - V)} \quad (2.45)$$

The image is then transferred to the host computer hard disk. In another mode of operation instead of storing $(I + V)$ and $(I - V)$ seperately, the left- and right-circular polarization video frames are added and subtracted alternately in a single frame buffer.

The result is given by,

$$nV = \Sigma \frac{1}{2}(I + V) - \Sigma \frac{1}{2}(I - V) \quad (2.46)$$

where n is the number of pairs of video frames utilised for making the magnetogram. The above resultant image is then transferred to the host memory. This method has the advantage that it uses a single frame buffer and thus saving switching time between the frame buffers. More over, during calibration this method is more suitable than the fractional Stokes V/I measurement. So the second method is preferred for the normal mode

of magnetograph operation. In our system, the whole process of making a magnetogram by averaging 128 frames in each circular polarisation and transferring the image to the host computer takes around 30 seconds. A CaI 6122 Å off-band image is made after each magnetogram keeping the filter tuned at the same wavelength. This off-band image gives information about the photospheric structures coinciding with the magnetogram signal.

2.7.2 Chromospheric H α filtergrams

For obtaining H α filtergrams the 6563 Å pre-filter is introduced into the solar beam in the place of the 6122 Å pre-filter. A voltage of +2500V is applied to the FP etalon for bringing its passband to the H α line center. Any difference in focus is adjusted by moving the relay lens to the pre-fixed H α point. The polarizer is also rotated away from the optical path to have a better image contrast. The image is acquired into the 8-bit image frame and transferred in to the computer memory.

This procedure gives near-simultaneous observations of small-field, high resolution magnetic field and corresponding photospheric and chromospheric structures which is an important requirement of active region evolution study.

Chapter 3

Calibration, comparison and data reduction of USO video magnetograms

Since the video magnetograph essentially obtains Stokes circular polarisation, V and not the magnetic field values, therefore it is required to convert V into B_{\parallel} . A procedure has been developed for the calibration of USO video magnetograms, to convert the measured Stokes circular polarisation value V in to magnetic field values. We use the line profile slope method for the absolute calibration of the magnetograms. In order to check the accuracy and reliability of the USO magnetograms, it is important to compare them with magnetograms obtained from other sources. However due to the large time gap between USO and other ground-based observatories the comparison is usually difficult as the evolution process on the sun may itself introduce important changes. For example there is a time gap of 12 hours between USO and BBSO (Big Bear Solar Observatory) observations, during which large structural changes in the active region magnetic field can take place. This would make any comparison of the respective magnetograms meaningless and inappropriate.

For a appropriate comparison, the only available data at our location are full-disk magnetograms obtained from GONG (Global Oscillation Network Group) instrument operational at USO. Since the spatial resolution of the GONG full-disk magnetogram (6

arc-seconds) is considerably lower than that of USO, we could use only those for the comparison of gross magnetic features. The initial comparisons showed a promising result. For a detailed comparison we obtained calibrated magnetograms made by the space-borne SOHO/MDI (Solar Orbiting Heliospheric Observatory/Michelson Doppler Imager) instrument taken around the time of USO magnetograms. SOHO/MDI full-disk magnetograms have a moderate spatial resolution of 2×2 arc-seconds. We found that nearly all the magnetic features on the SOHO/MDI and USO magnetograms were in very good agreement. After the calibration of USO magnetogram, a correlation plot is obtained between USO and SOHO magnetic field values. The details about the calibration, comparison of USO video magnetograms are described in the following sections. Preliminary data reduction of USO magnetogram is also described towards the end of the this chapter.

3.1 Calibration of USO video magnetograms

The longitudinal magnetograph measures the circular polarisation of the solar light. For a quantitative analysis of the magnetograms, accurate conversion of the polarisation images into solar magnetic field is required. Several methods for converting polarisation measurements into magnetic field have been discussed in the literature (Hagyard *et al.* 1988; Jefferies & Mickey 1991; Cauzzi *et al.* 1993). These methods vary depending upon the type of instrument used for the measurements. For example the BBSO longitudinal magnetograph is calibrated using three methods (Varsik 1995): by using the differences in radial velocity of the sun caused due to the differential rotation, by measuring the line profile in the Zeeman-sensitive 6103Å line and by comparison with spectra taken in 5250 Å line. All these calibration methods were found to be reasonably consistent with each other. Cauzzi *et al.* (1993) also discusses different methods for the calibration of longitudinal magnetograms, including the profile line slope method, which has been used for the absolute calibration of the USO magnetograms. Using this method a calibration constant is derived for the instrument taking into account of all the constants and atomic parameters of the absorption line. The details of the profile line slope is discussed in the

next section.

3.1.1 Profile line slope method in weak field approximation

For the calibration of USO magnetograms we have used the profile line slope method, taking the advantage of fast tunability of our FP etalon filter. This method has been extensively used for the calibration of BBSO video magnetograms (Varsik 1995). The method is based on weak field approximation, where the assumption is that the Zeeman splitting $\delta\lambda_B$ is much smaller than the Doppler width of the line $\delta\lambda_D$. In this approximation the transfer equation for the Stokes parameters is simplified greatly (Stix 1991; Cauzzi *et al.* 1993), and the Stokes parameter V can be expressed as,

$$V = -\mu \lambda_0^2 g B_{\parallel} \frac{dI}{d\lambda} \quad (3.1)$$

where $\mu = e / 4 \pi m c^2$; e and m are the charge and mass of the electron, λ_0 the central wavelength of observation, g the Landé factor of transition for the absorption line, B_{\parallel} the longitudinal magnetic field and I the Stokes intensity obtained in the absence of magnetic field. The profile line slope $dI/d\lambda$ can be easily measured in the case of filter magnetographs. This can be done by tuning the filter at different wavelength offsets from the line centre. In weak field approximation, the slope of the line profile is assumed to be a constant independent of the Zeeman splitting. Thus by finding $dI/d\lambda$, B_{\parallel} can be directly estimated from V measurements. The validity of this method can be extended up to $B \sim 3500/g$ Gauss provided that we observe far enough in the line wings i.e., $\sim 3\lambda_D$ away from the line centre where λ_D is the Doppler width (Jefferies & Mickey 1991).

3.1.2 Calibration of the USO video magnetogram data

From equation (3.1) it is evident that by estimating the line profile slope $dI/d\lambda$, one can derive B_{\parallel} from V measurements. We have used two methods for the estimation of the line slope. In the first method, the narrow band filter is tuned at different known wavelength offsets from the line centre and an image is acquired for each wavelength offset. The fast tunability of the FP etalon filter makes it possible to obtain the images rapidly along

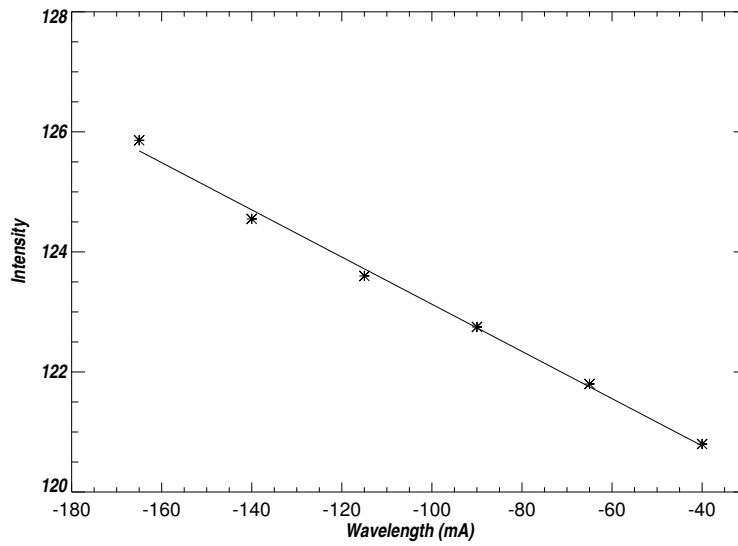


Figure 3.1: *The slope of the line profile. Intensity for different filter position is plotted against the wavelength offset, the slope is estimated as $0.04/\text{m}\text{\AA}$.*

the line profile. This reduces possible errors introduced due the atmospheric changes or solar variations. The measurement is carried out for a range of wavelengths, starting from $-40 \text{ m}\text{\AA}$ to $-170 \text{ m}\text{\AA}$ from the line centre, in steps of $25 \text{ m}\text{\AA}$. The filter position for the normal magnetogram observations, i. e., $-140 \text{ m}\text{\AA}$, lies within the above measurement range. The intensity for each image is estimated by averaging the pixel values of a section of the image which does not contain any active regions. Fig. 3.1 shows the averaged quiet sun intensity against the wavelength offset. The line slope $dI/d\lambda$ is calculated from the intensity measurements and is found to be $0.04/\text{m}\text{\AA}$.

In the second method, the resultant intensity is derived by the convolution of the filter and line profile at various points along the line profile. The result obtained is plotted in Fig. 3.2 as the intensity versus wavelength offsets. The line slope derived from this method; i.e., $0.047/\text{m}\text{\AA}$, is slightly higher than that obtained from the image measurements. When used with the real data for calibration and comparison the value obtained by the second method is found to be more accurate.

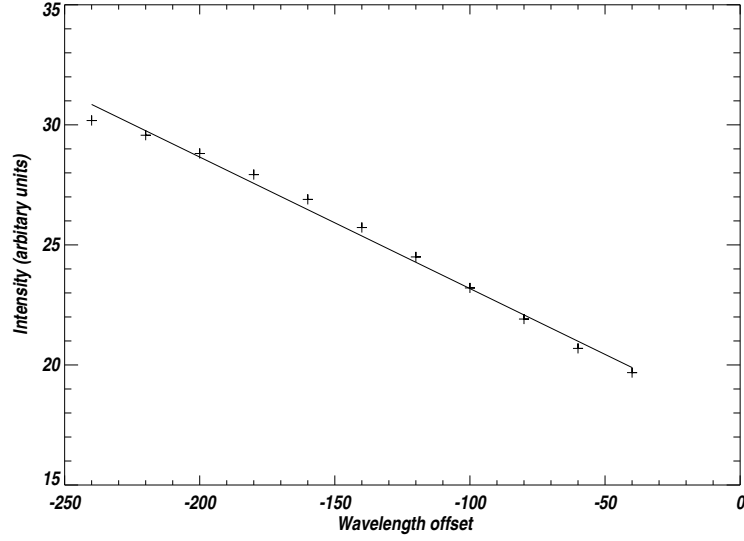


Figure 3.2: *The slope of the line profile by filter and line profile convolution. Intensity for different filter position is plotted against the wavelength offset, the slope is estimated as $0.047/\text{m}\text{\AA}$.*

For the computation of calibration constant equation (3.1) is used along with the other atomic parameters related to the absorption line. The equation can be rewritten as,

$$B_{\parallel} = k_{cal} V = k_{cal} (I_{+} - I_{-}) \quad (3.2)$$

where

$$k_{cal} = \left(-\frac{dI}{d\lambda} \mu \lambda_0^2 g\right)^{-1} \quad (3.3)$$

and V is the intensity obtained by subtracting a pair of video frames taken in opposite circular polarisations. Substituting the value $dI/d\lambda$, k_{cal} is estimated to be 2059. Thus the Stokes V image made by using n pairs of video frames is converted into longitudinal magnetic field image using the equation,

$$B_{\parallel} = \frac{k_{cal}}{n} V \quad (3.4)$$

In USO video magnetograph the resultant magnetogram can be stored in $512 \times 512 \times 8$ -bits or $512 \times 512 \times 16$ -bits format. Due to large memory requirement for 16-bits format, in normal mode of operation the images are stored in 8-bits format. Here the 16-bits result of the subtraction of $(I + V)$ and $(I - V)$ images are converted in to 8-bits by stretching the maximum and minimum intensity values between 0 and 255 grey levels. The 16-bits maximum and minimum values are recorded along with the image and are used during the calibration process to restore the original values of the grey levels. A factor of 16 is included in the calibration equation so that the precision is not lost during the conversion from 16 to 8 bits. In the case 16-bits format, Stokes V values are directly converted into longitudinal magnetic field values using the equation (3.4). After calibration of the magnetograms the minimum detectable field was found to be 15 Gauss. During best seeing conditions the fine magnetic features of 2 - 4 arc-second could be observed. The initial data reduction methodology is described in detail at the end of this chapter.

3.2 Comparison of USO, SOHO/MDI and GONG magnetograms

For comparison, we have used an USO VMG taken on 09 April 1997/ 09:32 UT and the magnetograms of SOHO/MDI and GONG instruments obtained on the same day at 09:42 and 09:01 UT respectively. GONG instrument obtains one full-disk magnetogram in every hour. On the other hand SOHO obtains both full-disk and high resolution magnetograms for target region. The full-disk magnetograms obtained by SOHO/MDI and GONG instruments have spatial resolution of $\sim 2 \times 2$ and $\sim 6 \times 6$ arc-seconds per pixel, respectively where as the USO magnetogram has a much better pixel resolution of 0.3×0.6 arc-seconds. Consequently we use the GONG magnetogram only for comparison of the gross magnetic features, while the moderate resolution SOHO/MDI magnetogram is used for a detailed analysis. The SOHO/MDI magnetogram enjoys the advantage of space-borne measurements which is free from atmospheric seeing effects. This makes the SOHO/MDI full-disk magnetograms with coarser resolution of $\sim 2 \times 2$ arc-seconds comparable with ground

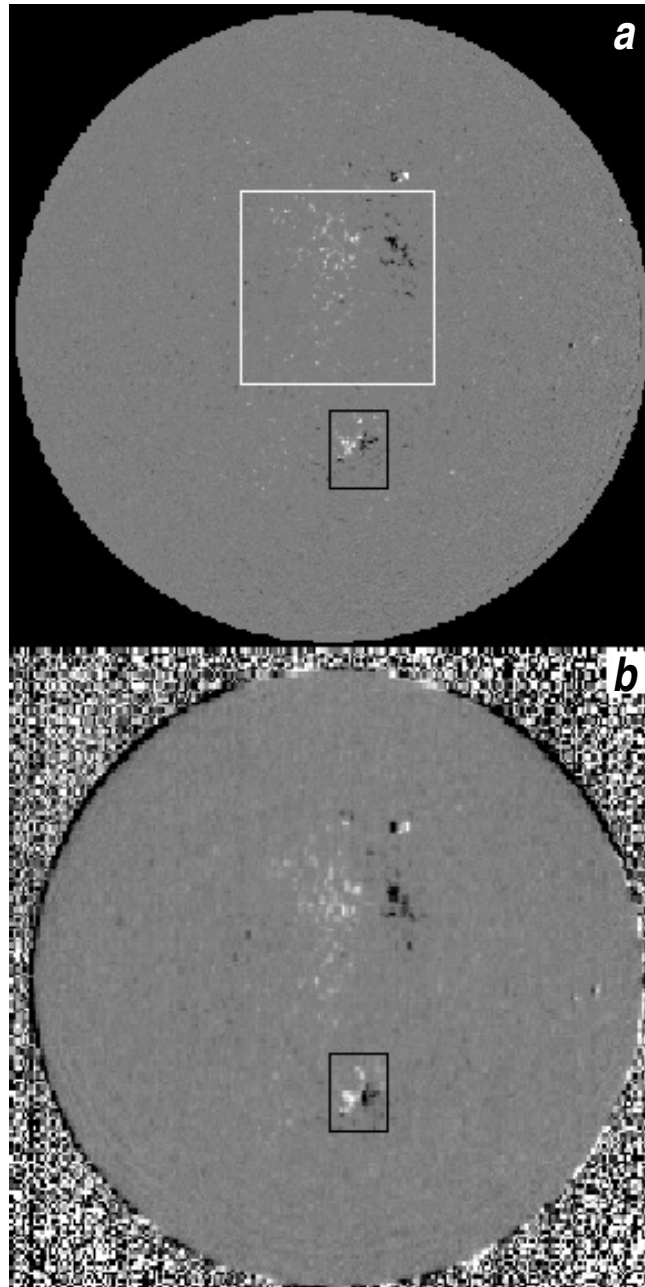


Figure 3.3: *The magnetograms used for comparison. (a) SOHO magnetogram obtained on April 9, 1997 at 09:42 UT, (b) GONG magnetogram obtained on the same day at 09:01 UT. The area enclosed by the black box is equivalent to the field-of-view of USO magnetogram. In the figure North is up and West is right.*

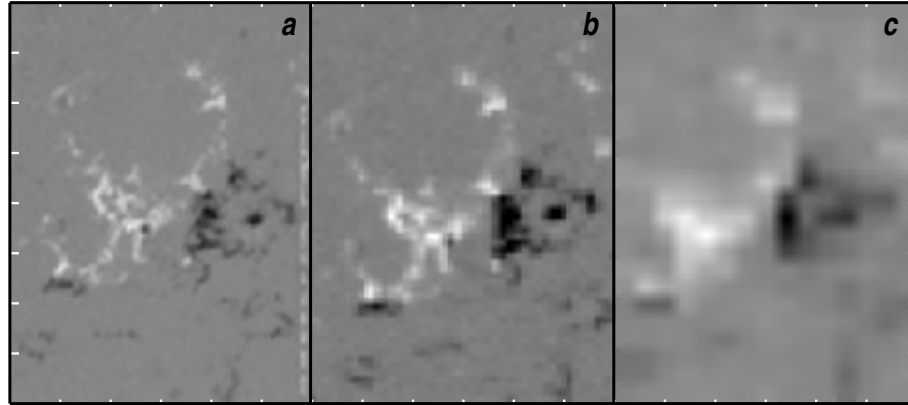


Figure 3.4: *Resolution effect.* The magnetograms obtained from SOHO (b) and GONG (c) instruments are shown along with USO (a) magnetogram. The SOHO and GONG magnetograms are a part of full disk magnetograms obtained with 2×2 and 6×6 arc-second spatial resolution. Here North is up, West is right and each tick mark corresponds to 30 arc-seconds on the sun.

based observations, normally limited due to atmospheric seeing effects to a spatial resolution of < 2 arc-second during the period of observation. Fig. 3.3(a) and (b) show full-disk magnetograms obtained from SOHO/MDI and GONG instruments respectively. The marked regions by black box on the image correspond to a field-of-view (FOV) of $\sim 4 \times 3$ arc-seconds, equivalent to the FOV of USO magnetograph. This area of the SOHO/MDI image was enlarged by binning to the size of USO magnetogram. The image rotation of the USO magnetogram produced by the Coudé movement of the telescope is corrected using IDL (Interactive Data Language) software package. The magnification of USO and GONG magnetograms were adjusted to match the SOHO magnetogram. Fig. 3.4(a), (b) and (c) show the SOHO/MDI, USO and GONG magnetograms corresponding to the same area on the sun around NOAA 8027. As evident, nearly all features on the SOHO/MDI and USO magnetograms are found to match well, where as only the gross magnetic features of the coarse GONG magnetogram can be identified on USO and SOHO magnetograms. The SOHO magnetograms used for comparison are calibrated only for

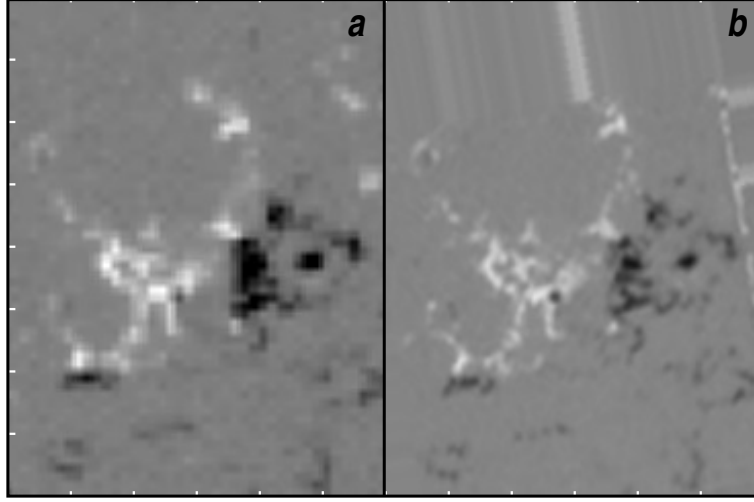


Figure 3.5: The SOHO (a) and USO (b) magnetograms. USO magnetogram is corrected for the Coudé telescope image rotation and for comparison only undistorted image section is used.

weaker fields up to ± 250 Gauss whereas the USO magnetogram is calibrated up to a field strength of ± 1500 Gauss using the linear portion of the line profile (Scherrer *et al.* 1995). This gives a higher contrast to the SOHO/MDI magnetogram over USO magnetogram due to the saturation in SOHO magnetogram for a field beyond ± 250 Gauss.

3.2.1 Correlation plot of calibrated USO and SOHO magnetograms

In order to quantify the comparison, we made a scatter plot between USO and SOHO magnetograms taken around the same time. Before making the correlation plot, we identified the FOV of the USO magnetogram on the SOHO/MDI full-disk magnetogram, which was selected and detached from the image. This FOV was magnified to the same size as the USO magnetogram for a proper comparison and a detailed view of fine structures. The USO magnetogram is normalised for the background intensity and corrected for the image rotation caused due to the Coudé motion of the telescope. The images after the above processing, are shown in the Fig. 3.5. A smoothening of the USO image has been carried out by taking a box averaging over 6×3 pixels to have almost the same spatial

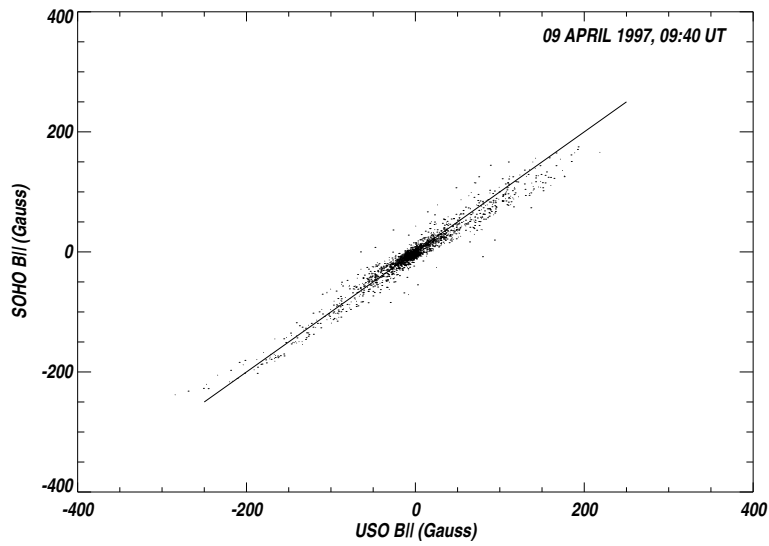


Figure 3.6: Scatter plot made between USO longitudinal magnetic field and SOHO longitudinal magnetic field. The magnetograms were obtained on 09 April 97, around 09:40 UT.

resolution as that of SOHO/MDI magnetogram. Fig. 3.6 shows a scatter plot of USO and SOHO/MDI magnetic fields. The large scatter at the larger field values in the plot is due to the fact that the SOHO/MDI magnetograms are saturated beyond ± 250 Gauss whereas the USO magnetograms are calibrated for ± 1500 Gauss. The slope of the best fit line drawn through the scatter plot is found to be $\sim 45^\circ$, which indicates the accuracy and reliability of the calibration procedure adopted for USO magnetograms.

3.3 Data acquisition and reduction methodology

3.3.1 Format of the raw VMG data and initial processing

For off-line correction and analysis of the images, a software is developed in IDL(Interactive Data Language), which performs various required operations on the image such as normalization of background intensity, correction for image rotation, noise reduction and the calibration. During calibration, the original intensity values are restored using a destretching routine, which is a part of the above program. The rotation of the image, caused due

to the Coudé motion of the telescope is corrected by calculating the offset angle using the time information, stored along with the image file. Normalization of the image is done by detecting the background intensity using histogram method, assuming that the maximum number of pixels corresponds to the back ground intensity. The FFT (Fast Fourier Transform) routine available in IDL software is used for the removal of random noise. A low pass filter is designed to filter out the high frequency noise component from the image. The frequency response of the filter is multiplied with the Fourier transform of the image and an inverse transform is applied to get back the filtered data. The filter is designed such that, it avoids the spatial frequencies of $> 40\text{Hz}$. Since the image is acquired with a rectangular CCD and is stored in square format, an aspect ratio correction is also applied. For correction the y-size of the image is multiplied by the width to height (4.8mm / 6.4mm) ratio of the CCD. The resultant data after aspect ratio correction consists of 512×384 pixels. Finally, we use equation (3.4) for the calibration of the processed data.

3.3.2 Magnetic flux, gradient and potential field calculation

A software routine is developed in IDL for the calculation of magnetic flux, gradient and potential field using the USO's line-of-sight magnetograms. The magnetic flux is calculated by integrating magnetic field over the active region, i. e., magnetic flux ϕ is given by

$$\phi = \int_S B \cdot da \quad (4.1)$$

where da is elementary area and B is the average line-of-sight magnetic field value enclosed by the area da . From the calculation of magnetic flux, it is possible to understand the flux changes and associated activities.

From the measurement of the longitudinal magnetic field in the photosphere one can compute the theoretical three dimensional map of the magnetic field. We use Schmidt method for the computation of the three dimensional magnetic field map (Harvey 1966). In this method monopole formulation of the potential theory is used to evaluate the magnetograms (Schmidt 1964). For the calculation of the field components B_x, B_y and B_z the

following equation is used,

$$B_i(r) = \frac{1}{2\pi} \int_S \frac{B_n(r')(r-r')_i}{|r-r'|} da' \quad (4.2)$$

where i represents x , y or z , r and r' are measured from some origin to the point where B is evaluated. The potential field map represents the minimum energy configuration of the magnetic field system. Any deviation from this produces a different configuration of the magnetic field, which is normally in a higher energy state and is called force-free field configuration (Lust & Schluter 1954; Stix 1991). The force-free field configuration can store energy in excess of minimum potential field energy belonging to the same photospheric boundary conditions. Since the observed magnetic structures or the direction of transverse magnetic field component represents the real configuration of the magnetic field in the solar atmosphere, the deviation of this from the computed potential field gives a measure of the energy stored in the magnetic field. For example, a comparison of the calculated potential field with the chromospheric $H\alpha$ fibril structures which trace the magnetic field lines, can give a qualitative information on the excess of energy stored in the field configuration. The magnetic field gradient can also be calculated from B_x and B_y components of potential field. This is done by taking the derivative of these components along x and y directions, and the resultant gives the magnetic field gradient.

Chapter 4

Observations and Analysis of Magnetic Fields in Solar Active regions

For the study of flare related magnetic field changes, we have carried out a detailed analysis of the H α and magnetic field structural evolution of active regions NOAA 7843, NOAA 8032, and NOAA 8038, observed during February 18 - 20, 1995, April 15, 1997, and May 10 - 13, 1997 respectively. These active regions were observed at the period of the activity minimum period of the sun, i.e., around September 1996. The region NOAA 7843, observed during February 18 - 20, 1995 was a moderately active group. It produced only sub-flares and all of these flares occurred near the site of emerging flux regions (EFRs). Large number of EFRs were observed during its three days of evolution. The flares were larger and more frequent when the EFRs emerged close to the existing spots. Some of the EFRs were accompanied by repeated sub-flares and surging activity. The active region, NOAA 8032 of April 15, 1997 was an example of a rapidly emerging and evolving flux region. Within the short duration of just a few hours, several EFRs were observed, and surges and small flares ensued. As in the case of NOAA 7843, in this region also EFRs emerged very close to the existing spots of opposite polarity and were associated with surging activity. During the observations of the active region of May 10 - 13, 1997 an M class two-ribbon flare was observed on May 12, otherwise the region was quiet during May

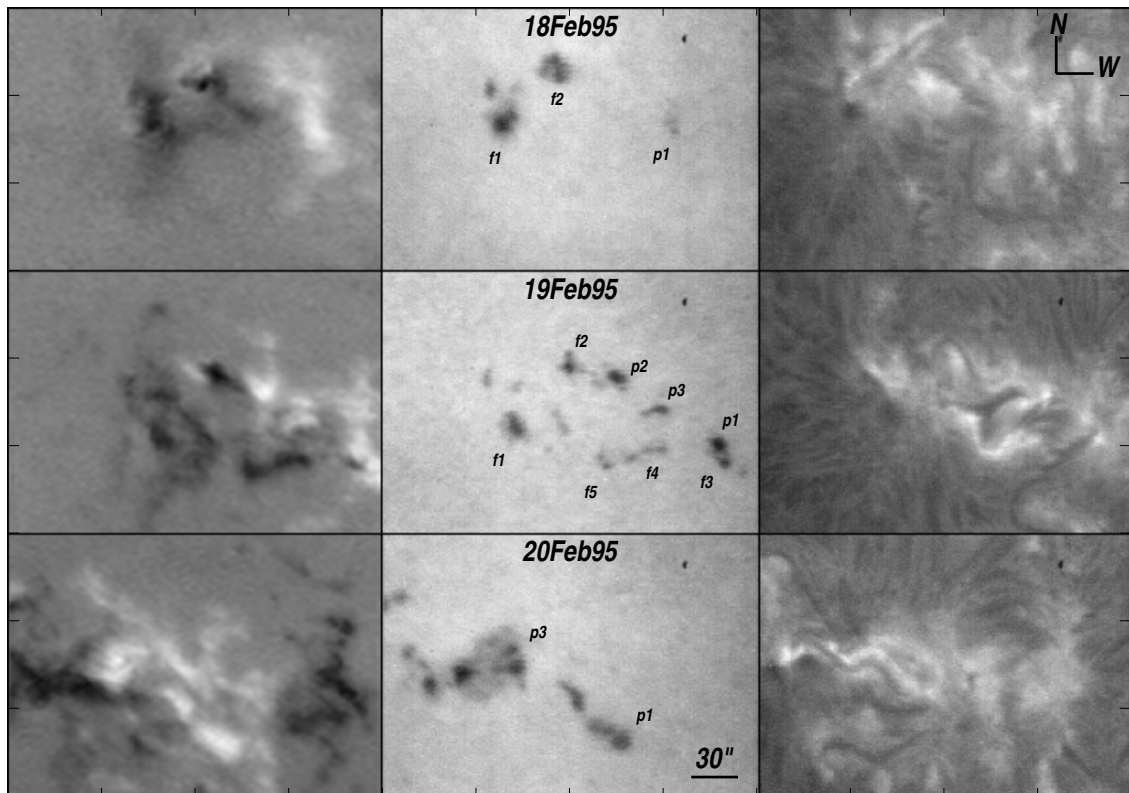


Figure 4.1: *Magnetograms, CaI and H α images of the active region NOAA 7843, observed during February 18-20, 1995.*

10 and 11, and did not show up much activity or evolutionary changes. Flux emergence and cancellation was observed prior to this flare. In the following sections, we present details of the photospheric, chromospheric and magnetic field observations taken using the USO video magnetograph.

4.1 Active region NOAA 7843 observed during February 18-20, 1995

4.1.1 Observations

The active region NOAA 7843 appeared on February 16, 1995 at the location of S14E62. The first USO observations of this active region started on February 18, 1995. During its

three days of evolution in the period February 18 - 20, it showed a lot of changes, produced a number of sub-flares and surges. Solar Geophysical Data (March 1995, Number 607, Part1) reported around 11 X-ray C-class flares and a large number B-class flares during the above three days of evolution. Near-simultaneous observations of longitudinal magnetic field, $H\alpha$, and CaI photospheric images were obtained for this region using the video magnetograph instrument. Fig. 4.1 show the evolution of active region during February 18 - 20, 1995 as observed in VMG, CaI, and $H\alpha$ modes respectively. On February 18, 1995, only three main sunspots $p1$, $f1$ and $f2$ were seen in CaI filtergrams. Corresponding VMGs and $H\alpha$ also showed simple field structure. The emergence of new fluxes was evident from magnetograms and $H\alpha$ pictures and by February 19, 1995 a large number of new flux regions appeared. Almost continuous flaring activity was also observed very close to some of these emerging flux regions. Eruption and reformation of filaments, which marked magnetic neutral line were observed during this period. Changes in the $H\alpha$ fibril structures showed re-arrangement of the field lines due to emergence of new fluxes. On February 20, 1995, sunspot $p3$ developed into δ configuration with a high magnetic field gradient. The new flux emergence of associated with this δ spot might have triggered the 1N/C2.5 flare reported on February 20, 1995 at 02 UT.

4.1.2 Discussions and Results

Flux emergence and the morphological changes in the active region

The study of the morphological changes of an active region provides a good account of the process of energy storage and flare productivity. General relationship between the flare occurrence and the evolutionary changes of the sunspot group was studied by Tanaka (1975), while relation between emergence of new flux and flare occurrence was found by Rust (1973), and Martin *et al.*(1984). From the study of active regions Zirin & Liggett (1987) reported a great flare near a highly sheared neutral line filament. Direct evidence of shear development due to the emergence of new fluxes can be obtained by photospheric vector magnetic field measurements (Hagyard *et al.* 1984), however $H\alpha$ filaments and

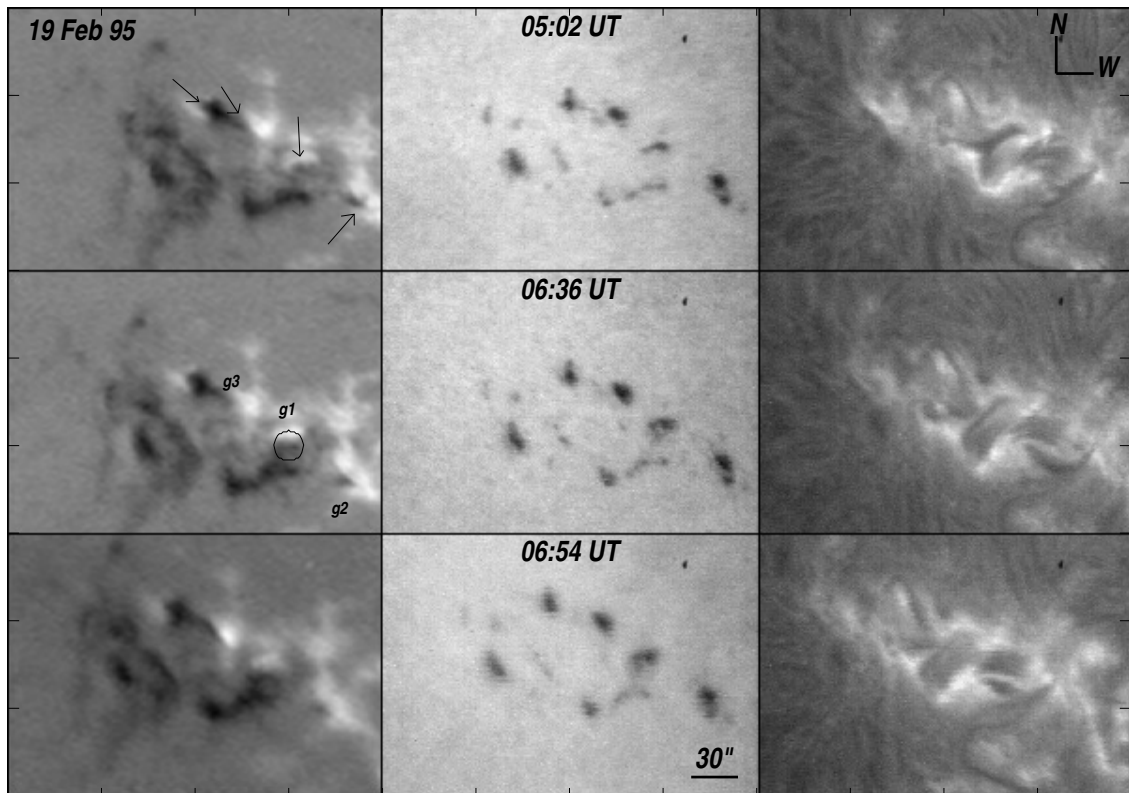


Figure 4.2: Magnetograms, CaI and H α images of the active region NOAA 7843, observed on February 19, 1995. The arrows show the locations of high magnetic field gradient, and the circled area show an increase in gradient during 05:02-06:36 UT

fibril structures can also provide a qualitative idea of shear development in active regions.

The evolutionary characteristics of the active region NOAA 7843, from the observations of white light pictures, magnetograms and H α filtergrams revealed newly emerging flux regions. In H α images the emerging flux regions appeared as bright points. Fig. 4.2 shows a sequence of magnetograms, white light and H α images, of the region taken on February 19, 1995. A comparison of white light images of February 18 and 19 (Fig. 4.1 and 4.2) showed a large number of new emerging flux regions (EFRs) which appeared in the form of sunspots. Most of the spots appeared very close to the existing magnetic field structure i.e., with in 10 - 20 arc-seconds. Negative polarity sunspots $f1$ and $f2$ were

split or decayed into smaller sunspots, while new spots, $p2$, $p3$, $f3$, $f4$ and $f5$ appeared on February 19, 1995. A steep increase in magnetic field gradient was observed during 05:02 - 06:36 UT at the encircled location. This increase in gradient resulted due to the emergence of new flux region at that location. The $H\alpha$ images showed bright points corresponding to the EFRs. Loop structures running along the neutral lines were also noticed in the $H\alpha$ images. The sequence of the $H\alpha$ filtergram show a rearrangement of loop structures due to the emergence new magnetic fluxes (*cf.* Fig. 4.2). On February 20, 1995, a δ spot configuration developed at $p3$, producing strong magnetic field gradient at that location. Some previous sunspots decayed while some new sunspots appeared in this region. A number of C-class flares were reported on February 19 and 20, 1995 (SGD, March, 1995, Number 607, Part 1). These flares might have resulted due to the continuous emergence and cancellation of flux regions.

Magnetic field gradient development and flux cancellation

Another important factor which plays a role in flare productivity of an active region is the proximity of emergence of new flux region to the existing ones (Rust 1972). Close emergence of new fluxes, characterized by large magnetic field gradient, may build up energy in the magnetic field configuration and can drive flux cancellation. If adequate free energy is available in the active region magnetic field, flux cancellation may trigger solar flares. The relation between the presence of strong gradient and occurrence of flares was reported earlier in literature by Rust (1973) and Severny (1969). Emerging flux region driven flux cancellation and their relation to flares were reported by Wang & Shi (1993).

We observed strong magnetic field gradient at several locations in the active region NOAA 7843, marked in the magnetograms obtained on February 19, 1995. Comparison of magnetograms taken around 05:00 UT and 06:30 UT showed that the magnetic field gradient increased at the location marked as $g1$ (Fig. 4.2). The $H\alpha$ brightening coincide with this high magnetic field gradient region. There is another such region of high magnetic field gradient, marked with $g2$, where a negative polarity region emerged very close to the

existing opposite polarity region. The field configuration showed a large structural change and a δ configuration developed at the region $g2$ on February 20, 1995.

Comparison of calculated potential field, $H\alpha$ neutral line filament, and fibril structures

The transverse component of the potential field was calculated, using the observed photospheric longitudinal magnetic field, as the boundary condition. The potential field configuration gives the minimum energy state in an active region. In the chromosphere, the magnetic field lines are traced by fibril structures and opposite polarity regions are separated by $H\alpha$ neutral line filaments. This represents the actual magnetic field configuration as observed in the chromosphere. If the field structure from the photosphere to chromosphere has not undergone major changes, and the $H\alpha$ fibril structures largely follow the calculated transverse potential field and neutral line filaments run perpendicular to the calculated transverse potential field component we may consider the active region to be in minimum energy state. Any deviation from this potential field configuration would indicate free energy build up in the active region. Although USO VMG measures only the photospheric magnetic field, we could undertake a comparison of the computed potential field with the chromospheric $H\alpha$ fibril and filament structures. This comparison would give a qualitative idea about the energy build up in an active region. Several observations relating the deviation of the observed transverse field and potential field to flare production has been reported in the literature (Hagyard *et al.* 1984; Ambastha *et al.* 1993). Similar kind of studies have been carried out using $H\alpha$ fibril structures as the tracers of magnetic field, which reported occurrence of flares at locations where the fibril structures run almost parallel to the magnetic neutral line, representing a large deviation from the potential field structure.

Fig. 4.3 - 4.5 show the computed potential field overlaid on the continuum and $H\alpha$ images of 19 and 20 February. The longitudinal magnetic field contours are also shown with white light images. Although the finer fibril structures are not easily visible in the $H\alpha$ images, the filaments separating the opposite polarity regions are easily distinguishable.

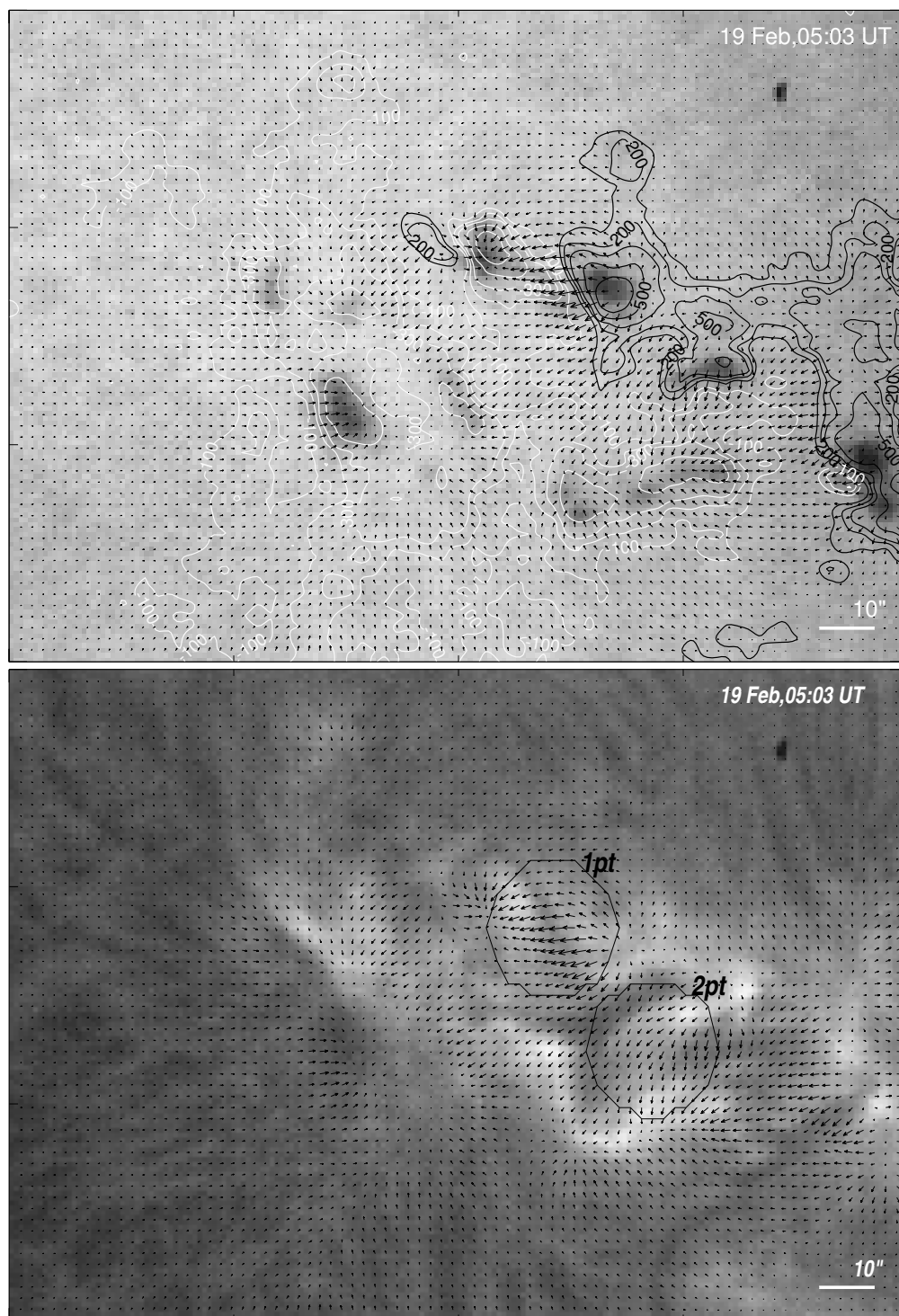


Figure 4.3: The computed potential field over laid on CaI (a) and H α (b) images of the of the active region NOAA 7843, observed on 19 Feb 1995, 05:03 UT

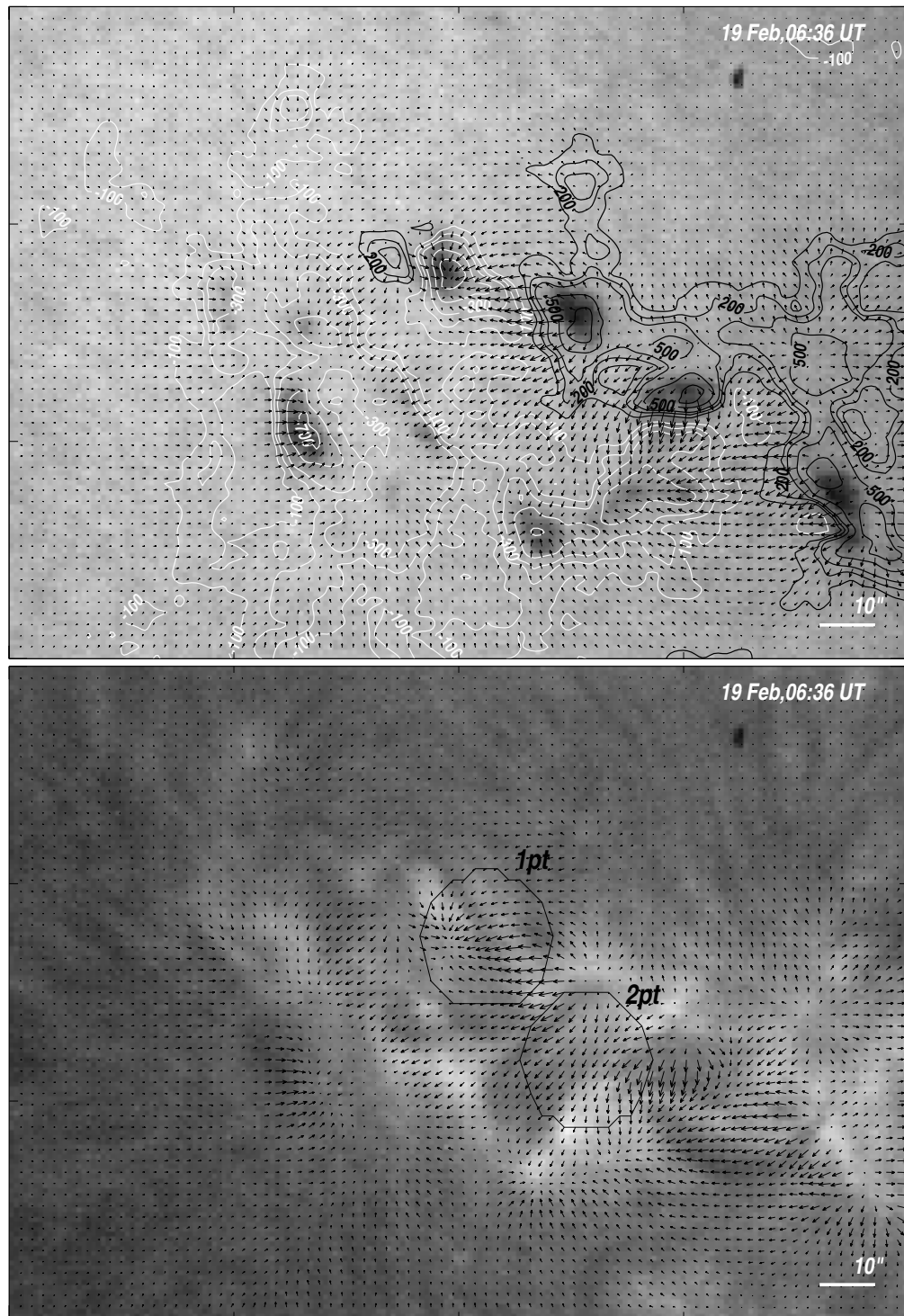


Figure 4.4: The computed potential field over laid on CaI (a) and H α (b) images of the of the active region NOAA 7843, observed on 19 Feb 1995, 06:54 UT

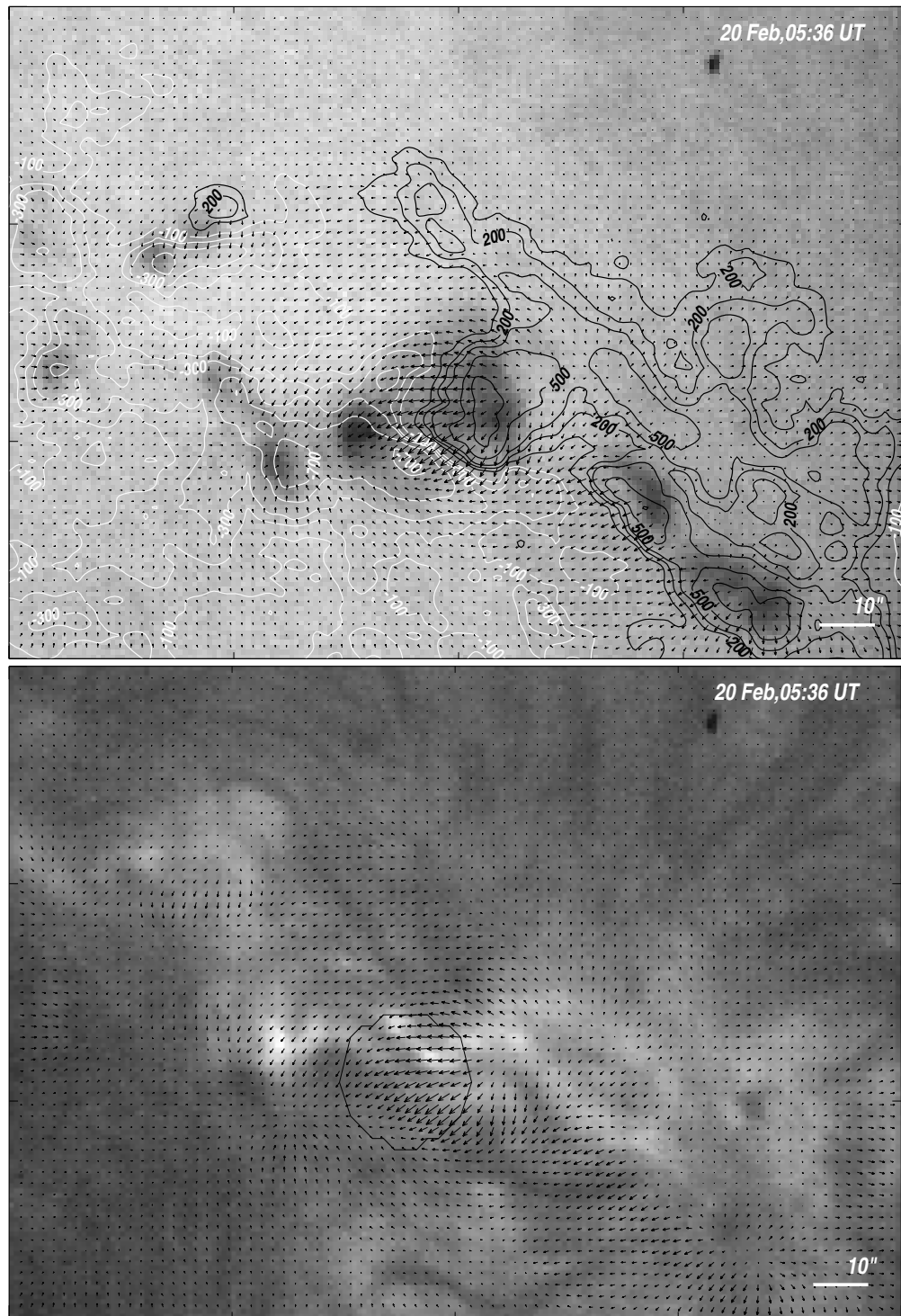


Figure 4.5: The computed potential field over laid on CaI (a) and H α (b) images of the of the active region NOAA 7843, observed 20 Feb 1995, 05:03 UT

At the location *1pt*, the orientation of the filament was seen almost perpendicular to the computed transverse potential field B_t^{pot} direction. This implies low shear of the magnetic field configuration, and less free energy. The flare productivity of this region was observed to be considerably low compared to other locations of high magnetic field gradient. This was perhaps attributed to a relatively slow evolution at this location, which might have provided enough time to relax the magnetic field lines, without buildup of much stress in the magnetic field configuration. At the location *2pt*, the filament showed significant amount of deviation from the potential field configuration. The transverse component of the potential field, showed slight angle with the filament, in the image obtained at 05:30UT, while in 06:30 UT image the angle is largely decreased and the potential field direction run almost parallel to the filament. This indicates an energy build up in the magnetic field configuration due to the EFRs. Most of the sub-flares including a C1.1 flare were observed at this location. On February 20, 1995, the filament passing across the delta spot also showed large shear. Here the transverse potential field direction showed large angle to the neutral line filament at the location of high magnetic field gradient, indicating a sheared magnetic field configuration.

4.1.3 Conclusion

During the three days of evolution of NOAA 7843, the active region had under gone a lot of changes, produced a number of sub-flares and X-ray C-class flares. Near simultaneous observations of the longitudinal magnetic field, $H\alpha$ and CaI photospheric images were obtained for this region. The morphological evolution of the active region was analysed, which showed large changes due to the emergence of new magnetic fluxes. On February 18, 1995 only a few sunspots were seen, which implied simple magnetic field structure. Later, on February 19, 1995, large number of emerging flux regions were noticed. The proximity of these EFRs, with the existing flux regions produced large magnetic field gradients, which in turn resulted in flux cancellation and flares. The comparison between the computed potential field and the $H\alpha$ filamentary structures showed large deviations from

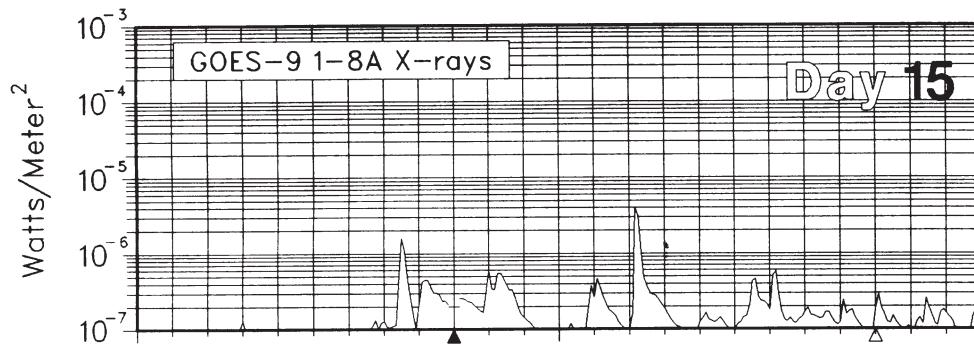


Figure 4.6: *GOES X-ray flare data of the active region NOAA 8032, for 15 April 1997. In figure the x-axis is marked in hours*

the potential field configuration, and most of these locations coincided with high magnetic field gradients. At one of these locations high gradient was present and the neutral line was found crossing perpendicular to the computed potential field. The locations of most of the flares were the sheared regions, i.e., where the filament structure largely deviated from the potential field configuration, and also large magnetic field gradients were present.

4.2 A rapidly evolving active region NOAA 8032 observed on April 15, 1997

4.2.1 Observations

The region NOAA 8032 of April 15, 1997 was observed to evolve rapidly in its magnetic and chromospheric structures. The USO observation of this region begun around 05:25 UT, when it was located at S23 E13. The Solar Geophysical Data reported a number of B class and two C class flares during its 10 hours of evolution. The spikes corresponding to the rapid emergence of magnetic flux region and the associated flaring activity is evident in the GOES X-ray data (Fig. 4.6). A large number of surges and other activities such as filament eruption and reorientation were also noticed during this period. The SOHO/EIT, Fe IX/X, 171 Å, transition region observations were also acquired and analyzed for this region, which showed loop formations and repeated brightening due to new emerging

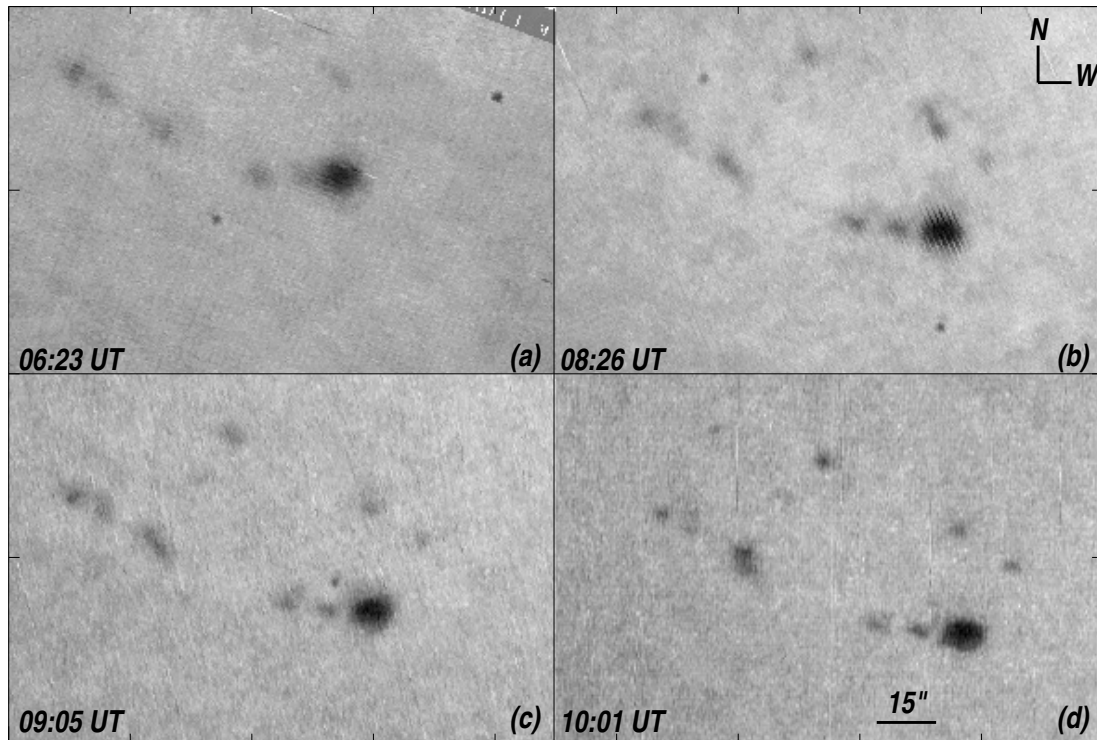


Figure 4.7: *The continuum images taken at the wing of CaI 6122 Å line for the active region NOAA 8032 on 15 April 1997.*

flux regions. At USO we have taken near-simultaneous photospheric and magnetic field observations of this active region.

The active region NOAA 8032 showed up in CaI 6122 Å image as a group of small pores (Fig. 4.7). The magnetogram showed that the leading spot had a negative polarity (Fig. 4.7). The evolution of the longitudinal magnetic field structure of the active region during 05:23 - 10:01 UT is shown in the Fig. 4.8. The contours are made for magnetic field values upto ± 750 Gauss, at the levels of $\pm 50, \pm 100, \pm 250, \pm 500, \pm 750$ Gauss. Fig. 4.9 shows the development of magnetic field gradient at various sites of this active region. The calculated potential field is shown in the Fig. 4.10, while the loop structures seen in SOHO/EIT Fe IX/X 171 Å images for this active region are presented in Fig. 4.11.

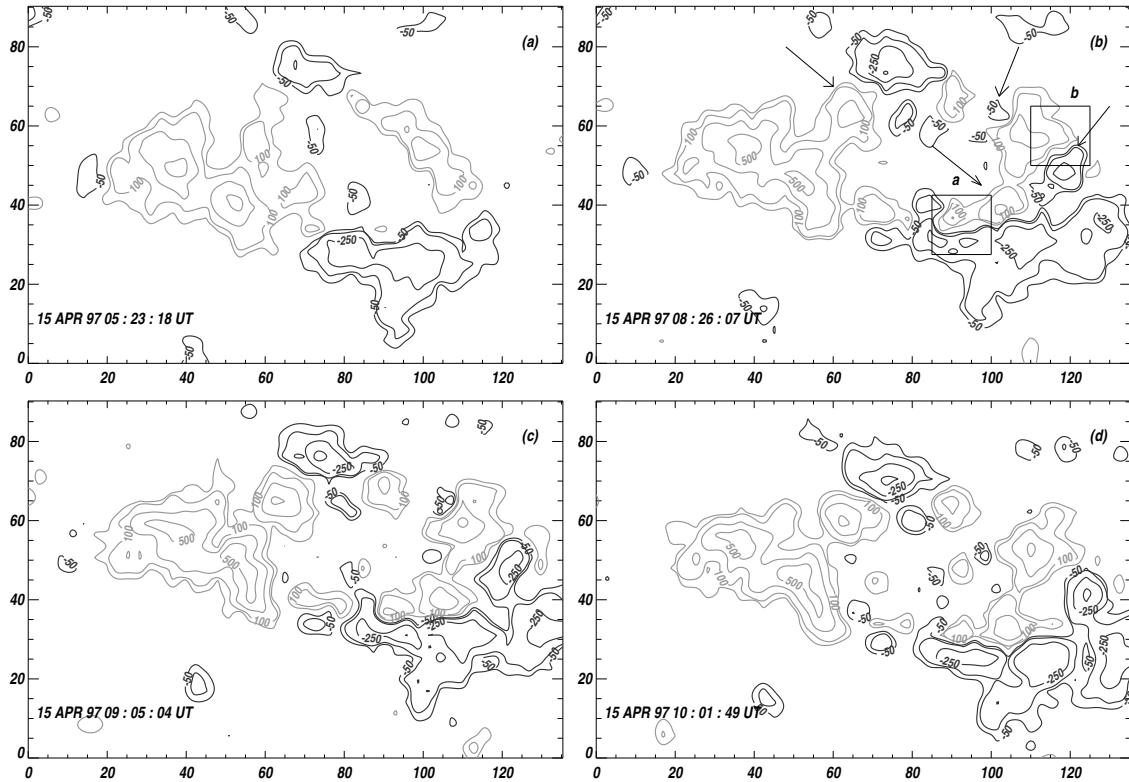


Figure 4.8: *The contour plots showing the evolution of active region NOAA 8032 for a time period of 05:23 UT to 10:01 UT. The contours are plotted for ± 50 , ± 100 , ± 250 , ± 500 and ± 750 Gauss. White and black contours represent positive and negative polarities respectively.*

4.2.2 Discussion and results

Magnetic flux change, flux imbalance, and emerging flux regions

Fig. 4.8(a) to (d) show the contour plots of magnetograms, obtained on April 15, 1997 at 05:23, 08:26, 09:05, and 10:01 UT respectively. The contour plots show clear evidence of the EFRs and corresponding magnetic field changes in this active region, some of them marked with arrows in the figure. Major changes in the fields occurred during the initial stages of evolution, i.e., within 3 to 4 hours after the beginning of our observations at 05:20 UT. Comparison of the images obtained around 05:23UT and 08:26UT shows the location of two of the EFRs as enclosed in small rectangular boxes *a* and *b* in Fig. 4.8(b). As evident in the contour plots, most of the new flux regions emerged very close to existing magnetic flux area i.e., within 10 - 15 arc-seconds. The new negative flux at *b* emerged in the middle of the existing positive polarity region creating a large magnetic field gradient. According to SGD (May 1997, Number 633, Part1), GOES X-ray data the flare activity at this active region started around 07:30UT. Even though the magnetogram data was not available at the time of flare, the images obtained around 08:26 UT showed a clear evidence of EFRs at the flare site. It can be inferred that, emergence of new flux region had started before the first X-ray flare, and perhaps the fluxes triggered the flare . Continuous occurrence of sub-flares, surges and filament eruption and its reorientation were observed from USO H α images obtained during the entire period of observation. The emergence of new fluxes and its interaction with the existing fields might be the reason for the observed flares and related activities. Similar observations of surges and H α compact flares due to the rapid flux emergence have been reported by Kurokawa (1988). Our observation supports the earlier observations of flux emergence and related flare and surge activities (*e.g.* Kurokawa 1986; Debi Prasad *et al.* 1998).

Martres *et al.* (1968) and Severny (1969) have studied the behavior of the total flux and net flux in active regions undergoing flare activities. They concluded that there are significant changes in these quantities during the course of flares. We have analysed the changes in the positive and negative flux in region NOAA 8032. These are calculated

for the for the entire active region as well as for the locations where the emergence of magnetic flux was observed i.e., areas enclosed by the boxes *a* and *b* in Fig. 4.8(b). In the magnetogram taken around 05:23 UT, more positive flux was present as compared to that at 08:36 UT, which implies a reduction of flux imbalance. Later, an increase and then again a decrease was observed in the net positive flux. This oscillation of the magnetic flux can perhaps be attributed to the continuous emergence and cancellation of fluxes during the flare activity. Flux changes were calculated in specific areas of EFRs marked by small boxes on the contour plot as listed in table 4.1. This study revealed

Table 4.1: *Flux changes at the location of EFRs*

<i>Flux</i>		<i>location a</i>			
<i>Maxwell</i>	05:23UT	08:26UT	09:05UT	10:01UT	
Positive	9.9×10^{16}	4.0×10^{17}	6.4×10^{17}	3.44×10^{17}	
Negative	1.31×10^{18}	1.02×10^{18}	1.33×10^{18}	1.28×10^{18}	

<i>Flux</i>		<i>location b</i>			
<i>Maxwell</i>	05:23UT	08:26UT	09:05UT	10:01UT	
Positive	1.52×10^{18}	1.00×10^{18}	9.0×10^{17}	5.12×10^{17}	
Negative	3.9×10^{16}	8.6×10^{17}	1.0×10^{18}	1.2×10^{18}	

that EFRs evolved considerably when the flare occurred. At these regions flux changes at a rate of approximately $10^{13} \text{ Mx s}^{-1}$ was found which conforms with earlier observations by Ribes (1969) and Rust (1972). At the location *b* of EFR the magnetic flux of negative polarity gradually increased while the positive polarity decreased. This observation was in confirmation with Ribes' results that the flare occurred when the magnetic flux in one feature is increasing and decreasing in another adjoining area.

Magnetic field gradient

Magnetic field gradient is a more important parameter to decide the flare location than the strength alone of the magnetic field (Gopasyuk *et al.* 1962). Large gradients in the longitudinal field were reported in earlier observations by Rust (1973) and Severny (1969). We have carried out magnetic field gradient calculation for the above active region, which

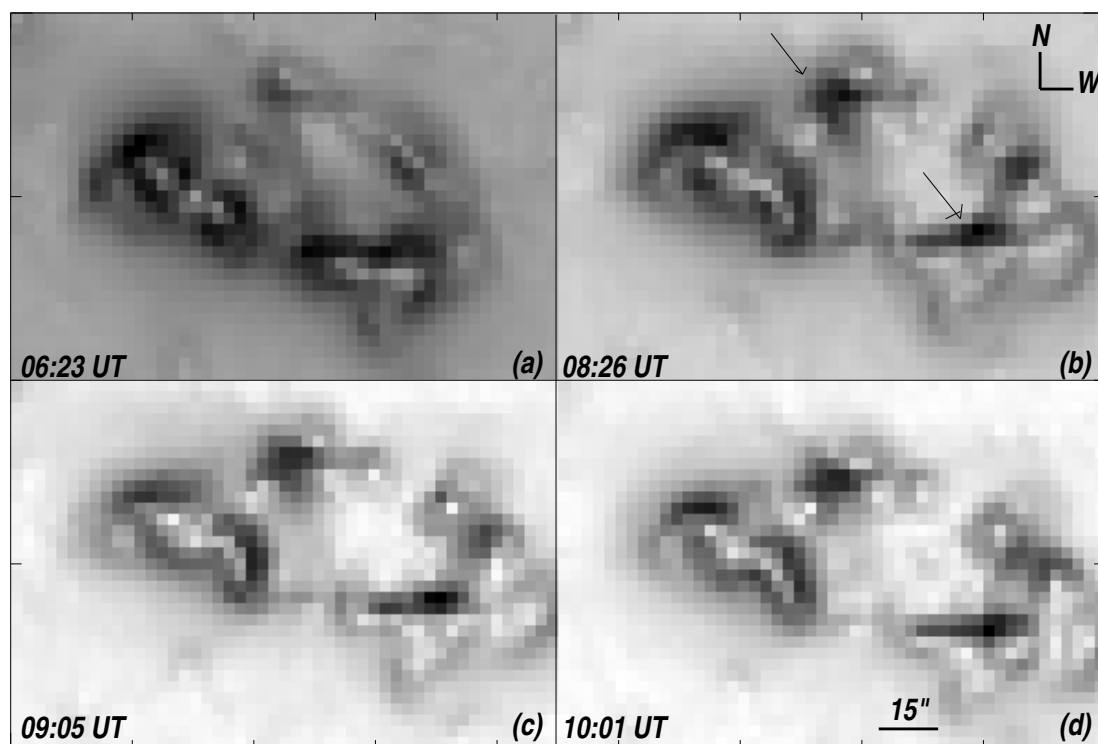


Figure 4.9: *The magnetic field gradient for the active region NOAA 8032 on 15 April 1997.*

is shown in the Fig 4.9(a) to (d). The regions marked with arrows indicate the specific locations where increase of magnetic field gradient occurred due to the emergence of new fluxes during 05:23 - 10:01 UT. In particular strong gradient were observed due to new EFRs in the neighborhood of the existing opposite polarities. This strong horizontal gradient might have favoured continuous occurrence of sub-flares, surges and related activities in NOAA 8032.

Potential field calculation and comparison with Fe IX/X transition region loops

Potential field calculation is carried out for the active region NOAA 8032 using Schmidt technique and observed flux distribution obtained from USO VMGs. Fig. 4.10(a) to (d) show the calculated transverse component of the potential field, B_t^{pot} overlaid on contour plots of the observed longitudinal magnetic fields B_l . The direction of magnetic field lines joining opposite polarity sites are shown in the potential field plots. The rearrangement of the field lines due to the emergence of new flux regions is also evident in these plots. From the comparison of the calculated potential field at 05:23 UT and 08:26 UT, the emerging flux flare model of Heyvaerts *et al.* (1977) may be visualised. At location *b* the emergence of new negative flux into the existing positive polarity produced new loops within the old one. According to Heyvaerts' flare model such loop systems can develop a current sheet where continuous reconnection of the flux loops and thus flares can take place. Fig. 4.11 show the SOHO/EIT images obtained around the time of magnetogram observations. The calculated transverse potential field shows the photospheric or low-lying connections while the EIT Ultraviolet images shows higher loops as observed in the coronal heights. The loop structure initially showed simple bipolar nature of the active region, as shown in Figure 4.11a. A number of new loops are noticed on further development of the active region, which correspond to the emergence of new magnetic flux areas. Comparing the USO longitudinal magnetic map and SOHO/EIT images, we find that the bright areas in SOHO/EIT images correspond to the location of EFRs or high magnetic field gradient. Due to the low resolution of the loops it is difficult to distinguish a particular loop which

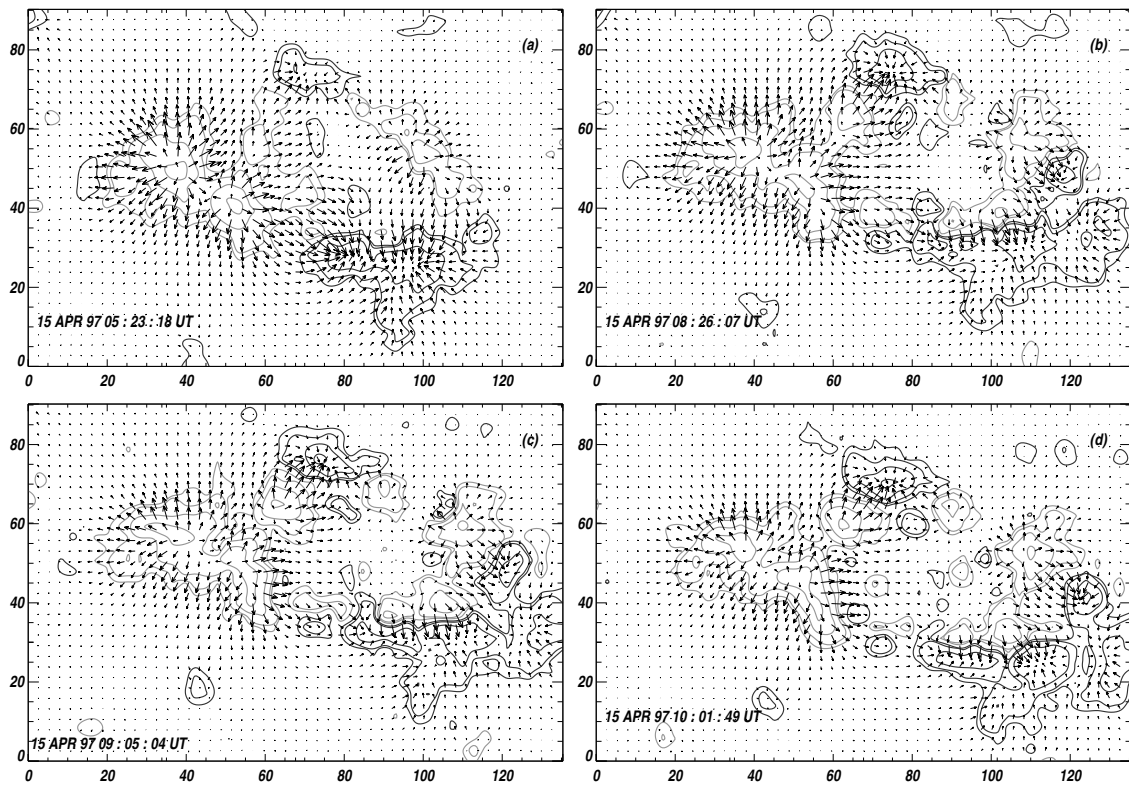


Figure 4.10: *Calculated potential field map of the region NOAA 8032.*

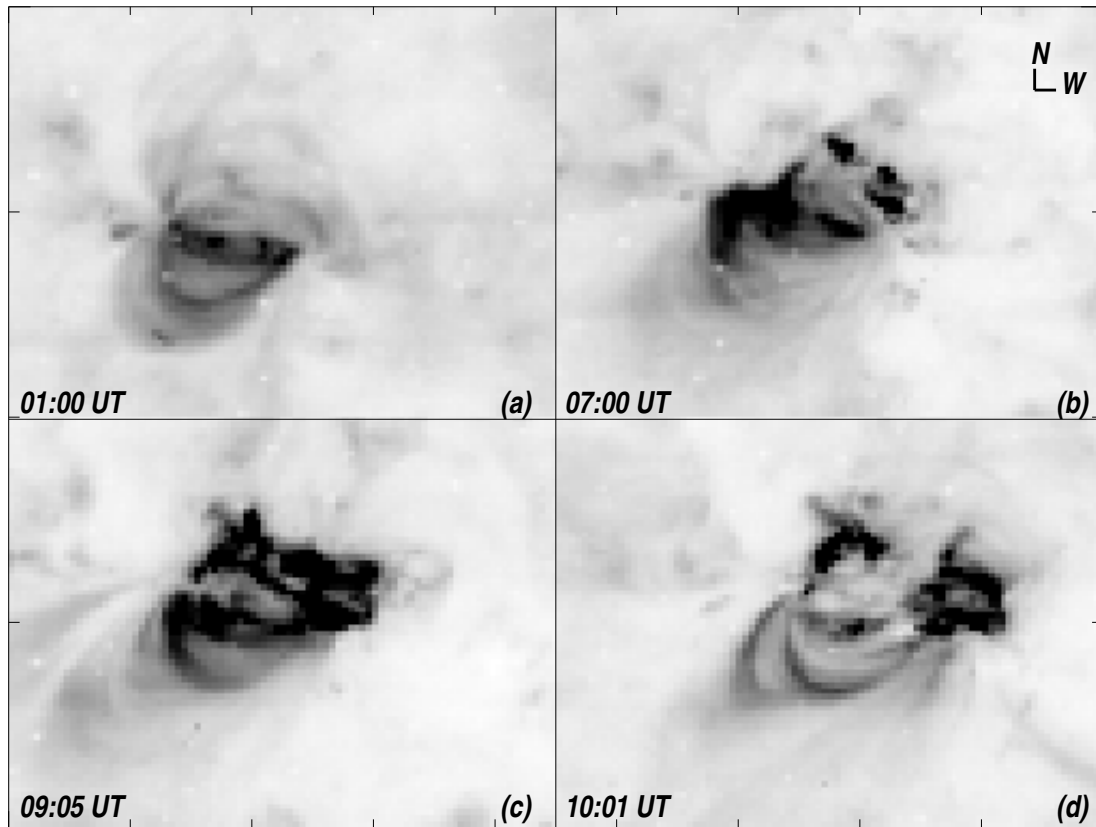


Figure 4.11: *The SOHO/EIT images for the active region NOAA 8032 on 15 April 1997.*

connects to the opposite polarity at the nearby the locations of EFRs. This make it difficult to obtain a measure of non-potentiality of the magnetic field structure using the loops. However it can be inferred that the evolution of loops connecting a simple bipolar structure evolved to a more complicated system as a result of new flux emergence in this region.

4.2.3 Conclusion

The GOES X-ray flare data showed a number of sub-flares and two C-class flares during the 8-9 hours of the evolution of NOAA 8032. Although no major flares were recorded to occur in this region, continuous recurrence of sub-flares, surges, filament formation and

re-orientation of structures were noticed. The magnetic field evolution of this active region has been studied to ascertain its role in flare and surge production. From the comparison of the magnetograms obtained around 05:23 and 08:20UT, large changes were observed in magnetic field configuration due the emergence new magnetic flux regions. Most of the new emergence occurred very close to (with in 10 - 15 arc-sec) the existing magnetic regions with opposite polarities. Strong magnetic field gradients developed due to these EFRs new flux regions. Moreover in some cases the EFRs showed motions so as to push itself into the already existing opposite polarity regions.

The first reported flare in NOAA 8032 started around 07:40 UT. The magnetogram obtained after the flare onset at 08:23 UT showed clear evidence of the EFRs. Although no magnetograms were available before the flare onset time, it can be inferred from the magnetograms obtained before and after the flares, that EFRs perhaps triggered the flares. This is in confirmation with the earlier observations made by Rust (1974) and Debi Prasad *et al.* (1998). Due to the emergence of magnetic flux regions, increase in magnetic field gradient and flux changes were observed throughout the evolution of this active region. The EFRs driven reconnection of field lines and the subsequent flux cancellation might be the reason for the continuous occurrence of sub-flares and other related activities. Similar observations were reported of the EFR driven reconnection and flux cancellation were reported by Wang & Shi (1993). The flux changes at the two adjoining locations of opposite polarities flux regions showed increase in one type of polarity while a decrease in the opposite polarity flux during the evolution. The potential field calculation showed rearrangement of the field lines during the evolution of the active region. Similar loop formation and reorientation were also observed in the transition region loops.

4.3 Active region NOAA 8038 observed during May 10 - 13, 1997

4.3.1 Observation

The observation of the active region NOAA 8038 began at USO on May 10, 1997 at 04:00 UT when it was located at N20E17. Fig. 4.12 shows longitudinal magnetogram and CaI images of this region during May 10-13, 1997. The magnetogram of the region showed a simple magnetic field configuration in which a dominant sunspot was seen surrounded by weak fluxes of opposite polarity. Corresponding H α images showed that the weak fluxes were represented by bright plages. On May 10 and 11, 1997 no activity was observed in this region. However on May 12, 1997/04:45 UT, it produced a two-ribbon flare of 1N/C1.3 importance, shown in Fig. 4.13. This flare started around 04:45 UT, attained the maximum at 04:56 UT and ended at 06:00 UT. Along with the flare, associated surges and filament eruption were also noticed. Magnetograms at USO were not taken continuously during this flare, therefore SOHO/MDI full disk magnetograms were also used for certain types of analysis, including the estimation of the proper motion of the fluxes.

4.3.2 Discussion and Results

The USO magnetograms showed that the active region NOAA 8038, possessed a simple magnetic field configuration, having a dominant positive polarity sunspot surrounded by scattered plages of opposite polarity. The concentration of negative polarity plages were found mostly in the intergranular lanes, which is evident from the size of the magnetic field pattern found in this region. These “network field” pattern show the typical size of supergranular cells of around 25, 000 - 30, 000 km. Also the observed rearrangement of fluxes are suggestive of a close relationship between the horizontal supergranular velocity field and the flux motions. The magnetic field evolution of this active region associated with the supergranular flow during May 10 - 13, 1997, is evident by Fig. 4.12. During the course of evolution of the active region, the main sunspot remains unchanged with only a slight rotation while the network field was found to diffuse all over a large area.

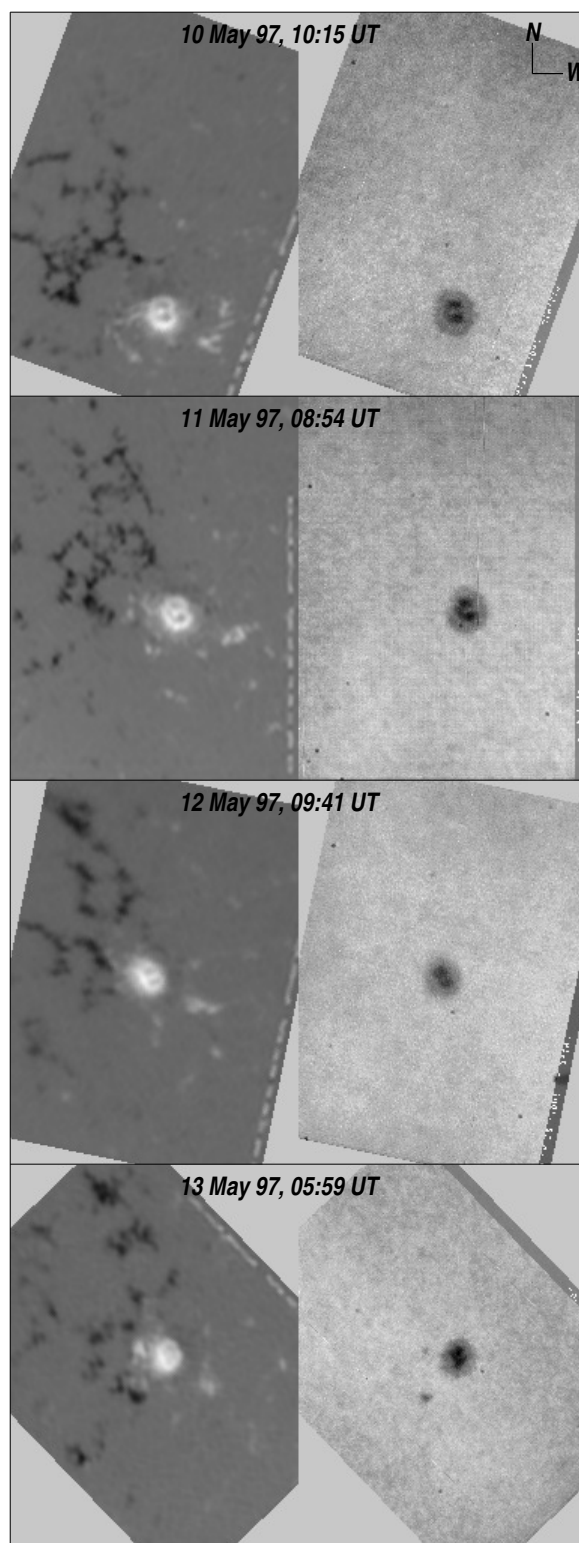


Figure 4.12: Magnetograms (left panel) and CaI (right panel) images of the active region NOAA 8038, observed during 10 - 13 May 1997.

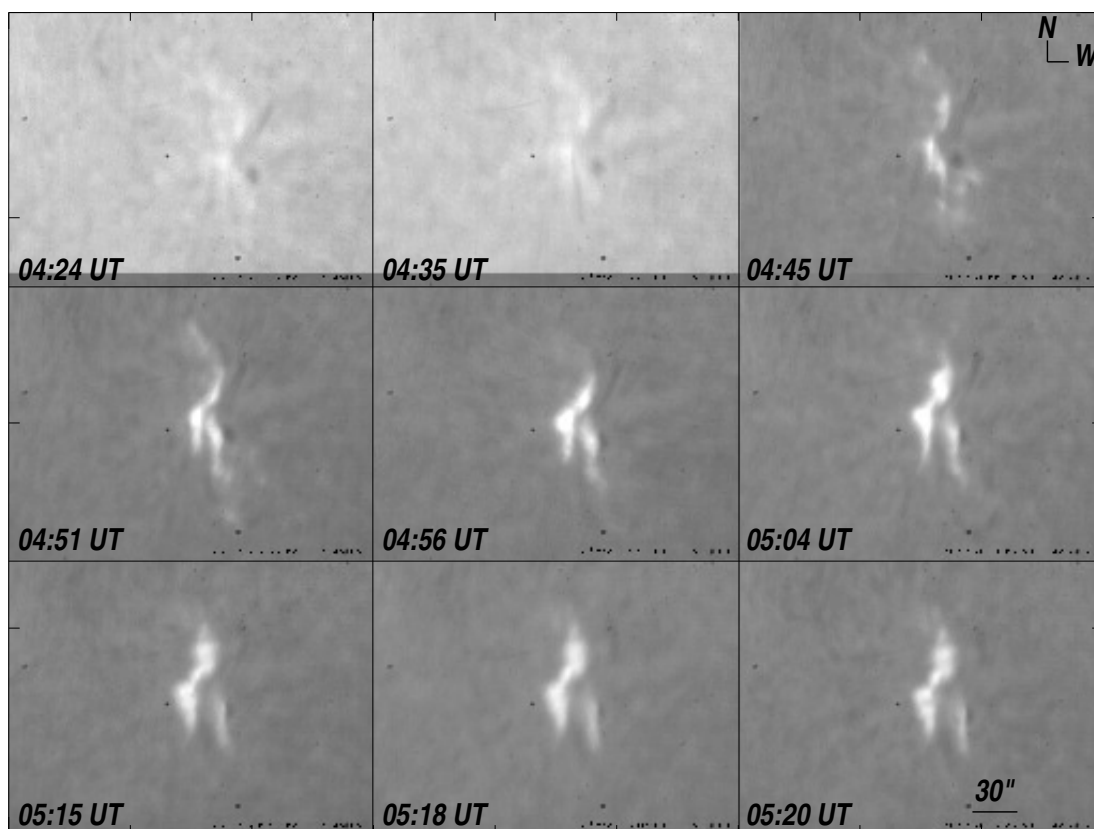


Figure 4.13: A $H\alpha$ (1N/C1.3) Flare observed from USO on 12 May 1997 at NOAA 8038.

Horizontal motion of the magnetic fluxes associated with supergranular flows

A variety of factors may lead to the energy build up in an active region. One of these factor is the motion at the photospheric level resulting in the shearing and stretching of the magnetic field structures (Sakurai 1976; Zirin & Lazareff 1975). The photospheric motion corresponding to the sunspots may produce twisting of the field lines which in turn result in helicity and energy storage. The stored or free energy due to these motions can be eventually released in the form of flares when triggered by an instability in the region. The sunspot proper motion and its relation with flare has been studied for the active region NOAA 2372 by Ambastha *et al.*(1988). They found that these motions gave rise to positive build-up of magnetic energy which was sufficient to account for the net energy release from the active region in the form of flares.

Apart from the motions of sunspots and their corresponding large fluxes, motions in weaker field areas are also observed. Flux motions associated with horizontal supergranular velocity field were observed in the active region NOAA 8038, during May 10 - 13, 1997. This active region consists of a stable sunspot with positive polarity and surrounding network fields with opposite polarity. The network fluxes showed considerable horizontal motions during the evolution of the active region. For visualising the horizontal motion of the fluxes, a movie was made using IDL software where several frames were spatially registered with the help of sunspot as the reference. Due to the lack of continuous observations at USO for this region, a time series of magnetograms obtained from SOHO/MDI instrument, was used for the movie. Some of the frames used in the movie are shown in Fig. 4.14. The network flux motion was very clearly evident in the movie. The reformation and accumulation of network magnetic fluxes along the supergranular boundary lanes were also observed. Negative fluxes were mostly found to be moving along the boundary lanes while new positive fluxes appeared or emerged very close to the sunspot. These positive fluxes later moved towards the network field. The negative fluxes close to the sunspot showed a motion towards the sunspot, while these located farther moved in the opposite direction. The flux dissipation and cancellations at sites were also observed in

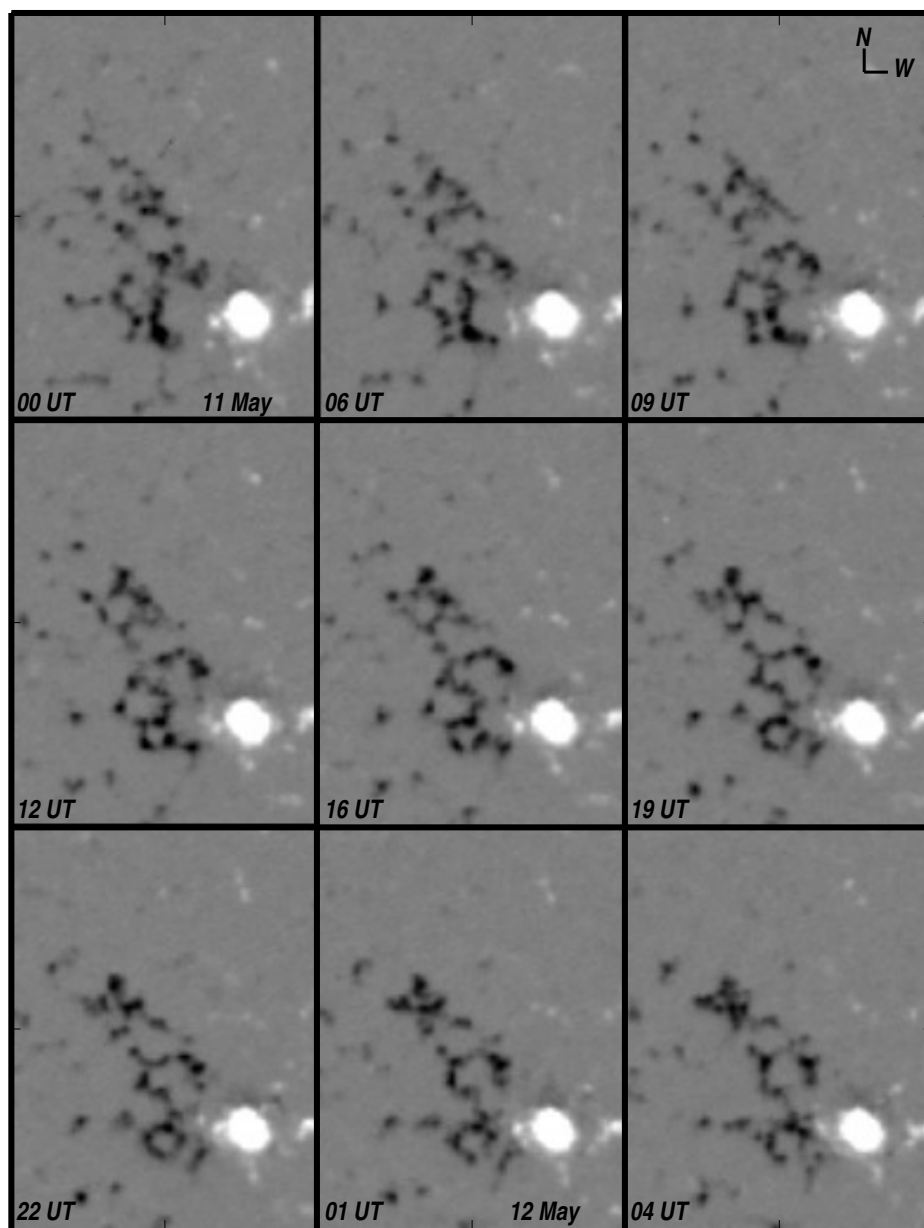


Figure 4.14: *Enlarged region of the SOHO full disk magnetograms used for the study of proper motion of network fluxes.*

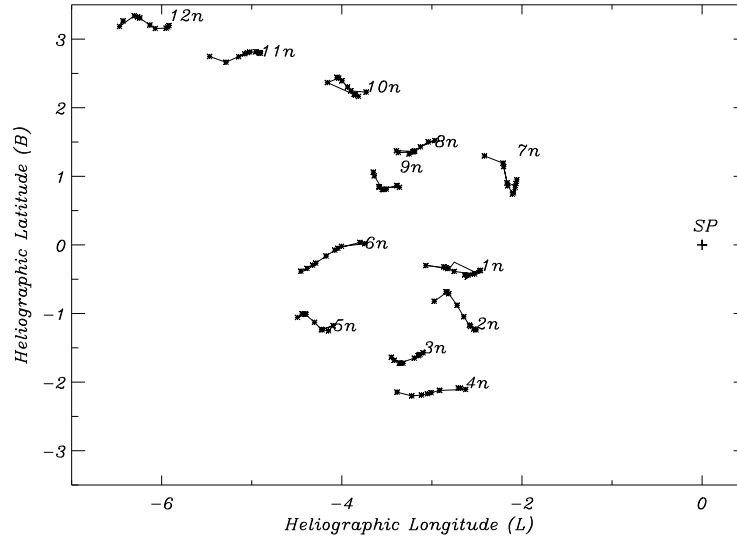


Figure 4.15: *Proper motion of the network fluxes.*

the movie.

We have estimated the motion of the foot-points of the network magnetic fluxes for the day of May 11, 1997 during the period 00:00 to 22:00 UT. The motion of the negative fluxes were estimated by identifying a number of locations corresponding to the foot-points of the negative n and positive p fluxes in the active region. All the identified fluxes were followed for a time period of 22 hours, at an interval of around 2 hours. For the estimation of flux motion, the sunspot is assumed to be stationary, while the motion of the network field is measured with respect to the sunspot. The heliographic latitude and longitude of each point is then computed and plotted as shown in Fig. 4.15.

Most of the fluxes show a motion of around 0.5 to 1 heliographic degrees along the latitude with respect to the main sunspot, for the time period of one day. The velocity estimation of the fluxes showed a horizontal flow of around 0.3 - 0.8 km/sec, which is in confirmation with earlier observations of Worden & Simon (1976). The histogram in Fig. 4.16 shows the velocity distribution of the fluxes. The peak velocity distribution is found to be in between 650 and 750 m/sec. For the positive fluxes the velocities were

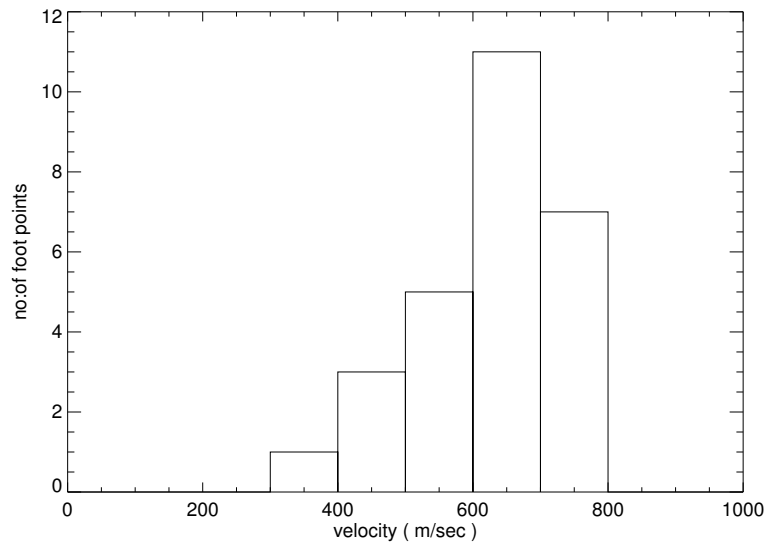


Figure 4.16: *Histogram showing the velocity distribution of the network magnetic flux elements.*

slightly higher than the negative fluxes and the motion was in opposite direction and was towards the network field. The velocity field of the fluxes are suggestive that the motion is associated with the horizontal flow of the supergranules.

We suggest that relatively fast photospheric foot-point motions of the fluxes might have produced the required energy for the May 12 flare. The negative fluxes near by the sunspot moved towards the sunspot while, the far away fluxes moved in a direction away from the sunspot, which could produce a twist of the field to produce the energy build up.

Role of EFRs, flux motion and magnetic field gradient for the trigger of the flare

There are a number of mechanisms for the trigger of solar flares as reported in the literature. One of these is the flux emergence and cancellation. The relation of flux cancellation and trigger of flares were reported by Livi *et. al* (1989). In their study they reported both small and big flares near the cancelling magnetic field and concluded that the flux cancellation is the common denominator among all the observed association of flares to changing

magnetic field. They found that magnetic fields migrate together, and a high magnetic field gradient is observed as long as the fields are cancelling. In a recent study, Wang & Shi (1993) observed that emerging flux region driven flux cancellation could play a role as the trigger for flares.

We have carried out a similar study for active region NOAA 8038 to understand the relation between flux emergence and cancellation for occurrence of solar flares. In the active region NOAA 8038 emergence of new positive fluxes were noticed during 11 - 12 May 1997, some of which are marked in the Fig. 4.18. Most of the positive fluxes emerged very close to the main sunspot. After the appearance, the new positive fluxes moved away from the sunspot in a direction opposite to the motion of the network field. The motion brings the positive and negative network fluxes closer together to produce stronger magnetic field gradient and flux cancellation. Analysis of the data showed several positive EFRs such as '4', '5' and '6' marked in the Fig. 4.18. The horizontal velocity of these fluxes were found similar to horizontal photospheric network velocity.

Magnetic field gradient resulted due to the emergence and motion of most of the positive fluxes were considerably small, except in the case of the positive flux '6'. On cancellation or dissipation, most fluxes did not produce any observable flares, but in the case of the positive flux marked as '6', the motion towards the network field resulted in building the magnetic field gradient. We have computed the magnetic field gradient using the longitudinal magnetic field observations obtained at 00:04 and 03:16 UT on May 12, 1997. The longitudinal magnetic field contours overlaid on the computed magnetic field gradient is shown in Fig. 4.17. The magnetic neutral line i.e., $B_l = 0$, passes through the middle of ± 10 Gauss contours. An increased magnetic field gradient can be noticed at the location of flux collision which is evident in both longitudinal magnetogram contours and calculated magnetic field gradient. The increased magnetic field gradient is at the interface of the positive flux '6' and the negative network flux. The first kernel of the May 12 flare started close to this high magnetic field gradient location which is marked as f in the figure.

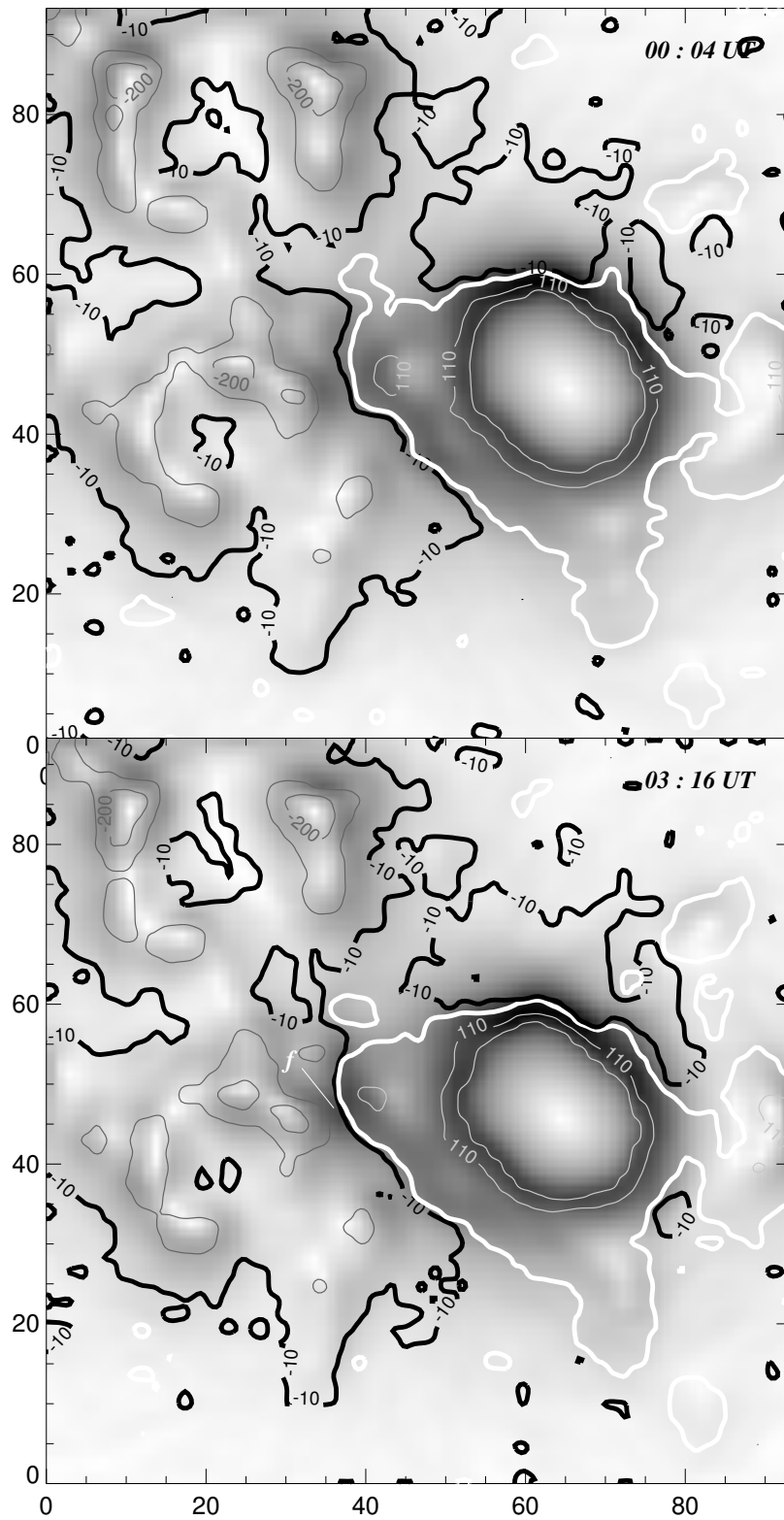


Figure 4.17: Longitudinal magnetic field contours overlaid on magnetic field gradient, on 12 May 1997. Initial flare kernel appeared at the location marked as 'f'. In the figure North is up and West is right, and the scale is in arc-seconds.

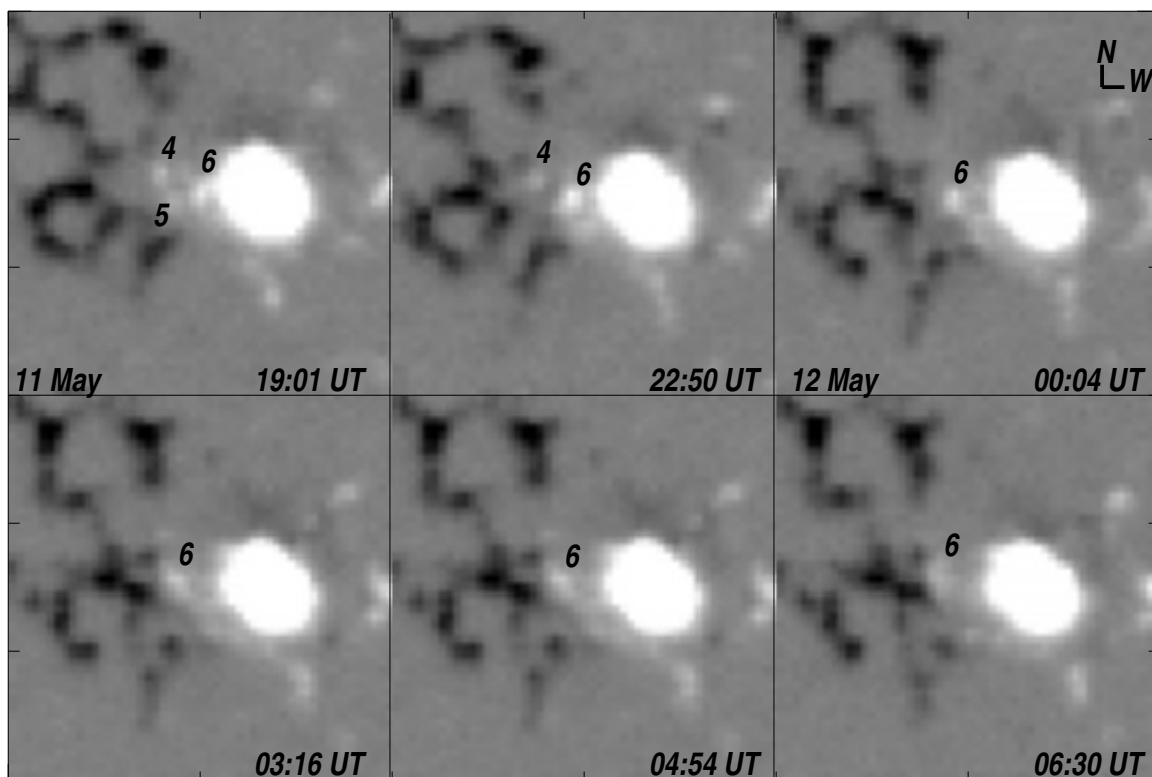


Figure 4.18: *The cancellation of the flux marked as '6', produced a flare at this region on 12 May 1997, at 04:45 UT.*

Table 4.2: *Flux cancellation at the flaring site on May 12, 1997*

Time (UT)	Negative flux (Maxwell)	Positive flux (Maxwell)	Total flux (Maxwell)
03:16	-4.33×10^{13}	3.13×10^{14}	3.56×10^{14}
04:54	-4.11×10^{13}	2.53×10^{14}	2.94×10^{14}
06:30	-8.39×10^{12}	1.28×10^{14}	2.11×10^{14}

Development of magnetic field gradient due to the collision of positive flux ‘6’ and negative flux is also evident in the longitudinal magnetic field observations shown in Fig 4.17. This development resulted in flux cancellation and subsequent flaring. The initial kernel of the flare was noticed at the location of the flux cancellation. This suggests that the flux cancellation process perhaps provided the trigger for May 12 flare. Later the flare developed into a two ribbon structure. The total flux before and after the flare is computed at the location of high magnetic field gradient, with in a rectangular area which enclosed the flaring site. This location is marked with δ in the Fig. 4.18. The computed flux changes are listed in Table 4.2, which indicated a reduction in both the positive and negative fluxes after the flare.

4.3.3 Conclusion

In the active region NOAA 8038, apart from some sub-flares, only one 1N/C1.3 flare was reported on May 12, 1997/04:24 UT during the three day period of 10 - 13 May 1997. As observed from USO and SOHO magnetograms, we inferred large horizontal motions of the network photospheric magnetic field foot-points. Horizontal velocities of these foot points motion were calculated between 300 - 800 m/s. We suggest that motions of these foot-points might have accumulated enough energy for the May 12 flare.

Prior to the flare, emergence of positive fluxes were also observed. These fluxes moved in direction opposite to the network field. Most of the positive fluxes dissipated or cancelled without producing any considerable magnetic field gradient. One of the positive EFR emerged very close to the sunspot, and subsequently moved towards the network field producing strong magnetic field gradient. This resulted in flux cancellation, which might

have triggered the May 12 flare. We noted that the initial kernel of the flare appeared at the location of the flux cancellation. This suggests the association of the 1N/C1.3 flare with the canceling magnetic field. However not all the observed flux cancellation could trigger flares, which could indicate that high magnetic field gradient and adequate magnetic energy build up may be other prerequisite criterion for the triggering of solar flares.

4.4 Summary of results

NOAA 8038 observed during May 10 - 12, 1997 was a slowly evolving active region, while the other two active regions, NOAA 7843 and NOAA 8032, observed on February 18 - 20, 1995, and April 15, 1997 were rapidly evolving. Some important results obtained from their analysis are listed below,

- Energy build up: In the case of slowly evolving active region NOAA 8038, buildup of energy for the observed flares was contributed mainly due to the motions of magnetic fluxes. With respect to the leading positive polarity sunspot, the negative polarity network magnetic field structures showed motions. These motions were in opposite directions for fluxes close to and those away from the main sunspot. On the other hand for the rapidly evolving active regions, the energy buildup was mainly due to the emergence of new fluxes of opposite polarity nearby the existing magnetic structures.
- Emerging flux regions: Emerging flux regions were one of the common phenomenon noticed before the occurrence of a flare in all the three active regions. In NOAA 8038, the positive polarity EFR which triggered the flare emerged very close to the main sunspot, i.e., within 2 - 3 arc-seconds. After its emergence the EFR moved away from the sunspot and collided with the opposite polarity network field. In the other two active regions the EFR appeared very close to the opposite polarity structures. Large number of EFRs were observed in rapidly evolving region while

comparatively fewer number of EFRs were noticed in the case of NOAA 8038

- Flare productivity: Flares and surges were observed almost continuously in rapidly evolving active regions throughout the period of evolution, while in the case of NOAA 8038, only one flare was reported in its three days of evolution.
- Magnetic field gradient: High magnetic field gradient was another important property observed at the flaring locations. For NOAA 8038 magnetic field gradient developed due to the motion and collision of EFR with the opposite polarity network fluxes, while in the other two cases the proximity of the flux emergence led to its increase.
- Flux cancellation: In both cases flux cancellation was observed before/during the flare. This process was very evident for NOAA 8038, while in other two cases change in the net magnetic flux was observed prior to the flares. In rapidly evolving regions, one type of polarity was found to be decreasing while the other was increasing at the site of the emerging flux regions. This apparently indicated the emergence and/or cancellation of the fluxes.
- Sheared magnetic structures: The computed potential field direction showed large deviation from the $H\alpha$ filament structures at the locations of high magnetic field gradients. In the absence of observation of transverse component of the magnetic field the $H\alpha$ fibril structures could be used as providing the direction of the field lines. The angle between the computed potential transverse field and $H\alpha$ fibrils thus provided a measure of 'angular shear'. We found that locations of high angular shear were associated with some of the observed flares.

From the above results it can be concluded that, EFRs, high magnetic field gradient, flux cancellation and sheared magnetic structures are some of the observed criterion for the occurrence solar flares.

Chapter 5

Summary and Future Plans

5.1 Summary

5.1.1 Instrumentation

In order to study the flare related magnetic field evolution of active regions, photospheric longitudinal magnetic field, white light, and chromospheric $H\alpha$ observations are some of the important requirements. Keeping this in mind, a digital video magnetograph has been designed, fabricated and successfully installed at USO during the course of this Ph.D. work. This instrument is capable of providing near-simultaneous longitudinal photospheric magnetic field, chromospheric $H\alpha$ (6563 Å), and photospheric CaI (6122 Å) observations using the same telescope and back-end equipment.

The magnetic field measurements are made by using the polarisation properties of the Zeeman components of the photospheric CaI line at 6122 Å (Landé g factor of 1.75). The CaI line has been chosen due to its low Doppler sensitivity, larger line depth and no blend with other solar or atmospheric lines. A variable electro-optic quarter wave retarder, KD*P (Potassium di-Deuterium Phosphate) along with a linear polariser is used for analysing the circular polarisation of the Zeeman components. The filter tuned at 140 mÅ away from the line centre in the blue wing is found to give the best linear response for the field strength up to 1500 Gauss. A field of view (FOV) of $\sim 4 \times 3$ arc-min on the solar disk is imaged using a 699 x 288 pixel CoHU CCD camera in synchronous with the KD*P modulation. The KD*P modulation is achieved by applying $\pm\lambda/4$ voltages of ± 2100 volts

such that the alternate frames are oppositely circular polarised images. These images are stored in separate frame buffers of an image acquisition system. To achieve high signal to noise ratio a large number of images (maximum 256) are added in respective frame buffers and then the difference between left and right circularly polarised images is obtained. This difference is related to the magnetic field strength.

5.1.2 Comparison and calibration of VMG

The comparison of magnetograms obtained at USO, with space borne SOHO/MDI instrument, show a good agreement over all the finer magnetic features. Using the profile line slope method a calibration constant is obtained, for converting the measured Stoke V values in to magnetic field in Gauss. A scatter plot of USO and SOHO/MDI magnetograms show very less scatter which validates of our calibration procedure.

5.1.3 Study of evolution of active regions

Observational data has been obtained for three active regions which had shown moderate flaring activities. The active regions for which the analysis have been carried out are NOAA 7843, NOAA 8032, and NOAA 8038, observed during February 18 - 20, 1995, April 15, 1997, and May 10 - 13, 1997 respectively. A detailed analysis of the above data has been done to understand the magnetic field evolution and flare activity of these regions.

Large morphological changes were observed in NOAA 7843 region during its three days of evolution, i.e. February 18 - 20, 1995. A number of new emerging flux regions were noticed at this region during this period. Flux emergence produced large magnetic field gradients, which in turn led to flux cancellation and flares. A comparison between potential field and $H\alpha$ loop structures showed large deviations in magnetic field configuration from the computed potential field configuration. Locations of most of the flares coincided with the locations of high magnetic field gradient, and shear.

Active region NOAA 8032, observed on April 15, 1997, was also an example of rapidly emerging fluxes. This region produced a number of sub-flares and one C-class flare during

its 8 - 9 hours of evolution. This region was conspicuous by several surges, filament formation and re-orientation. The flares resulted due to rapid emergence of fluxes very close to the existing opposite polarities. Strong magnetic field gradients and flux changes were observed in this active region as a result of flux emergence. These observations suggest that the emergence of new fluxes and flux cancellation driven by it might have triggered the flares and the continuous occurrence of sub-flares, surges, filament eruptions, and re-orientation.

Active region NOAA 8038, observed during May 10 - 13, 1997 was an example of rather simpler active region which consisted of single positive polarity sunspot surrounded by opposite polarity network fluxes. The only flare found at this region was a two ribbon flare of 1N/C1.3 which occurred, on May 12 at 09:45 UT. Large horizontal motions were observed using the network fluxes in this active region, which might have helped in accumulation of sufficient energy for the flare. The emergence and collision of flux with the existing opposite polarity regions increased the magnetic field gradient, which resulted in flux cancellation and perhaps in triggering of the May 12 flare.

The study of the three active regions provided insight in to the relation between the evolution of magnetic fields in active regions and production of moderate flares in simple active regions. Emerging flux regions, large magnetic field gradient and flux cancellations were found to be some of the pre-requisite criteria for solar flares.

5.2 Future Plans

5.2.1 Study of more active regions during the ascending phase of solar cycle 23

More studies of active regions are required to have a better statistical understanding of the flare phenomenon. Since the installation of the magnetograph was completed during the minimum period of solar cycle, the observations were limited to only a few active regions. With the successful installation of the video magnetograph facility at USO, well planned observations and analysis of more active regions of various types can be obtained during

the current ascending phase of solar cycle 23.

5.2.2 Calibration of magnetograph using different methods

A thorough calibration of our magnetograph is required for quantitative measurement of magnetic field. Different methods are reported in literature for the calibration of magnetographs (Cauzzi *et al.* 1993; Varsik 1995). We have used only one of the methods, the line-slope method, for the calibration of our video magnetograph, which showed promising results. The cross check of our results using different methods of calibration is essential to determine most accurate conversion of the Stoke's V measurements to the magnetic field strength.

5.2.3 Vector magnetic field measurement

Need for the full, vector magnetic field information

It is believed that the energy required for the release in solar flare is stored in the stressed magnetic fields, where the field configuration deviates largely from the potential field. Measurement of transverse magnetic field in vector magnetographs showed that in many cases the first $H\alpha$ brightening coincides with the places where the transverse field is nearly parallel to the neutral line. Hagyard *et al.* (1984) defined a term called shear angle, as the angular difference in photosphere between the potential, and the observed transverse fields.

We have used in the present study; $H\alpha$ fibril structures as the tracers of magnetic field lines, which can provide only a qualitative measurement of shear development. But for the quantitative measurement of magnetic shear it is essential to obtain the transverse magnetic field component. Thus the up-gradation of the present VMG to a full vector magnetograph to provide both the longitudinal and transverse magnetic field components is essential in order to understand the process of flare energy build-up and release.

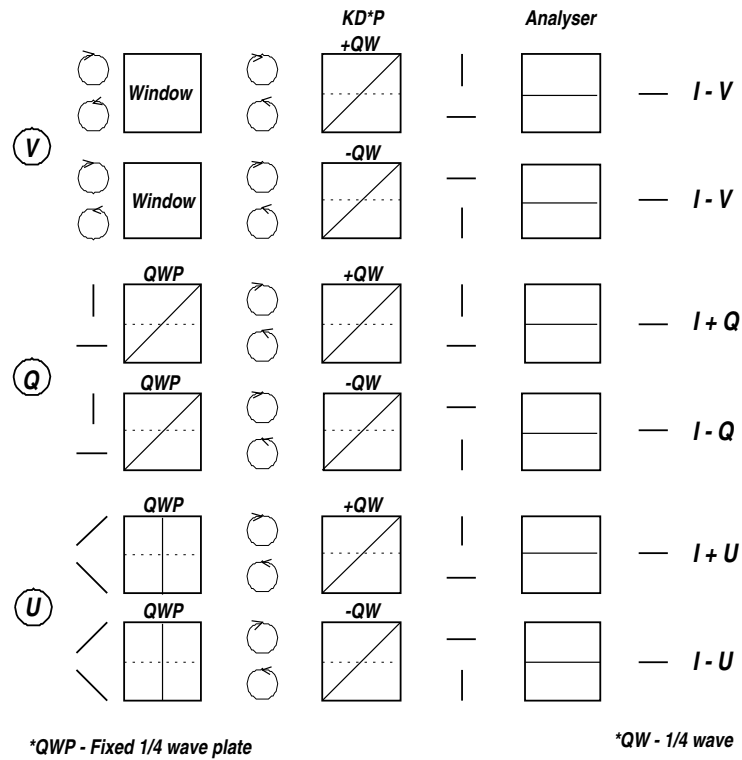


Figure 5.1: The scheme for vector magnetic field measurement. The sequence of operation is listed in the table 5.1. (Adapted from West (1989))

Technique and additional optical components required for vector magnetic field measurements

The observation of the vector magnetic field involve the measurement of both the circular V and linear components (Q and U) of the Stokes parameters. With the existing instrument, the measurement requires two additional quarter waveplates on a rotating wheel. The scheme for the measurement of all the Stokes parameters is illustrated in Fig. 5.1. The Table 5.1 gives the sequence of observational procedure to obtain all the Stokes parameters.

More detailed descriptions for the measurements can be found in West (1989) and Stenflo (1994). The observed Q and U can be utilised for deriving the magnitude and the

Table 5.1: *Full vector magnetic field measurement*

Stokes Parameter	Window	Fixed $\lambda/4$ plate	KD*P
$I + V$	IN	OUT	$+\lambda/4$
$I - V$	IN	OUT	$-\lambda/4$
$I + Q$	OUT	IN (45°)	$+\lambda/4$
$I - Q$	OUT	IN (45°)	$-\lambda/4$
$I + U$	OUT	IN (90°)	$+\lambda/4$
$I - U$	OUT	IN (90°)	$-\lambda/4$

direction of the transverse field (*cf.* chapter 2, section 2).

Problems encountered in linear polarisation measurements

The measurement of transverse magnetic field is more difficult than longitudinal magnetic field component, because the signal strength in case of linear polarisation is almost 5 times weaker than the linear polarisation. Thus in order to avoid the circular crosstalk in linear polarisation, very accurate polarisation measurements are required. The fact that, transverse magnetic field is proportional to the square-root of the total linear polarisation, also imposes the need for accurate measurement of Q and U components for determining the vector magnetic field on the Sun. Another problem which becomes rather important is the instrumental polarisation caused by telescope and other optical components, present in front polarisation analyser module. These effects cause inaccuracies in measurements. For a proper interpretation and analysis of the data, correction for the instrumental polarisation is very essential prior to the measurements.

Since the linearly polarised signal strength is very low, it is required to average a large number of image frames to achieve acceptable signal-to-noise ratio. This requires accurate guiding of the telescope during the time of frame acquisition for averaging process. A second order telescope guiding using correlation tracker which uses an active mirror may provide better results.

Velocity field measurement in an active region

Apart from full vector magnetic field, it is important that line-of-sight velocities in the active region be also obtained. A close relationship is reported between the flare occurrence and line-of-sight velocity fields in the active regions. Martres & Soru-Escout (1977) found that flares occurred in the vicinity of the sites where the magnetic neutral line crossed the velocity neutral line. Another important observation was reported by Ai *et al.* (1991). They observed flare occurrence close to the red-shifted side of the velocity inversion line. Thus, in addition to the magnetic field observations, the line-of-sight velocity field is very useful in predicting the flares in an active region. With some modifications in the observational procedures, control electronics and optical components, it is possible to obtain the dopplergrams with our instrument which will provide the velocity field information in active regions.

With all the above proposed modifications in the existing instrument, we hope to obtain vector magnetic field and Doppler velocity information in addition to the white light and $H\alpha$ measurements. This will provide a better and useful data set for detailed study of the flare phenomena on the Sun.

Appendix A

KD*P High Voltage Power Supply

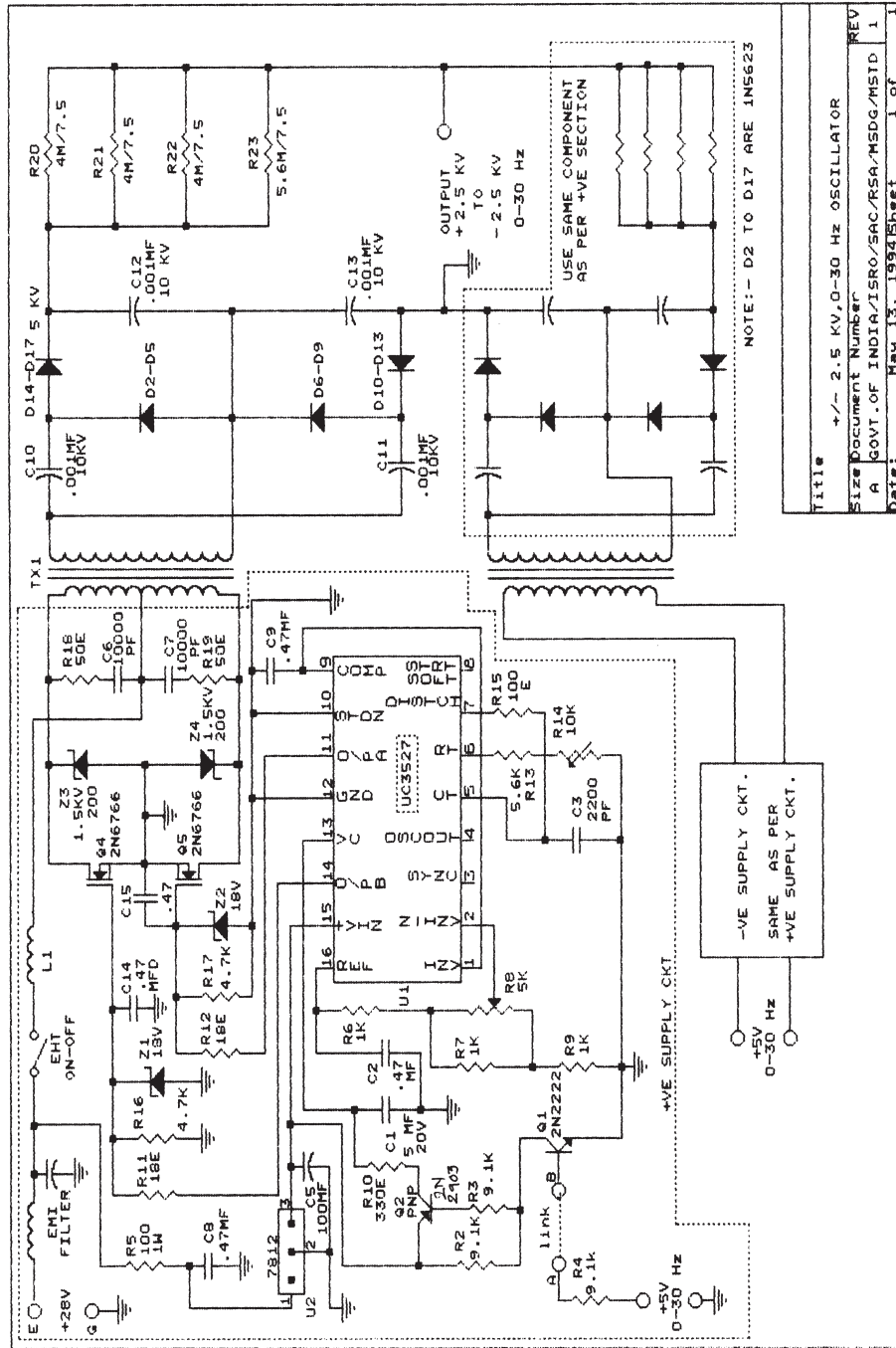


Figure A.1: KD*P switchable power supply

Appendix B

VMG-Data Acquisition Software

```
/* PROGRAMME:VIDEO MAGNETO GRAPH ( VMG.C ) LAST REVISION ON 02.02.1997
   WRITTEN AND REVISED BY SHIBU K. MATHEW */
/* THIS PROGRAM USES A SINGLE FRAME BUFFER.  THE ALTERNATE IMAGES ARE
   ADDED AND SUBTRACTED  TO THE PREVIOUS FRAME BUFFER CONTENT.
   NORMALISATION OF THE IMAGE IS DONE OFFLINE */

#include "/h0/ivlib3i/include/sys150.h"
typedef  short pixel;
extern pixel *mem_wptr();
#define NROWS 512
#define NCOLS 512

void time();
main()

{
register pixel *p;
int *q;
int i,j,k,l,err1;
```

```
int spin0,spin1;
int nframes,scale,ncycles,tcycles,a,b,sleep;
int fnstat;
int nf,nbits,dx,dy,ave,sum,c,d;
int zdiff,zsum;
pixel zratio;
int zval;
int nval;
int minzdiff,maxzdiff,dz,dzmin,dzmax,min,max;
int pulsewidth,cou;
int g,iv,ih,it;
WORD *fb1con,*fb2con;
int *sigeven;
char d1[100],dat[50];
int ti,da,tic,z,tc,halp,o,w;
short day;
FILE *f1,*f2,*f3,*f4,*f9;
char time1[100],time2[100],f5[100],f6[100],s1[50],hti[100],wti[100],an1,*s2,*s3;

sigeven=(int*)malloc(512*512*sizeof(int));

printf("\n\n");
printf("MEMORY LOCATION POINTER Q: %x\n",sigeven);

if(sigeven==NULL)
{
printf("Memory allocation failed, exiting..\n");
d1[0]=0;
```

```
memcpy(0x02800000L,d1,1);
exit(1);
}

q=sigeven;

for(i=0;i<NROWS;i++)
{
for(j=0;j<NCOLS;j++)
{
*q++=0;
}
}

printf("loading configuration file ....,");
if(load_cfg("/h0/ivlib3i/lib/150.cfg")!= NO_ERROR)
{
printf("Error in cofiguration file, exiting....\n");
d1[0]=0;
memcpy(0x02800000L,d1,1);
exit(1);
}

fb1con=(WORD*)0xc01332;
printf("loaded\n");

g=7;

printf("\n");
```



```
memcpy(0x02800000L,d1,1);
/* tsleep(58*g); */

initsys();

for(w=1;w<=tc;w++)
{
printf("cycle no      :%d\n",w);
for(z=1;z<=tcycles;z++)
{
q=sigeven;

for(i=0;i<NROWS;i++)
{
for(j=0;j<NCOLS;j++)
{
*q++=0;
}
}

printf("vmg cycle :%d\n",z);
printf("initializing.....");
select_fb(0);
fb_init();
fb_clf(FRAMEA,0);
fb_clf(FRAMEB,0);
fb_access(NONE,SCAN,SCAN);
fb_setsmask(FRAMEA,0x0000);
fb_setaq(OFF,OFF);
```

```
spin0=sys_spin(ALU,select_alu(-1));
fb_setxyspin(spin0,0);
fb_aq(CONTINUOUS);
printf("adi,fb");

select_alu(0);
alu_init();
fb_setxyspin(24,0);
alu_initregs();
alu_reset();
alu_setk(0,0,0,0);
alu_selwxyz(CONSTANT,VDI,VDAH,VDAL);
select_path(ALOW);
printf(",alu\n");

adi_camera(0);

time();
d1[0]=8;
memcpy(0x02800000L,d1,1);

adi_fbssel(0);

for(i=0;i<nframes;i++)
{

adi_waitvb();
alu_setop(SIGNED,A_PLUS_B,1);
```

```
    d1[0]=9;
    memcpy(0x02800000L,d1,1);
    adi_waitvb();
*fb1con=(WORD)(*fb1con|0x4);
adi_waitvb();
adi_waitvb();
*fb1con=(WORD)(*fb1con & 0xffffb);
d1[0]=8;
memcpy(0x02800000L,d1,1);

adi_waitvb();
alu_setop(SIGNED,B_MINUS_A,1);
d1[0]=10;
memcpy(0x02800000L,d1,1);
adi_waitvb();
*fb1con=(WORD)(*fb1con|0x4);
adi_waitvb();
adi_waitvb();
*fb1con=(WORD)(*fb1con & 0xffffb);
d1[0]=8;
memcpy(0x02800000L,d1,1);

}
select_fb(0);
p=(pixel*)mem_wptr(FB,0);
q=sigeven;
fb_access(FRAMEA,SCAN,NOSCAN);
fb_mmode(MEM);
```

```
adi_waitvb();
adi_waitvb();

min=7000000.0;
max=-7000000.0;

for(i=0;i<NROWS;i++)
{
for(j=0;j<NCOLS;j++)
{
zsum=*p;
*q++=zsum;
p++;
}
}

select_fb(0);
p=(pixel*)mem_wptr(FB,0);
q=sigeven;
fb_access(FRAMEA,SCAN,NOSCAN);
fb_mmode(MEM);
adi_waitvb();
adi_waitvb();

for(i=0;i<NROWS;i++)
{
for(j=0;j<NCOLS;j++)
```

```
{
zval= *q ;
if (zval < min ) min=zval;
if (zval > max ) max=zval;
*q++=zval;
}
}

select_fb(0);
p=(pixel*)mem_wptr(FB,0);
q=sigeven;
fb_access(FRAMEA,SCAN,NOSCAN);
fb_mmode(MEM);
adi_waitvb();
adi_waitvb();
select_path(ALOW);
printf("scaling the image to 0 - 255 levels.....\n");

for(i=0;i<NROWS;i++)
{
for(j=0;j<NCOLS;j++)
{
nval>(*q - min)*254.0/(max -min);
*p++=nval;
*q++=0;
}
}
*s3=max;
```

```
*s2=min;
adi_waitvb();
adi_waitvb();
select_fb(0);
fb_aq(STOP);

fb_mmode(IO);
fb_aq(OFF,ON);
f3=fopen("tem","r");
fscanf(f3,"%s",time1);
f4=fopen("tem1","r");
fscanf(f4,"%s",s1);
fclose(f3);
fclose(f4);
text(ALOW,0,150,10,HORIZONTAL,1,255,s1);
text(ALOW,0,225,10,HORIZONTAL,1,255,*s3);
text(ALOW,0,250,10,HORIZONTAL,1,255,*s2);
text(ALOW,0,10,10,HORIZONTAL,1,255,"USO VMG");
text(ALOW,0,75,10,HORIZONTAL,1,255,dat);
printf("transferring the image to hard disk..... \n\n");
im_write(ALOW,EIGHT_BIT,0,0,512,512,time1,"");
if(iv>0 && z<tcycles) tsleep(58*iv);
}
    if( an1 == 'y' || an1 == 'Y')
    {
time();
select_path(B1);
fb_clf(B1,0);
```

```
snap(B1);
f9=fopen("tem3","r");
fscanf(f9,"%s",wti);
fclose(f9);
text(B1,0,10,10,HORIZONTAL,1,255,"USO WHITE LIGHT");
text(B1,0,150,10,HORIZONTAL,1,255,wti);
im_write(B1,EIGHT_BIT,0,0,512,512,wti,"");
    }

if(halp>0)
{
d1[0]=12;
memcpy(0x02800000L,d1,1);
tsleep(58*g);

for(o=1;o<=halp;o++)
{
printf("halpha no  :%d\n",o);
time();
select_path(B1);
fb_clf(B1,0);
snap(B1);
f9=fopen("tem2","r");
fscanf(f9,"%s",hti);
fclose(f9);
text(B1,0,10,10,HORIZONTAL,1,255,"USO HALPHA");
text(B1,0,100,10,HORIZONTAL,1,255,hti);
im_write(B1,EIGHT_BIT,0,0,512,512,hti,"");
```

```
if(ih>0 && o<halp) tsleep(58*ih);
else
{
d1[0]=8;
memcpy(0x02800000L,d1,1);
tsleep(58*g);
}
}
printf("\n\n");
}

if(it>0 && w<tc) tsleep(58*it);
}
system("del tem*");
d1[0]=0;
memcpy(0x02800000L,d1,1);
}

void time()
{
int ti,da,tic,hms,hr,mn,sec,re;
short day;
FILE *fi1,*fi2,*fi3,*fi4;
fi1=fopen("tem","w");
fi2=fopen("tem1","w");
fi3=fopen("tem2","w");
fi4=fopen("tem3","w");
_sysdate(1,&ti,&da,&day,&tic);
```

```
hms=ti-19800;
hr=hms/3600;
re=hms-hr*3600;
mn=re/60;
re=re-mn*60;
sec=re;
fprintf(fi2,"%02d:%02d:%02dUT\n",hr,mn,sec);
fprintf(fi1,"V%02d%02d%02d\n",hr,mn,sec);
fprintf(fi3,"H%02d%02d%02d\n",hr,mn,sec);
fprintf(fi4,"W%02d%02d%02d\n",hr,mn,sec);
fclose(fi1);
fclose(fi2);
    fclose(fi3);
fclose(fi4);
return;
}
```

Bibliography

- [1] Ai G., and Hu Y., 1986, Publ. Beijing Astron. Obs. **8**, 27
- [2] Ai G., Zhang H., Li W., and Chen J., 1991, Chinese Sci. Bull. **36**, 1275
- [3] Alfvén H., and Carlqvist P., 1967, Solar Phys. **1**, 220
- [4] Ambastha A., and Bhatnagar A., 1988, J. Astrophys. Astr. **9**, 137
- [5] Ambastha A., Hagyard M. J., and West E. A., 1993, Solar Phys. **148**, 277
- [6] Babcock H. W., 1953. ApJ. **118**, 387
- [7] Bhatnagar A., 1986, *Solar Terrestrial Physics, Indo-US 1984 Workshop*, Kundu M. R., Biswas B., Reddy B. M., and Ramadurai S. (eds), National Physical Laboratory, New Delhi
- [8] Brian J., Goldstein H., and Schindler K., 1978, Solar Phys. **57**, 81
- [9] Bruzek A., 1967, Solar Phys. **2**, 451
- [10] Bumba A., 1958, Izv. Krymsk. Astrofiz. Obs. **19**, 105
- [11] Canfield R. C., 1986, *The Lower Atmosphere of Solar Flares*, Neidig D. F.(ed), National Solar Observatory, Sunspot
- [12] Cauzzi G., Smaldone L. A., Balasubramaniam K. S., and Keil S. L., 1993, Solar Phys. **146**, 207
- [13] Debi Prasad C., Ambastha A., and Ai G., 1998, Solar Phys. **179**, 133

- [14] Dunn R. B., and Zirker J. B., 1973, *Solar Phys.* **33**, 281
- [15] Fontenla J. M., Ambastha A., Kalman B., and Csepura Gy., 1995, *ApJ.* **440**, 894
- [16] Foukal P., 1971, *Solar Phys.* **19**, 59
- [17] Gaizauskas V., 1989, *Solar Phys.* **121**, 135
- [18] Goldberg L., 1953, University of Chicago press
- [19] Gold T., and Hoyle F., 1960, *MNRAS* **120**, 89
- [20] Gopasyuk S. I., Ogir M. B., Severny A. B., and Shaposhnikova E. F., 1962, *Izv. Krymsk. Astrofiz. Obs* **29**, 15
- [21] Hagyard M. J., Gaizauskas V., Chapman G. A., et al., 1986, *Energetic Phenomena on the Sun*, Kundu M., Woodgate B. (eds), NASA Conf. Publ. **2439**, 16
- [22] Hagyard M. J., 1988, *Solar Phys.* **115**, 107
- [23] Hagyard M. J., Cumings N. P., West E. A., and Smith J. E., 1982, *Solar Phys.* **80**, 33
- [24] Hagyard M. J., Smith J. B., Teuber D., and West E. A., 1984, *Solar Phys.* **91**, 115
- [25] Hale G. E., 1908, *ApJ.* **28**, 100
- [26] Hale G. E., et al., 1919, *ApJ.* **49**, 153
- [27] Harvey J. W., 1966, *HAO Astro-GeoPhysical Memorandum* 173
- [28] Heyvaerts J., Priest E. R., and Rust D. M., 1977, *ApJ.* **216**, 123
- [29] Hiei E., 1987, *Solar Phys.* **113**, 353
- [30] Howard R., and Babcock H. W., 1960, *ApJ.* **132**, 218
- [31] Jefferies J. J., and Mickey D. L., 1991, *ApJ.* **327**, 694

- [32] Jones H. P., Duvall T. L., Harvey J. W., Mahaffey C. T., Schwitters J. D., and Simmons J. E., 1992, *Solar Phys.* **139**, 211
- [33] Kiepenheuer K. O., 1953, *The Sun*, Kuiper (ed), University of Chicago press, Chicago
- [34] Kurokawa H., 1986, *The Lower Atmosphere of Solar Flares*, Neidig D., (ed), NSO/SMM flare symposium, 51
- [35] Kurokawa H., 1987, *Solar Phys.* **113**, 259
- [36] Kurokawa H., 1988, *Space Sci. Rev.* **51**, 49
- [37] Leighton R. B., 1959, *ApJ.* **130**, 366
- [38] Livi S. H. B., Martin S. F., and Wang J., 1989, *Solar Phys.* **121**, 197
- [39] Livingston W. *et al.*, 1971, *Pub. Roy. Obs. Edinburgh*, **8**, 52
- [40] Low B. C., 1977, *ApJ.* **212**, 234
- [41] Low B. C., 1982, *Rev. Geophys. Space Phys.* **20**, 145
- [42] Liggett M., and Zirin H., 1985, *Solar Phys.* **97**, 51
- [43] Lust R., and Schluter A., 1954, *Z. Astrophys.* **34**, 263
- [44] Martin S. F., Bentley R. D., Schadee A., Antalova A., Kucera A., Dezsó L., Gesztelyi L., Harvey K. L., Jones H., Livi S. H. B., and Wang J., 1984, *Adv. Space Res.* **4**, 61
- [45] Martin S. F., Livi S. H. B., Wang J., and Shi Z., 1985, *Measurement of Vector Magnetic Fields*, NASA Conf. Publ. **2734**, 403, Marshall Space Flight (MSFC), NASA, Alabama
- [46] Martres M. J., Michard R., and Soru-Iscovisci I., 1966, *Ann. Astrophys.* **25**, 4
- [47] Martres M. J., Michard R., and Soru-Iscovisci I., 1968, *Structure and Development of Solar Active Regions*, Kiepenheuer K. O., (ed), *IAU Symp.* **35**, 318

- [48] Martres M. J., and Soru-Escout, 1977, Solar Phys. **53**, 225
- [49] Mayfield E. B., and Lawrence K. J., 1985, Solar Phys. **96**, 293
- [50] Mehlretter J. P., 1974, Solar Phys. **38**, 43
- [51] Mickey D. L., 1985, Solar Phys. **97**, 223
- [52] Moore R. L., and LaBonte B. J., 1980, *Solar and Interplanetary Dynamics*, Dryer M., Tandberg H. E. (eds), IAU symposium **91**, 207
- [53] Neidig D. F., 1979, Solar Phys. **61**, 121
- [54] Parker E. N., 1955, ApJ. **122**, 293
- [55] Patty S. R., and Hagyard M. J., 1986, Solar Phys. **103**, 111
- [56] Philips K. J. H., 1995, *Guide to the Sun*, Cambridge University Press, Newyork
- [57] Prata S. W., 1972, Solar Physics. **25**, 136
- [58] Priest E. R., 1981, *Solar Flare Magnetohydrodynamics*, Gordon and Breach Science Publishers
- [59] Priest E. R., and Heyvaerts J., 1974, Solar Phys. **36**, 433
- [60] Ribes E., 1969, ApJ. **2**, 316
- [61] Rust D. M., 1972, Solar Phys. **25**, 141
- [62] Rust D. M., 1973, AFCRL Environm. Res. Rep., No.440
- [63] Rust D. M., 1974, *Flare Related Magnetic Field Dynamics*, HAO conference, Colardo, 243
- [64] Rust D. M., 1985, Aust. J. Phys., **38**, 781
- [65] Rust D. M., and Bridges C. A., 1975, Solar Phys. **43**, 129

- [66] Rust D. M., Appourchaus T., and Harris T. J., 1988, *The SAMEX Vector Magnetograph*, NASA Technical memorandum 4048
- [67] Sakurai T., 1976, *Solar Phys.* **47**, 261
- [68] Sakurai T., 1989, *Space Sci. Rev.* **51**,11
- [69] Sakurai T., Ichimoto K., Nishino Y., et al., 1992, *Publ. Astron. Soc. Japan*, **47**, 81
- [70] Scherrer P. H., Bogart R. S., Bush R. I., et al., 1995, *Solar Phys.* **162**, 129
- [71] Schmidt H. U., 1964, *NASA Solar Flare Symposium*, NASA, SP-50, 107
- [72] Schmieder B., Hagyard M. J., Ai G., Zhang H., Kalman B., Gyori L., Rompolt B., Demoulin P., and Machado M. E., 1994, *Solar Phys.* **150**, 199
- [73] Severny A. B., 1958, *Izv. Krymsk. Astrofiz. Obs.* **20**, 22
- [74] Severny A. B., 1960, *Izv. Krymsk. Astrofiz. Obs.* **22**, 12
- [75] Severny A. B., 1969, *Solar Flares and Space Research*, de Jager C., and Svestka Z., (eds), North Holland Publ. Co., Amsterdam, 38
- [76] Sivaraman K. R., Rausaria R. R., and Aleem S. M., 1992, *Solar Phys.* **138**, 353
- [77] Smithson R. C., 1973, *Solar Phys.* **29**, 365
- [78] Solanki S. K., 1993, *Space Sci. Rev.* **63**, 1
- [79] Stenflo J. O., 1989, *A&A Rev.* **1**, 3
- [80] Stenflo J. O., 1994, *Solar Magnetic Fields, Polarization Diagnostics*, Kluwer Academic Publishers, Dordrecht
- [81] Stix M., 1991, *The Sun*, Springer-Verlag, Berlin
- [82] Sturrock P. A., 1972, *Solar Phys.* **23**, 438

- [83] Svestka Z., 1975, *Solar Flares*, D. Reidel Publishing company
- [84] Tanaka K., 1975, BBSO reprint No. **0152**
- [85] Tanaka K., 1976, *Solar Phys.* **47**, 247
- [86] Tanaka K., 1987, *Publ. Astron. Soc. Japan* **39**,1
- [87] Tanaka K., and Nakagawa Y., 1973, *Solar Phys.* **33**, 187
- [88] Tanaka K., Smith Z., and Dryer M., 1980, *Solar and Interplanetary Dynamics*, Dryer M., and Tandberg E. H. (eds), *IAU Symp.* **91**, 231
- [89] Tandberg E. H., and Emslie G. A., 1988, *The Physics of Solar Flares*, Cambridge University Press
- [90] Tang F., 1986, *Solar Phys.* **105**, 399
- [91] Teuber D., Tandberg H., and Hagyard M. J., 1977, *Solar Phys.* **53**, 97
- [92] Vaughan J. M., 1989, *The Fabry-Perot Interferometer*, Adam Hilger, Bristol&Philadelphia
- [93] Varsik R. C., 1995, *Solar Phys.* **161**, 207
- [94] Venkatakrishnan P., 1993, *Solar Phys.* **143**, 385
- [95] Vorpahl J., 1973, *Solar Phys.* **28**, 115
- [96] Waldmeier M., 1947, *Publ. Zurich Obs.* **9**, 1
- [97] Wang H., 1988, *Solar Phys.* **117**, 343
- [98] Wang J., and Shi Z., 1993, *Solar Phys.* **143**, 119
- [99] Wang H., Tang F., Zirin H., and Ai G., 1991, *ApJ.* **380**, 282
- [100] West E. A., 1989, *SPIE.*, **1166**, 434

- [101] Worden S. P., and Simon G. W., 1976, *Solar Phys.* **46**, 73
- [102] Yariv A., 1991, *Optical Electronics*, Saunders College Publishing, Philadelphia
- [103] Zeldovich, Ya. B., Ruzmaikin A. A., and Sokoloff D. D., 1983, *Magnetic Field in Astrophysics*, Gordon and Breach
- [104] Zirin H., 1971, *Solar Magnetic Field*, Howard R. (ed), IAU Symp. **43**, 237, France
- [105] Zirin H., 1974, *Vistas Astron.* **16**, 1
- [106] Zirin H., 1989, *Astrophysics of the Sun*, Cambridge Univ. Press, Cambridge
- [107] Zirin H., 1988, *The physics of Magnetic Flux Ropes*, AGU Chapman conference, Pasadena, California
- [108] Zirin H., 1995, *Solar Phys.* **159**, 203
- [109] Zirin H., and Lazareff, B., 1975, *Solar Phys.* **41**, 425
- [110] Zirin H., and Liggett M. A., 1987, *Solar Phys.* **113**, 267
- [111] Zirin H., and Tanaka K., 1973, *Solar Phys.* **32**, 173